Development of Microphysiological Models for the Assessment of Xenobiotic and Endobiotic Absorption and Disposition

Brian D. Chapron

A dissertation

submitted in partial fulfillment of the

requirements for the degree of

Doctor of Philosophy

University of Washington

2018

Committee

Kenneth E. Thummel, Chair

Edward J. Kelly

Catherine Yeung

Program Authorized to Offer Degree:

Pharmaceutics

University of Washington

Abstract

Development of Microphysiological Models for the Assessment of Xenobiotic and Endobiotic Absorption and Disposition

Brian D. Chapron

Chair of Supervisory Committee:

Kenneth E. Thummel

Department of Pharmaceutics

Animal models and *in vitro* systems have long been relied upon to provide insights into the toxicology, pharmacodynamics and pharmacokinetics of investigational drug candidates before they are administered to human subjects. In this respect, these systems serve as crucial gatekeepers, protecting human subjects from some harmful prospective investigational drugs and also steering pharmaceutical researchers away from expending valuable time and resources on unpromising drug candidates. Despite the remarkable accomplishments in reducing both the drug attrition rates in clinical studies, existing preclinical models are far from refined systems. The growing recognition of crucial interspecies differences has prompted greater interest in human-derived *in vitro* preclinical models. However, cellular and subcellular systems, when separated from the crucial architecture of their native functional units (e.g. villi, acini, and

nephrons), lose the capacity to execute physiological functions that are dependent on their *in vivo* microenvironment. To this end, we have pursued the development of *in vitro* microphysiological systems that are designed to better reflect the native environment of *in vivo* organ tissues. Herein are described specific efforts to develop microphysiological systems for the assessment of xenobiotic and endobiotic metabolism and disposition in the human small intestine and renal proximal tubule.

The renal proximal tubule microphysiological system displayed numerous hallmark structural features and recapitulated of a many important physiological functions of the renal proximal tubule *in vivo*. Once validated, the kidney proximal tubule microphysiological system was used to characterize the megalin-mediated pathway through which vitamin D metabolites access their major site of bioactivation in humans, the proximal tubule epithelium. These findings are of broad importance given that the bioactive metabolite of vitamin D is a potent hormone with a demonstrated capacity to regulate the expression of xenobiotic-metabolizing enzymes and transporters.

Table of Contents

List of Nonstandard Abbreviations

1´-OH MDZ: 1´-hydroxymidazolam

13-DMT: 13-O-desmethyltacrolimus

1α,25$(OH)_2D_3$: 1α,25-dihydroxyvitamin D_3

1α,24,25$(OH)_3D_3$: 1α,24,25-trihydroxyvitamin D_3

24,25$(OH)_2D_3$: 24,25-dihydroxyvitamin D_3

25OHD_3: 25-hydroxyvitamin D_3

2-NBDG: 2-deoxy-2-[7-nitro-2, 1, 3-benzoxadiazol-4-yl) amino]-D-glucose

5-aza-dC: 5-aza-2'-deoxycytidine

A488-DBP: Alexa Fluor 488-conjugated DBP

BCRP: breast cancer resistance protein

CKD: chronic kidney disease

CYP24A1: cytochrome P450 24A1

CYP27B1: cytochrome P450 27B1

CYP2R1: cytochrome P450 2R1

CYP3A4: cytochrome P450 3A4

d_4-MDZ: d_4-midazolam

d_4-1'-OH MDZ: d_4-1'-hydroxymidazolam

DAPI: 4',6-diamidino-2-phenylindole;

DBP: vitamin D binding protein

DDI: drug-drug interaction

DME: drug-metabolizing enzyme

DMEM: high glucose Dulbecco’s modified eagle medium with L-glutamine

DMEM/F12: 50:50 Dulbecco’s modified eagle medium with Ham’s F-12

DMSO: dimethyl sulfoxide

DPBS: Dulbecco's phosphate-buffered saline, with no calcium or magnesium

$DPBS^{++}$: Dulbecco's phosphate-buffered saline with calcium and magnesium

EC_{50}: concentration of inducer at which half-maximal effect occurs

E_{max}: predicted maximal inductive effect

FBS: fetal bovine serum

FGF-23: fibroblast growth factor-23

fSIEC: fetal human small intestinal epithelial cells

GAPDH: glyceraldehyde 3-phosphate dehydrogenase

GGT: γ-glutamyl transpeptidase

GLUT1: glucose transporter 1

GLUT2: glucose transporter 2

GSSG: glutathione disulfide

HBSS: Hanks balanced salt solution

HCV: hepatitis C virus

HLM: human liver microsomes

IC_{50}: concentration of inhibitor at 50% inhibition

ICC: immunocytochemistry

IDBPs: intracellular vitamin D binding proteins

IgG: immunoglobulin G

iPSCs: induced pluripotent stem cells

ISTD: internal standard

ITS-A: insulin-transferrin-selenium A solution

k_{inact}: maximum inactivation rate constant

LC–MS/MS: liquid chromatography coupled with tandem mass spectrometry

MBI: mechanism-based inhibition

MDR1: multidrug resistance protein 1

MDZ: midazolam

MEM: minimum essential medium

MeOH: methanol

MRM: multiple reaction monitoring

MRP2: multidrug resistance-associated protein 2

NADPH: nicotinamide adenine dinucleotide phosphate

NDA: new drug application

NEAA: MEM non-essential amino acids

OCT1: organic cation transporter 1

P_{app}: apparent permeability coefficient

PBPK: physiologically-based pharmacokinetic

PCR: polymerase chain reaction

PCT: proximal convoluted tubule

PST: proximal straight tubule

PTB: $DPBS^{++}$ containing 0.1% Triton X-100 and 5% bovine serum albumin

PTECs: proximal tubule epithelial cells

PTH: parathyroid hormone

PT-MPS: proximal tubule microphysiological system

PXR: pregnane X receptor

RXR: retinoid X receptor

qRT-PCR: quantitative real-time PCR

RAD: renal tubule assist device

RAP: receptor-associated protein

SGLT2: sodium-glucose co-transporter 2

SI-MPS: small intestinal microphysiological system

TDI: time-dependent inhibition

TEER: trans-epithelial electrical resistance

UGT1A1: UDP glucuronosyltransferase 1A1

VDR: vitamin D receptor

VDRE: vitamin D response element

ZO-1: Zonula occludens-1

List of Figures

List of Tables

Acknowledgements

Firstly, I would like to thank my advisor, Dr. Kenneth Thummel, for his unique insights, incredible patience and encouragement throughout this long journey. I cannot imagine a better environment for the training of independent researchers than the one he has cultivated in his laboratory. I would like to thank Dr. Edward Kelly and Dr. Catherine Yeung for their review of my thesis and Dr. Terrance Kavanagh for serving as my Graduate Student Representative. I would also like to thank the many other individuals who provided constructive advice during the course of my research, in particular Dr. Danny Shen and Dr. Jonathan Himmelfarb. I would like to thank Dr. Zhican Wang and Dr. Yoshiyuki Yamaura for taking the time to teach me many of the laboratory techniques employed in my research.

I would like to thank my mother for her unwavering enthusiasm and support in my pursuit of this degree. I would also like to thank my uncle, Dennis Chapron, for introducing me to the field of pharmacy and the pharmaceutical sciences. Without his example, I would very likely not have considered this field of study and would have missed out on the many enriching experiences it has afforded me. I would also like to thank my wife, Alenka Chapron. Her intellectual and technical assistance in the lab has vastly improved the quality and scope of the research I was able to conduct. Lastly, I would like to thank my daughter, Lana, for being a crucial motivator towards finishing this thesis.

Dedication

To Alenka, Lana and Mom

1 Introduction

1.1 Critical Organs of Absorption, Metabolism and Excretion of Orally Administered Drugs

The bulk of mathematical models developed to predict *in vivo* pharmacokinetics have described drug handling by three organs, in particular the small intestine, the liver, and the kidney.[1-3] This is because while nearly every organ has some capacity to metabolize and transport drugs, the small intestine, liver and kidney are the principal organs governing drug absorption, metabolism and excretion respectively.[3] A multitude of factors contribute to the nuances of drug handling in these organs. However, it is primarily a combination of three factors that underlie these organs unique roles in drug disposition: (1) anatomical position, (2) enzyme/transporter content, and (3) high degree of blood perfusion.[3, 4] Hence these three factors are the repeating motifs for the following subsections on the small intestine, liver and kidney proximal tubule.

1.1.1 Small Intestine

The small intestine is the major site for the absorption of orally administered drugs in humans.[3, 4] Anatomically, the organ can be divided into the three major segments: the duodenum, jejunum, and ileum. The duodenum represents the initial portion of the small intestine, approximately 25-38 cm in length.[4] It receives the contents from the stomach, bile from the liver and digestive enzyme-rich secretions from the pancreas.[4] The duodenum transitions into the jejunum at the ligament of Treitz.[4] At 250 cm in length, the jejunum represents a much longer segment of the small intestine.[4] However, the jejunum and duodenum are histologically indistinct; both are rich in tissue folds, villi, and a monolayer of columnar epithelial cells (enterocytes) that provide a selectively permeable barrier.[3, 4] The transition of

the jejunum into the final segment of the small intestine, the ileum, is defined by a reduction in luminal diameter, thinning of the intestinal walls, abundant lymphoid tissue and decreases in size and number of circular folds.[4] At the ileocecal valve, the ileum terminates and large intestine, relatively devoid of the hallmark circular folds and villi of the small intestine, begins.[4]

The primacy of small intestine in the absorption of orally administered drugs is largely due to the organ's approximately 200 m^2 of total surface area, which is achieved through numerous tissue folds (plicae circulares), villi and a brush border of microvilli on the apical membranes of the enterocytes lining the intestinal lumen.[3, 4] Drug absorption in the small intestine is further facilitated by a high degree of tissue vascularization, a host of apical and basolateral uptake transporters and a favorable pH for the absorption weak bases, which constitute the majority of marketed drugs.[3]

In addition to facilitating the absorption of nutrients and drugs, the small intestine also represents a barrier for many xenobiotics. The presence of tight junctions prevents the substantial paracellular absorption of drugs over 350 g/mol.[3] The transcellular passage of drugs into systemic circulation is also restricted by a number of active efflux transporters in the apical membrane of enterocytes (e.g. P-gp, BCRP, MRP2) and drug-metabolizing enzymes (DMEs).[5] Cytochrome P450 3A (CYP3A) is the most notable among these DMEs due to its high expression in the villous tips and broad substrate specificity for lipophilic drugs.[6-8] Other notable intestinal DMEs include uridine glucuronosyltransferses, sulfotransferases, N-acetyl transferases and esterases.[3]

Once drugs cross the intestinal epithelium and interstitium and into the microvascular space, the high rate of villous blood flow rapidly draws the solutes away from the intestine and into the portal vein.[1, 3, 4] This reduces partitioning of absorbed drug back into the enterocytes

and ensures the maintenance of a favorable concentration gradient for absorption, with concentrations in the lumen exceeding microvascular drug concentrations.[3]

1.1.2 Liver

The liver is crucial to a number of physiological processes including hormone production, synthesis of plasma proteins, metabolism of ingested xenobiotics, metabolism of nutrients, and the production and secretion of bile into the intestine via biliary ducts.[4] It is supplied by both arterial (hepatic artery) and venous (portal vein) blood, with the portal flow dominating under most conditions.[3, 4] Portal triads comprised of branches of the hepatic artery and portal vein cluster with bile ducts traversing the hepatic tissue, supplying resident cells with oxygen and arterial and intestinal derived solutes.[4, 9] Blood egresses from the liver via central veins, regularly spaced tributaries of the hepatic vein.[4] The repetitive orientation of central veins and portal triads results in patterns of zonal distribution of oxygenation throughout the liver, differentially effecting protein expression in these regions and establishing physiologically functional units called acini.[9, 10] An acinus is ellipsoid in shape, although it is sometimes depicted as diamond, with lengthwise boundaries of opposite hepatic central veins and widthwise boundaries of opposite portal triads.[4, 9] The major cell type comprising the liver acinus is the hepatocyte.[4] Hepatocytes are responsible for most of the organ's physiological functions, including drug metabolism.[4]

Drugs absorbed by the intestine make their way into the portal vein and then are distributed into the hepatic acini.[3, 4] The sequential delivery of outgoing venous blood from the intestine directly to liver, prior to returning to the systemic pool, is what enables the liver to participate in the first-pass elimination processes for orally administered drugs.[1, 3] In addition

to its role in first-pass elimination, the liver is the principal organ of metabolism for most drugs in systemic circulation.[3] The extraordinary ability of the liver to clear drugs from the blood is primarily because it is highly perfused with fenestrated acinar capillaries, allowing for rapid equilibration of drugs in the blood with the hepatic tissue that possesses high levels of numerous drug metabolizing enzymes.[3, 4]

There exists a great diversity of drug metabolizing enzymes in liver including: cytochrome P450s, uridine glucuronosyltransferases, sulfotransferases, esterases, dehydrogenases and flavin-containing monoxygenases.[3] Notably, members of the cytochrome P450 family mediate the elimination of approximately half of all drugs whose primary site of metabolism is the liver. Furthermore, over half of all drugs cleared primarily by P450-mediated drug metabolism are metabolized to a significant extent via CYP3A4.[3] This central role of CYP3A4 is somewhat disquieting, considering the relatively large degree of interindividual variability in hepatic CYP3A4 expression.[11] Unlike other cytochrome P450s, the large interindividual variability of CYP3A4 expression is not easily ascribed to genetic polymorphisms in either CYP3A4 itself or regulatory genes.[12, 13]

1.1.3 Kidney Proximal Tubule

The human kidneys are the principal organs for carrying out a multitude of important physiological functions including: clearance of nitrogenous wastes, synthesis of a number of hormones, regulation of blood osmolality, xenobiotic excretion, maintenance of acid base homeostasis, and the reabsorption of nutrients and vitamins.[4] The gross anatomy of the kidney can be divided into an outer layer, the cortex, and an inner portion called the medulla.[4] Winding through the cortex and medulla are millions of nephrons, the physiologically functional

units of the kidney.[4] The nephron can be divided into a number of functionally distinct segments: the renal corpuscle, the proximal tubule, the distal tubule and the collecting duct.[4]

In humans, the renal proximal tubule is roughly 14 mm in length with an outside diameter of 40 μm.[14] The proximal tubule can be divided into two segments, the proximal convoluted tubule (PCT) and the proximal straight tubule (PST) on the basis of anatomy and histology.[4, 14] The initial portion of the proximal tubule, the PCT, begins at the urinary pole of Bowman's capsule, winds through the renal cortex, and transitions into the PST.[14] The PST descends in a straight line from the renal cortex into the medulla.[14] The relatively uniform line where the PST transitions into the thin descending tubule forms the boundary between the inner and outer stripe of the medulla.[14]

The proximal tubule epithelial cells (PTECs) of the PCT and PST have a large number of overlapping physiological functions and thus share many general morphological features including microvilli, numerous mitochondria, basolateral interdigitations, tight junctions, and a substantial endocytotic apparatus.[14] However, these histological features vary in degree between the PCT and PST due to differences in the relative magnitude of functional contributions the two segments make to particular physiological functions.[4, 14] Of note, the PTECs of the PCT possess many more basolateral invaginations/interdigitations, have relatively longer and more densely packed microvilli, and have more basalolaterally localized and elongated mitochondria than the PST.[14]

The renal proximal tubule is important for a number of physiological functions. Over 65% of filtered sodium is reabsorbed in the proximal tubule.[14] The solvent drag generated by this extensive sodium reuptake also makes the proximal tubule the principle site for renal water reabsorption.[4] Similar percentages of reabsorption also occur for phosphate (~80%), potassium

(~65%) and urea (~50%).[4, 14] Many filtered organic solutes are almost completely reabsorbed via active and facilitative transporters.[4, 14] A notable example is glucose, which is reabsorbed in the proximal tubule mostly by sodium-dependent glucose co-transporter 2 (SGLT2).[15] Interestingly, inhibitors of SGLT2 are clinically used to reduce renal glucose reuptake for the treatment of diabetes.[16]

Proteins represent another important constituent of the glomerular ultrafiltrate that undergoes active tubular reabsorption. With exception in certain disease states, the glomerular filtration of circulating proteins is limited by the size, structural conformation and electrical charge of a given protein.[17] While there is considerable debate as to the extent of renal filtration for many specific proteins, renal reabsorption of proteins that are filtered is a highly efficient process, as evidenced by the relative lack of intact proteins in the urine of healthy individuals.[14] The process by which filtered proteins are reabsorbed from the glomerular ultrafiltrate is receptor-mediated endocytosis, occurring principally in the proximal tubule.[18] Localized at the base of the apical brush border in PTECs, a multiligand endocytotic receptor, megalin, and its co-receptor, cubilin, have been identified as the major mediators of proximal tubular protein reabsorption.[18]

Megalin is a member of the lipoprotein receptor family and has a wide array of ligands including many that are not proteins.[19] The intracellular fate of proteins bound to megalin is a complicated process. The clathrin-coated vesicles that result from ligand-induced receptor internalization enter the cytosol and merge with early endosomes.[20] Early endosomes have a mildly acidic pH (~6.5) that facilitates the dissociation of many ligands from megalin and other endocytotic receptors.[21] Following ligand release, megalin can then be recycled back to the apical brush border to continue participating in endocytotic events.[19, 20] Early endosomes are

complex transient subcellular compartments and represent a crossroads for receptors/ligands retrieved from the apical and basolateral membranes in polarized epithelial cells.[21] This property of early endosomes underlies their ability to participate in transcytosis, where receptors and ligands that are not released within the early endosome can move on to the membrane opposite from which they originated.[21] Even ligands (e.g. albumin) that are liberated from their internalizing receptor (e.g. megalin) by the mildly acidic pH of the early endosome can bind to alternate receptors (e.g. neonatal Fc receptor) in the endosomal membrane and result in transcytosis when these receptors are recycled to the opposing membrane from which the ligand was internalized.[22] Endocytosed protein ligands and receptors that remain within the early endosome are exposed to decreasing pH and are eventually degraded as the endosome fuse with highly acidic lysosomes, replete with proteolytic enzymes.[21]

A number of small molecules and protein therapeutics are targets for megalin-mediated endocytosis in the renal proximal tubule.[19] For some of these drugs, the principal site of pharmacologic action or toxicity is within the kidney; notable examples are exogenously administered parathyroid hormone, interferon alpha and aminoglycosides.[19] Consideration of the role of megalin-mediated endocytosis in the intracellular disposition of these drugs may be important when modeling their pharmacokinetics and toxicity.

1.2 *In Vitro* Models for Drug Disposition

The development of physiologically accurate *in vitro* models for the liver, intestine and kidney, the major organs governing *in vivo* drug disposition, would represent a monumental shift in the way in which pharmacokinetics research is conducted in the preclinical phase of drug development. Heretofore, the use of non-human animal models and incomplete cellular or

subcellular systems has provided useful information in regards to identifying metabolic/transport pathways and the propensity of a candidate compound to inhibit these pathways.[23, 24] Increasingly, researchers are acknowledging important differences, both known and unknown, in transporters and drug-metabolizing enzymes in humans versus other animals.[25] However, even data generated from long established human-derived systems (e.g. hepatocyte suspensions, human liver microsomes) must be viewed with the understanding that these are incomplete systems and the complexity of the structural units comprising a given organ can have a profound effect on organ function and xenobiotic handling.[26]

Subcellular fractions, combined with protein quantification in human tissues and statistical modeling approaches have become a mainstay in predicting disease-induced and drug-precipitated changes in drug disposition.[27] The makers of physiologically-based pharmacokinetic (PBPK) modeling software have touted these programs as a replacement to small clinical trials in specialized populations, where difficulty in recruitment or ethical considerations make a properly-powered experimental trial infeasible.[28, 29] To their credit, these PBPK models have strived to be holistic, using anatomy as a guide to delineate distinct model compartments with physiologically accurate volumes, incorporating measured organ-specific enzyme/transporter content and modeling the sequential intra- and inter-organ transit of drugs as it is thought to occur *in vivo*.[29] However, the drug-dependent parameters used to populate these models are often built upon data acquired from subcellular fractions such as microsomal incubations and membrane vesicles.[30, 31] Differences in protein interactions, localization, orientation and retention of activity can alter parameter estimates and propagate errors through an otherwise physiologically relevant model. Even when whole cell systems are used, the resultant parameter estimates may not always reflect *in vivo* realities. The biology of

established cancer cell lines may differ substantially from that of cells in a healthy organ that it is intended to model. A notable example is the frequent reliance on the Caco-2 colon carcinoma cell line to model passive permeability in the small intestine.[32, 33] Differences in tight junction integrity and drug-metabolizing enzyme expression between the small intestine and Caco-2 cells suggest the model may poorly capture paracellular routes of absorption or the proposed interplay between drug-metabolizing enzymes and transporters in the small intestine.[32-35]

The limitations of conventional 2-dimensional cultures of immortalized or transfected cells lines has been a major impetus for the development of microphysiological systems (MPS),[36] *in vitro* cell culture platforms incorporating one or more organ-specific cell types under conditions encountered in their native *in vivo* environment. While many of the initial MPS have relied on the same immortalized cell lines used in traditional cultures,[36, 37] MPS developers have increasingly made use of primary human adult/fetal cells with the hopes of more faithfully recapitulating human physiology.[38-40] Future advances in dedifferentiation and subsequent reprogramming of adult human somatic cells into induced pluripotent stem cells (iPSCs) could also position iPSCs as valuable cell source for MPS models.[41] A particularly exciting prospect would be to culture patient-derived iPSCs in "personalized" MPS units that would be capable of providing timely information on organ function, guiding drug- and dose-selection by intrinsically accounting for many of the patient-specific factors that contribute to inter-individual variability.

For the MPS-based experiments described in this dissertation, I relied upon primary adult human PTECs with the notable exception of a few preliminary characterizations of MPS-cultured fetal human SIECs. PTECs cultured in the MPS were isolated from healthy renal cortical tissue obtained through research protocols at the University of Washington and used by

others and myself to constitute a kidney proximal tubule MPS (PT-MPS). The microfluidic platform used in the MPS was designed and fabricated by Nortis Inc. The Nortis platform was designed with broad applicability in mind and our group has used the product, with slight modifications, to recapitulate both the kidney proximal tubule epithelium and the liver. Additional details about the composition, structure and performance of the PT-MPS can be found in Chapter 4. In Chapters 4 and 5, I also detail efforts made to evaluate xenobiotic and endobiotic handling using this novel cell culture system.

1.3 Vitamin D Metabolism and Disposition

Vitamin D is a hormone that is well known for its critical role in regulating systemic mineral homeostasis [42]. In recent years, vitamin D status has also been implicated in immunological modulation, psychological health and cardiovascular health outcomes [42-44]. The principal sources of vitamin D in humans are intestinal absorption from the diet and sunlight-mediated *de novo* biosynthesis in the skin. Intestinally absorbed vitamin D is incorporated into chylomicrons and shuttled via the lymphatic circulation to the liver, blood and adipose tissues [45]. In contrast, epidermally-synthesized vitamin D enters directly into the vascular circulation where it is bound to its carrier protein, vitamin D binding protein (DBP). The binding of vitamin D to DBP is believed to facilitate a slower mode of delivery of vitamin D to the liver than the chylomicron-incorporated dietary-derived vitamin D [42, 46]. In this way, DBP may play a role in restricting the hepatic clearance of vitamin D, thereby establishing a more stable circulating reservoir of vitamin D. Importantly, the primary metabolite of vitamin D produced in the liver, $25OHD_3$, is even more tightly bound to DBP [42]. As such, DBP provides another important function, the maintenance of a circulating reservoir of vitamin D. $25OHD_3$ is

cleared by multiple P450-depedendent oxidation reactions, some of which are catabolic (e.g., 24- and 4'-hydroxylation) and one that is anabolic (1'-hydroxylation).[42] An alternate route of clearance for $25OHD_3$ is Phase II conjugative metabolism. Both glucuronide and sulfate metabolites of $25OHD_3$ have been identified, with the $25OHD_3$-3-*O*-sulfate metabolite circulating at higher concentrations than even unconjugated $25OHD_3$ [47, 48]. It is worth noting here that the sulfonation of $25OHD_3$ may not be a step in a terminal clearance pathway but rather a form of metabolic sequestration. A number of mammalian sulfatases have been identified in the human kidney.[49, 50] These enzymes may be capable of de-conjugating $25OHD_3$-3-O-sulfate back into $25OHD_3$.

Circulating $25OHD_3$ is the precursor to $1\alpha,25(OH)_2D_3$, the most biologically active form of vitamin D [42]. Vitamin D metabolites, specifically $1\alpha,25(OH)_2D_3$, exert their effects on gene transcription primarily by binding to the vitamin D receptor (VDR). Ligand-bound VDR complexes with retinoid X receptor (RXR) before translocating to the cell nucleus, where it can bind to putative vitamin D response elements (VDRE) that have been identified in over 150 genes [51]. Conversion of $25OHD_3$ to the bioactive VDR-ligand, $1\alpha,25(OH)_2D_3$, is mediated by the mitochondrial cytochrome P450 27B1 (CYP27B1) and has been identified in a number of tissues. However, biosynthesis of systemically available concentrations of $1\alpha,25(OH)_2D_3$ is thought to occur almost entirely in the proximal tubule epithelial cells (PTECs) of the kidney [42]. Presumably, extra-renal production $1\alpha,25(OH)_2D_3$ is necessary for tighter regulation of local concentrations of the hormone at certain privileged sites such as the small intestine and fat.

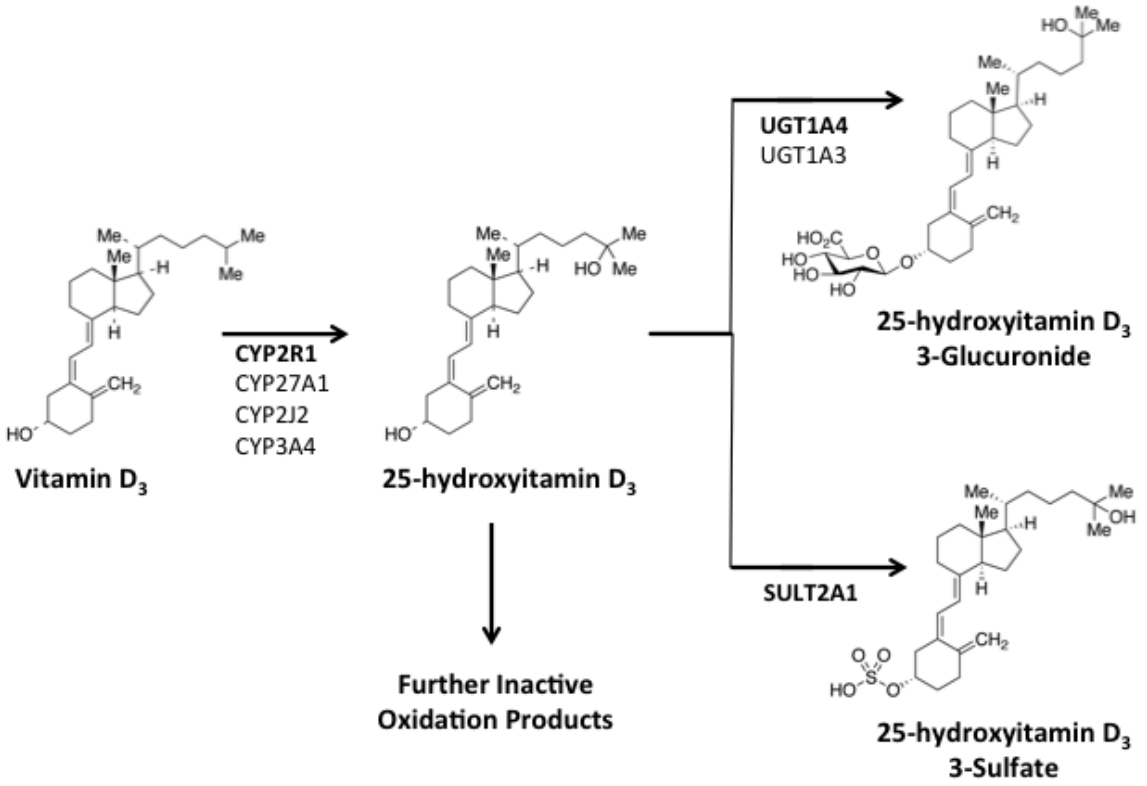

Figure 1.1. Hepatic Metabolism of Vitamin D_3. Vitamin D_3 enters into systemic circulation from either dietary sources or *de novo* synthesis in the skin upon exposure to UVB radiation.[42] Vitamin D_3 entering the liver is metabolized, primarily by CYP2R1, to 25-hydroxyvitamin D_3 which can, in turn be metabolized by the liver to further inactive oxidation products or conjugation products such as 25-hydroxyvitamin D_3-3-*O*-Sulfate or as 25-hydroxyvitamin D_3-3-*O*-Glucuronide by SULT2A1 and UGT1A3 respectively.[42, 52]

Because $25OHD_3$ is extensively bound to DBP in the plasma, levels of freely diffusible vitamin D are reduced and passive cellular uptake of the free hormone is restricted. To provide access of $25OHD_3$ to the site of bioactivation, megalin-mediated tubular endocytosis facilitates entry of the DBP-bound $25OHD_3$ from the glomerular filtrate into the PTECs. The 58 kDa size of DBP permits it to pass freely through the glomerular sieve [53, 54]. Clearance of active $1\alpha,25(OH)_2D_3$ and its precursor $25OHD_3$ from the intracellular space proceeds via mitochondrial CYP24A1-mediated 24-hydroxylation to $1\alpha,24,25(OH)_3D_3$ and $24,25(OH)_2D_3$ respectively. Unlike $1\alpha,25(OH)_2D_3$, the affinity of these 24-hydroxylated vitamin D metabolites for VDR is

very weak and this clearance pathway is generally considered inactivating, resulting in the respective terminal oxidation products, calcitroic and calcioic acids [42, 55].

1.4 Homeostatic Regulation of Vitamin D Uptake and Metabolism

Maintenance of proper systemic concentrations of calcium and phosphate is critical to a number of physiological functions. As such, phosphate and calcium homeostasis is a tightly controlled process. The presence of Vitamin D Response Elements (VDRE) in the genes coding for calcium transporters/receptors and the gene coding for FGF-23, a factor important in regulating phosphate transporters, allows $1\alpha,25(OH)_2D_3$ to directly and indirectly regulate calcium and phosphate handling in the intestine and kidney [56]. The importance of $1\alpha,25(OH)_2D_3$-mediated regulation of calcium and phosphate necessitates the tight regulation of $1\alpha,25(OH)_2D_3$ itself. Specifically, renal metabolism of $25OHD_3$ to $1\alpha,25(OH)_2D_3$ is induced by the action of parathyroid hormone (PTH) released from the parathyroid gland in response to low calcium or high phosphate [42]. In the proximal tubule, PTH acts on parathyroid hormone 1 receptor to induce expression of the 1α-hydroxylase, CYP27B1 [57]. As a compensatory mechanism, the increases in calcium and FGF-23 resulting from the biological actions of $1\alpha,25(OH)_2D_3$ and PTH are capable of suppressing $1\alpha,25(OH)_2D_3$ synthesis [58]. The negative feedback actions of calcium and FGF-23 are mediated by the calcium sensing receptor and FGF-receptor respectively [56, 59]. FGF-23 must complex with a VDR-regulated co-factor, klotho, in order to effectively agonize the FGF-receptor [56].

Taken as a whole, the body of literature on the adaptive regulation of vitamin D metabolism has revealed a complicated puzzle of highly interconnected pieces. However, certain parts of the picture, specifically those involving the homeostatic regulation of the tubular

endocytosis of $25OHD_3$ remain conspicuously absent. While a number of investigations have been undertaken to describe the pathological changes in megalin expression accompanying renal toxicant exposure [60-62], studies of the normal healthy adaptive response of megalin expression to $1\alpha,25(OH)_2D_3$ exposure have been lacking. To date, only a single study could be found on the Pubmed database that specifically addresses the question of $1\alpha,25(OH)_2D_3$-mediated regulation of megalin in the proximal tubule [63]. In that experiment, the authors administered $1\alpha,25(OH)_2D_3$ to an established cell line derived from rat proximal tubular cells.[63] They reported an approximately 2-fold increase in protein and mRNA transcript accumulation for megalin.[63] If these findings indeed highlight a real *in vivo* phenomena whereby $1\alpha,25(OH)_2D_3$ induces the expression of megalin at the apical brush-border of PTECs, it would run at odds with prevailing theme of negative-feedback inhibition that is associated with the homeostatic regulation of CYP24A1 and CYP27B1. Our attempts to reproduce these findings in isolated human PTECs suggest an opposite, more intuitive process, whereby $1\alpha,25(OH)_2D_3$ suppresses megalin mRNA transcripts (see Chapter 5).

1.5 Research Directions

The research appearing in this text serves as both a demonstration of deficiencies in existing *in vitro* models for predicting *in vivo* drug disposition and an examination of potential solutions to this problem. Described herein are my efforts towards the development of alternative *in vitro* models to fill this critical need. In my first hypothesis, I provide a proof of concept for the insufficiency of conventional models, both *in vitro* and mathematical, to describe the mechanisms underpinning a drug-precipitated modulation of *in vivo* drug clearance. The second and third hypotheses guide my line of inquiry in the development of novel *in vitro* models for two of the major organs governing drug-disposition, the small intestine and kidneys. The fourth hypothesis is a validation of the kidney model by testing its ability to recapitulate and further describe the renal disposition of a drug with unusual pharmacokinetics/pharmacodynamics, 25-hydroxyvitamin D_3.

The extensively studied endogenous prohormone, 25-hydroxyvitamin D_3 (Reyaldee®) is also an FDA-approved prodrug with complex disposition pathways that challenge conventional *in vitro* models in a number of ways. (1) Formation of its active metabolite is mediated by renal mitochondrial, rather than hepatic microsomal, P450s. (2) The active metabolite induces both its own clearance and the clearance of the prodrug to inactive compounds. (3) Within the principal organ of drug bioactivation, access of the prodrug to the intracellular space, metabolizing enzymes, and pharmacologic receptor (VDR, primarily for the active metabolite) rely upon a chain of direct protein-protein interactions and does not adhere to the assumptions of the free-drug hypothesis. (4) In addition, some of the phase II metabolites of 25-hydroxyvitamin D_3 produced in the liver may be reversibly cleaved back into the unconjugated prodrug at the site of bioactivation.

1.5.1 First Hypothesis

Telaprevir is a reversible time-dependent inhibitor of CYP3A.

Specific Aim 1a: Using traditional static modeling approaches, determine whether competitive inhibition by telaprevir and its major metabolite can account for the degree of CYP3A inhibition observed *in vivo*.

Specific Aim 1b: Assess time-dependence, NADPH-dependence and reversibility of telaprevir-mediated inhibition of CYP3A.

1.5.2 Second Hypothesis

A VDR-responsive intestinal cell source that expresses CYP3A and tight junctions can be identified for culture in a 3-dimensional SI-MPS.

Specific Aim 2a: Compare barrier integrity, CYP3A-mediated metabolism and VDR-mediated induction of mRNA transcripts coding for proteins related to intestinal drug disposition in LS180, T84, Caco-2 and human fSIECs.

Specific Aim 2b: Conduct a preliminary evaluation of cell survival and polarity of fSIECs cultured in the SI-MPS.

1.5.3 Third Hypothesis

A 3-dimensional PT-MPS can be established that will respond to VDR-dependent regulation of vitamin D_3 metabolism.

Specific Aim 3a: Determine the structural biology of PTECs and their capacity to retain fundamental kidney-specific physiological functions when cultured in the PT-MPS.

Specific Aim 3b: Validate experimental conditions under which the effects of $1\alpha,25(OH)_2D_3$ and $25OHD_3$ metabolism can be evaluated in the PT-MPS.

1.5.4 Fourth Hypothesis

Megalin modulates the cellular uptake of DBP-bound vitamin D metabolites, which in turn, exert feedback regulation of megalin gene expression.

Specific Aim 4a: Assess the effect of megalin inhibition on the cellular uptake of DBP and $25OHD_3$ into PTECs.

Specific Aim 4b: Assess the effect of megalin inhibition on VDR-dependent pharmacologic activity of $1\alpha,25(OH)_2D_3$.

Specific Aim 4c: Characterize the effects of $1\alpha,25(OH)_2D_3$ on megalin gene expression.

2 Reversible, Time-Dependent Inhibition of CYP3A-Mediated Metabolism of Midazolam and Tacrolimus by Telaprevir in Human Liver Microsomes

Portions of this chapter were published in J Pharm Pharm Sci. 2015;18(1):101-11

2.1 Abstract

Telaprevir inhibits CYP3A resulting in drug-drug interactions (DDI) of unprecedented magnitude. We investigated the mechanisms by which telaprevir inhibits the oxidation of midazolam and tacrolimus in human liver microsomes (HLM). We performed a static mechanistic DDI prediction to evaluate whether previously reported competitive inhibition of CYP3A by telaprevir and its diastereomeric metabolite, VRT-127394, is sufficient to explain the remarkable reduction in apparent oral clearance observed with oral midazolam and tacrolimus. To further explore the inhibitory mechanisms of telaprevir, we assessed whether telaprevir-mediated inhibition of the oxidation of midazolam and tacrolimus is time-dependent in human liver microsomes, and if present, as to its reversibility. The competitive inhibition model failed to account for the magnitude of telaprevir interactions in human subjects. In comparing HLM incubations with and without a prior 30-min exposure to telaprevir, a respective 4- and 6-fold reduction in IC_{50} was observed with midazolam and tacrolimus as substrates. The time-dependent inhibition was further shown to be nicotinamide adenine dinucleotide phosphate (NADPH)-dependent, and either completely (midazolam) or partially (tacrolimus) reversible upon dilution of the microsomes. The interaction between telaprevir and midazolam or tacrolimus involves both competitive and time-dependent inhibition mechanisms. Such time-dependent inhibition is not explained by irreversible mechanism-based inactivation of CYP3A. Formation of potent inhibitory metabolites may contribute to the remarkable *in vivo* inhibitory potency of telaprevir.

2.2 Introduction to Chapter 2

Introduction of the first hepatitis C virus (HCV) protease inhibitors, telaprevir and boceprevir, in 2011 marked a major milestone in hepatitis C drug development. HCV protease inhibitors, when used in combination with ribavirin and peginterferon alpha, were the first of a new generation of direct-acting drug treatments for combating HCV.[64, 65] However, during development, telaprevir was found to precipitate a number of drug-drug interactions (DDI).[66] In particular, attention was drawn to the profound interaction between telaprevir and the immunosuppressant, tacrolimus.(Coilly, 2014 #26) Although newer and more effective drugs have since replaced telaprevir in the treatment of hepatitis C, the unprecedented magnitude of this interaction, an approximately 67-fold reduction in tacrolimus oral clearance, raises interesting scientific questions with respect to the pharmacokinetic mechanism(s) of this interaction.[67]

In the "*Clinical Pharmacology & Biopharmaceutics Review*" section of the NDA for Incivek® (telaprevir),[68] Vertex Pharmaceuticals reported on *in vitro* studies demonstrating competitive inhibition of CYP3A4, as measured by midazolam 1'-hydroxylation, with a K_i of 1.43 μM. A major metabolite, VRT-127394, was also identified as a competitive inhibitor of CYP3A4 with a reported K_i of 0.94 μM. In the work described herein, we attempted a prediction of the joint effects of telaprevir and VRT-127395 based upon a mechanistic static DDI model that assumed reversible, competitive inhibition of CYP3A in the gut mucosa and the liver. The competitive inhibition DDI model was not able to adequately account for the approximately 14-fold reduction in midazolam oral clearance that was observed *in vivo*. Under-prediction of the interaction was even more pronounced in the case of tacrolimus. One possible explanation for this discrepancy between the predicted and observed interactions could be the presence of

additional mechanisms of CYP3A inhibition. An *in vitro* maximum inactivation rate constant (k_{inact}) of 0.065 min^{-1} using midazolam as the reporter substrate was quoted in the telaprevir NDA,[68] implying evidence of mechanism-based inhibition (MBI). More recently, *Oda and Yamano* reported observing MBI of tacrolimus oxidation by telaprevir in human liver microsomes (HLM).[69]

We set out to confirm and further characterize the putative MBI by telaprevir *in vitro*. We were able to demonstrate time-dependent inhibition of both midazolam and tacrolimus metabolism in HLMs. However, we observed reversibility in the time-dependent inhibition, pointing to mechanisms other than irreversible MBI.

2.3 Materials and Methods

2.3.1 Chemicals and Reagents

Telaprevir was obtained from Toronto Research Chemicals (Toronto, Canada). NADPH, tacrolimus and rapamycin were obtained from Sigma-Aldrich (Steinheim, Germany). 13-O-desmethyltacrolimus (13-DMT) was extracted and purified from incubates of HLMs with tacrolimus according to an established method.[70] Midazolam and 1'-hydroxymidazolam (1'-OH-MDZ) were obtained from Cerilliant (Round Rock, TX). Pooled HLMs were obtained from Xenotech (Lenexa, KS). Recombinant P450s were obtained from BD Biosciences (Woburn, MA). All other solvents and reagents were of analytical reagent grade.

2.3.2 Modeling of Competitive Inhibition Scenarios

We utilized a mechanistic static DDI modeling approach described in several previous publications.[1, 71, 72] The fold-change in apparent oral clearance (CL_{oral}) of either midazolam

or tacrolimus in the presence of telaprevir and VRT-127394 was the principal endpoint for our model prediction. Prediction of CL_{oral} entailed an assessment of the impact of CYP3A inhibition by telaprevir and VRT-127394 on the fraction absorbed (F_a), fraction escaping first-pass gut metabolism (F_g), fraction escaping first-pass hepatic metabolism (F_h), and systemic clearance (CL_{sys}) for midazolam and tacrolimus. Baseline values of F_a, F_g, F_h and CL_h (i.e., in the absence of inhibitors) were either taken directly or estimated based upon data from the literature.[73, 74] Linear pharmacokinetics were assumed for both object drugs. The following sections provide salient details on how the F_a, F_g, F_h and CL_h parameters during telaprevir co-administration were computed.

Systemic Clearance (CL_{sys}). Systemic elimination of both midazolam and tacrolimus was assumed to occur exclusively via hepatic metabolism; hence, CL_{sys} was set equal to hepatic clearance (CL_h). Baseline hepatic intrinsic clearance ($CL_{h,int}$) of midazolam or tacrolimus was estimated from their corresponding literature reported systemic clearance and hepatic blood-flow (Q_h) according to the well-stirred hepatic clearance model.

All clearance values were referenced to blood concentrations of the object drug. Specifically, plasma clearance values for midazolam were converted to blood clearance values using the equilibrium blood-to-plasma ratio of midazolam.[75] Q_h was assumed to be 90 L/h.[2]

$$CL_h = \frac{Q_h * CL_{h,int}}{Q_h + CL_{h,int}} \quad (1)$$

A term reflecting the fold-reduction in the intrinsic clearance parameter for the object drug due to additive competitive inhibition by telaprevir and VRT-127394 was defined as the inhibition ratio (*IR*).[1] Subscripts in the *IR* parameter denote the assumptions adopted regarding inhibitor concentrations at the clearance site; viz., systemic concentration driven inhibition

(IR_{sys}), maximum potential inhibition of first-pass elimination in the gut ($IR_{g,max}$), or hepatic portal vein ($IR_{hpv,max}$) when calculating the particular inhibition ratio. For example, IR_{sys} denotes the inhibition ratio for intrinsic clearance using unbound systemic concentrations of telaprevir ($I_{sys,telaprevir}$) and VRT-127394 ($I_{sys,VRT127394}$).

$$IR_{sys} = 1 + \frac{f_u * I_{sys,telaprevir}}{K_{i,telaprevir}} + \frac{f_u * I_{sys,VRT127394}}{K_{i,VRT127394}} \quad (2)$$

Only unbound telaprevir and VRT-127394 in plasma were assumed to access the intra-hepatocellular site and inhibit CYP3A.

Plasma concentrations of telaprevir and VRT-127394 during co-administration with each object drug were taken from their respective DDI studies in healthy volunteers.[67, 73] Telaprevir and VRT-127394 concentrations were evaluated as a range from the lower to upper bound of the reported 95% confidence interval of their average steady-state plasma concentrations during chronic dosing at 750 mg of telaprevir every 8 hours. The unbound inhibitor concentrations were estimated by multiplying the total concentrations by the fraction unbound (f_u) of 0.24 to 0.41, as reported in the telaprevir NDA.[68] Competitive inhibition constants of 1.43 and 0.94 μM were assigned for telaprevir ($K_{i,telaprevir}$) and VRT-127394 ($K_{i,VRT127394}$) respectively, as reported in the NDA.[68]

As indicated in the equation below IR_{sys} was only applied to CYP3A-mediated fraction of intrinsic clearance ($f_{m,CYP3A}$: 0.94 for midazolam and 1.0 for tacrolimus) thereby accounting for hepatic metabolism that is not inhibited by telaprevir (i.e. non-CYP3A mediated pathways).[76] The assumption of complete metabolism of tacrolimus by CYP3A (i.e., $f_{m,CYP3A}$ = 1) was substantiated by conducting substrate depletion experiments with recombinant CYP1A1,

CYP1A2, CYP2B6, CYP2C19, CYP2C8, CYP2C9, CYP2D6, CYP3A4 and CYP3A5. In this experiment, the only P450s that observably metabolized tacrolimus were CYP2D6, CYP3A4 and CYP3A5. The intrinsic clearance per pmol of CYP2D6 was approximately one-third that of CYP3A (data not shown), or 60-fold lower when scaled to their respective enzyme content in the liver.[8] Therefore, CYP2D6-mediated metabolism of tacrolimus was ignored in our modeling on the basis of its modest activity and the relatively low expression of CYP2D6 in both the gut and liver.[8] Furthermore, adopting an $f_{m,CYP3A} = 1$ afforded the simple competitive inhibition model the fullest potential in predicting the magnitude of the competitive inhibition.

$$CL_{h,int,inh} = \frac{CL_{h,int} * f_{m,CYP3A}}{IR_{sys}} + CL_{h,int} * (1 - f_{m,CYP3A}) \quad (3)$$

Hepatic Clearance (CL_h). Hepatic intrinsic clearance accounted for competitive inhibition ($CL_{h,int,inh}$) was applied to the well-stirred model to generate an estimate for the inhibited systemic hepatic clearance ($CL_{h,inh}$).[2]

Gut Absorption (F_a). Drug release from the dosage form and mucosal permeability were assumed not to be affected by telaprevir; i.e., F_a remains the same in the presence of the inhibitor. This assumption ignores the potential effect of intestinal P-glycoprotein on the intestinal absorption of tacrolimus. The values for F_a were calculated from the literature and were 0.90 and 0.96 for midazolam and tacrolimus respectively.[74, 77]

Gut First-Pass (F_g). The usual challenge in the static prediction of first-pass inhibition is what relevant inhibitor concentration ought to be used in the *IR* term. We chose to model both the "least" and "maximum" impact scenarios; the former represents the period after the intestinal absorption of telaprevir had been completed, whereas the latter considers the moment shortly

after inhibitor co-administration. The following equation based upon the Q_{gut} model was used to assess the "least" scenario; that is, the impact of average systemic inhibitor concentrations on the fraction of drug escaping first-pass intestinal extraction ($F_{g,inh}$).[1] Intestinal metabolism of midazolam or tacrolimus was assumed to be solely mediated by mucosal CYP3A.

$$F_{g,inh} = \frac{F_g}{F_g + (1 - F_g) * \left(\frac{1}{IR_{sys}}\right)} \quad (4)$$

We also estimated the fraction escaping intestinal extraction for the "maximum" inhibition scenario ($F'_{g,inh}$) ; in this case, the first-order absorption rate constant (k_a), telaprevir dose (D), and blood drainage from the intestinal villi (Q_{villi}) determine the local (mucosal) concentration of telaprevir ($I_{g,max}$) and inhibition ratio ($IR_{g,max}$).[78] Note that circulating concentration of VRT-127394 continues to apply in this scenario.

$$I_{g,max} = \frac{k_a * F_a * D}{Q_{villi}} \quad (5)$$

$$IR_{g,max} = 1 + \frac{I_{g,max} + (f_u * I_{sys,telaprevir})}{K_{i,telaprevir}} + \frac{f_u * I_{sys,VRT127394}}{K_{i,VRT127394}} \quad (6)$$

Hepatic First-Pass (F_h). The previously derived $CL_{h,inh}$ was used to predict the fraction escaping hepatic first-pass metabolism in a "least" inhibition scenario ($F_{h,inh}$), wherein the effective concentrations of the inhibitors equal their systemic concentrations during the post-absorptive phase of telaprevir pharmacokinetics.

$$F_{h,inh} = 1 - \left(\frac{CL_{h,inh}}{Q_h}\right) \quad (7)$$

The following equation represents the "maximum" inhibition scenario during first-pass following simultaneous telaprevir and object drug administration. This scenario assumes a transiently elevated inflow portal venous concentration that equals the sum of re-circulating and newly absorbed telaprevir from the gut lumen into the hepatoportal blood flow ($I_{hpv,max}$).[1]

$$I_{hpv,max} = \frac{k_a * F_a * F_g * D}{Q_h} \quad (8)$$

$$IR_{hpv,max} = 1 + \frac{f_u * (I_{hpv,max} + I_{sys,telaprevir})}{K_{i,telaprevir}} + \frac{f_u * I_{sys,VRT127394}}{K_{i,VRT127394}} \quad (9)$$

Again, hepatoportal concentrations of VRT-127394 were assumed to be equal to systemic concentrations (i.e., no sequential first pass). The above $IR_{hpv,max}$ expression applies if the entire telaprevir dose was absorbed instantly at the same time as the object drug. It allows us to determine the effect of these hepatoportal concentrations on the fraction of substrate escaping first-pass metabolism under "maximum" inhibition conditions ($F'_{h,inh}$).

Systemic bioavailability of each object drug was computed in the absence ($F_{total} = F_a \cdot F_g \cdot F_h$) and presence of co-administered inhibitor under either the "least" or "maximum" inhibition scenario ($F_{total,inh} = F_a \cdot F_{g,inh} \cdot F_{h,inh}$ or $F'_{total,inh} = F_a \cdot F'_{g,inh} \cdot F'_{h,inh}$). A third "extreme" scenario was considered that assumed complete absorption ($F_a = 1$) and total abolition of first-pass elimination processes ($F_{g,inh} \cdot F_{h,inh} = 1$). Essentially, this final scenario is one where systemic

availability ($F_{total,inh}$) is set to a fixed value of 1 and apparent oral clearance ($CL_{oral,inh}$) is effectively reduced to the inhibited systemic or hepatic clearance ($CL_{sys,inh}$ or $CL_{h,inh}$).

All three scenarios were evaluated in terms of the predicted fold-reduction in apparent oral clearance from telaprevir co-administration compared to the uninhibited state. Below are the final equations used to determine the fold-reduction from the baseline apparent oral clearance to that in the "least" ($CL_{oral,inh}$), "maximum" ($CL'_{oral,inh}$), and "extreme" scenarios respectively.

$$\frac{CL_{oral}}{CL_{oral,inh}} = \frac{CL_{oral}}{\left(\frac{CL_{sys,inh}}{Fa*F_{g,inh}*F_{h,inh}}\right)} \quad (10)$$

$$\frac{CL_{oral}}{CL_{oral,inh}} = \frac{CL_{oral}}{\left(\frac{CL_{sys,inh}}{Fa*F'_{g,inh}*F'_{h,inh}}\right)} \quad (11)$$

$$\frac{CL_{oral}}{CL_{oral,inh}} = \frac{CL_{oral}}{\left(\frac{CL_{sys,inh}}{1}\right)} \quad (12)$$

A glossary of all model parameters is provided below.

CL_h: hepatic clearance

$CL_{h,inh}$: inhibited hepatic clearance

$CL_{h,int}$: hepatic intrinsic clearance

$CL_{h,int,inh}$: inhibited apparent hepatic intrinsic clearance

CL_{oral}: oral clearance

$CL_{oral,inh}$: inhibited oral clearance assuming "least" gut and hepatoportal inhibitor concentrations during first-pass

$CL'_{oral,inh}$: inhibited oral clearance assuming "maximum" gut and hepatoportal inhibitor concentrations during first-pass

CL_{sys}: systemic clearance

$CL_{sys,inh}$: inhibited systemic clearance

D: dose

F_a: fraction absorbed

F_g: fraction escaping first-pass gut metabolism

$F_{g,inh}$: inhibited fraction escaping first-pass gut metabolism assuming "least" gut inhibitor concentrations during first-pass

$F'_{g,inh}$: inhibited fraction escaping gut metabolism assuming "maximum" gut inhibitor concentrations during first-pass

F_h: fraction escaping first-pass hepatic metabolism

$F_{h,inh}$: inhibited fraction escaping first-pass hepatic metabolism assuming "least" hepatoportal inhibitor concentrations during first-pass

$F'_{h,inh}$: inhibited fraction escaping hepatic metabolism assuming "maximum" hepatoportal inhibitor concentrations during first-pass

F_{total}: absolute oral bioavailability

$F_{total,inh}$: inhibited absolute oral bioavailability assuming "least" gut and hepatoportal inhibitor concentrations during firt-pass

$F'_{total,inh}$: inhibited absolute oral bioavailability assuming "maximum" gut and hepatoportal inhibitor concentrations during first-pass

$f_{m,CYP3A}$: fraction metabolized by CYP3A

f_u: fraction unbound

$I_{g,max}$: theoretical "maximum" inhibitor concentrations at the gut epithelium

$I_{hpv,max}$: theoretical "maximum" hepatoportal inhibitor concentrations

$I_{sys,telaprevir}$: systemic telaprevir concentrations

$I_{sys,VRT127394}$: systemic VRT-127394 concentrations

$IR_{g,max}$: inhibition ratio for first-pass gut metabolism assuming "maximum" gut inhibitor concentrations

$IR_{hpv,max}$: inhibition ratio for first-pass hepatic metabolism assuming "maximum" gut inhibitor concentrations

IR_{sys}: inhibition ratio for the CYP3A-mediated fraction of the intrinsic clearance

k_a: first-order absorption rate constant

$K_{i,telaprevir}$: competitive inhibition constant for telaprevir

$K_{i,VRT127394}$: competitive inhibition constant for VRT-127394

Q_h: hepatic blood flow

Q_{villi}: blood drainage from the intestinal villi

2.3.3 IC_{50} Shift Experiments

Incubation mixtures (200 µL volume), containing 0.05 mg/mL pooled HLM, fixed concentration of substrate (either 1 µM midazolam or 0.5 µM tacrolimus), and variable concentration of telaprevir or corresponding vehicle control in a phosphate buffer medium (100 mM KH_2PO_4, 1 mM ethylenediaminetetraacetic acid, pH = 7.4), were pre-warmed at 37°C in a shaker water bath for 5 min prior to initiation of reaction. To construct an IC_{50} curve, telaprevir concentration was varied from 0.05 µM to 10 µM. Due to non-specific binding of tacrolimus to the HLM and incubation vessel, the unbound concentration in the 0.5 µM tacrolimus incubations was effectively 0.1 µM in this particular experimental setup. Midazolam and telaprevir had no appreciable (< 20%) non-specific binding and thus their nominal concentrations were considered as the unbound concentrations.[79] The concentrations of midazolam or tacrolimus were chosen so as to achieve unbound concentrations below their respective K_m for CYP3A.[79, 80] The CYP-mediated reaction was initiated with 50 µl of 5 mM NADPH (final 1 mM concentration)

and quenched with either 250 µL of ice-cold acetonitrile (midazolam) or 2 mL methyl tert-butyl ether (tacrolimus) after incubating for 2 minutes. All incubations were conducted in quadruplicates.

For midazolam incubations, 20 µL of d4-1'-OH-MDZ (0.25 ng/µL) was added as internal standard to each of the quenched reaction mixtures, which were then centrifuged at 14,000 rpm for 10 min at 4°C. A portion of the supernatant was then transferred to 96-well plates for LC/MS-MS analysis. For tacrolimus incubations, 20 µL of rapamycin (1.1 ng/µL) was added as internal standard before addition of methyl tert-butyl ether. The aqueous phase was frozen by dry ice. The solvent phase was then decanted and evaporated under N_2 gas. The sample residues were reconstituted in 75 µL of methanol and transferred to glass inserts for LC/MS-MS analysis. Activity of CYP3A was measured by 1'-OH-MDZ formation for midazolam and 13-DMT formation for tacrolimus.

To assess time-dependent inhibition, IC_{50} experiments were performed after pre-incubating 0.05 mg/mL HLM with 1 mM NADPH and varying concentration of telaprevir (0.05 to 10 µM) for 30 minutes. Parallel pre-incubations with vehicle control (0.3% DMSO) were also performed to assess any non-telaprevir mediated decreases in CYP3A activity related to the 30-minute pre-incubation. Substrate reaction was then initiated by the addition of 1 µM midazolam or 0.5 µM tacrolimus to the reaction mixture. These reactions were quenched and processed for analysis as described above.

2.3.4 NADPH Dependence and Reversibility Experiments

Co-incubations of substrate (0.5 µM for tacrolimus or 1 µM for midazolam) and telaprevir (1 µM for tacrolimus or 0.5 µM for midazolam) in HLM were performed after varying

durations of pre-incubation with telaprevir (0, 15, or 30 minutes). Each of the three pre-incubation duration experiments was further designed to assess whether the IC_{50} shifts observed in earlier experiments were NADPH-dependent (i.e., CYP-dependent) and whether the time-dependent IC_{50} shift was related to CYP3A inactivation (i.e., irreversible or slowly reversible inhibition). For the NADPH-dependent experiment, the incubation protocol was essentially the same as that described for the IC_{50} shift experiment except that either NADPH or vehicle was added at the outset of pre-incubation; for the vehicle incubation, 1 mM NADPH was added along with the substrate to initiate the reporting reaction. For the reversibility experiment, pre-incubation was conducted with a 20-fold greater concentration of HLM (1 mg/mL) at a volume of 500 µL After the designated duration of pre-incubation with telaprevir (0, 15, or 30 min), the concentrated microsomal incubate was diluted 20-fold (i.e., to 0.05 mg/mL). Fifty µL of the diluted, pre-incubation mixture was transferred to a 200 µL reaction mixture containing substrate (final concentration 0.5 µM tacrolimus or 1 µM midazolam) and 1 mM of fresh NADPH, which was allowed to co-incubate for 2 minutes before quenching.

2.3.5 Metabolite Analysis

1'-OH MDZ and 13-DMT concentrations were quantified using an Agilent 1290 HPLC system (Agilent, Santa Clara, CA) connected to a triple quadrupole mass spectrometer (Agilent 6410 LC-MS/MS) operated in the positive ion mode. Chromatography for 1-OH-MDZ in the acetonitrile extract was achieved using a reverse-phase column (Zorbax SB C18, 2.1 mm x 150 mm x 5 µm; (Agilent, Santa Clara, CA) at 35°C. The aqueous (A) mobile phase consisted of 10 mM ammonium formate (pH = 4) and 100% acetonitrile was used for the organic (B) mobile phase. The gradient for the mobile phase was as follows: (1) mobile phase A was set to 55% from 0 to 5 min at a total flow of 0.25 mL/min, (2) a linear gradient from 5 min to 6 min

decreased phase A to 5% and increased flow to 0.3 mL/min, which were held until 8 min, (3) a linear gradient increased phase A back to 55% from 8 to 8.1 min and decreased total flow back to 0.25 mL/min, which were maintained for the remainder of the run. The total run time was 12 minutes per sample. 1'-OH-MDZ and d4-1-OH-MDZ were quantified under single reaction monitoring mode using specific precursor/product ion transition. The mass transition for 1'-OH-MDZ was m/z 342→168.1 at a collision energy of 40 V. The mass transition for d4-1'-OH-MDZ was m/z 346→168 at a collision energy of 44 V.

Chromatographic separation of the 13-DMT extract was achieved using a reverse-phase column (Zorbax Eclipse XDB C8, 3 mm x 150 mm x 5 µm; Agilent, Santa Clara, CA) operated at 60°C. The aqueous (A) mobile phase consisted of 10 mM ammonium formate and 0.1 mM sodium acetate (pH = 7). The organic (B) mobile phase consisted of 100% methanol with 0.1 mM sodium acetate. The gradient for the mobile phases was: (1) mobile phase A was set to 40% at 0 min at a total flow of 0.3 mL/min, (2) a linear gradient to 10 minutes decreased phase A to 10%, (3) mobile phase A was increased back to 40% by a linear gradient from 11 to 11.1 minutes, which was maintained for the remainder of the run. Total run time was 12.5 minutes per sample. 13-DMT and rapamycin were quantified under single reaction monitoring mode using specific precursor/product ion transition. The mass transition for 13-DMT was m/z 812.5→602.3 at a collision energy of 36 V. The mass transition for rapamycin was m/z 936.4→409.3 at a collision energy of 60 V.

2.3.6 Data Analysis

For the IC_{50} shift experiment, an IC_{50} model, assuming classical Michaelis-Menten kinetics, was fitted to the metabolite formation rate data and statistical significance of the shift in

IC_{50} estimates was ascertained by an unpaired t-test using GraphPad Prism Version 5.04 (La Jolla, CA). The observed data points and model predictions were normalized to vehicle control and graphically presented as percentage activity versus inhibitor concentration plots.

For the NADPH dependence and reversibility experiment, the mean data for each of the experiments was normalized to the mean of their respective vehicle control incubations. The control groups used were identical to the co-incubations except that vehicle (0.3% DMSO) was added instead of telaprevir. The two means of the experimental and control groups were assumed to be independent. The standard deviation of the ratio was calculated utilizing a propagation of error equation.[81] The resultant means and standard deviations of the ratios for the three incubation groups were then compared (0 vs 15 min, 0 vs 30 min, 15 vs 30 min) using an unpaired t-test on QuickCalcs software (GraphPad, La Jolla, CA) with a $p < 0.05$ assigned as statistically significant.

2.4 Results

2.4.1 Competitive Inhibition Modeling

Model predictions for the various inhibition scenarios precipitated by telaprevir are presented in Table 2.1, along with the reported magnitude of interactions with midazolam and tacrolimus.[67, 73] Our static DDI modeling indicates that competitive inhibition by telaprevir and its diastereomeric metabolite VRT-1237394 cannot fully explain the profound inhibitory interactions observed with either midazolam or tacrolimus. With respect to competitive inhibition of orally administered midazolam clearance, an approximate 2.6- to 4.2-fold reduction in clearance was predicted for the “least” inhibition scenario. The magnitude of this reduction increased to 3.7- to 5.2-fold for the “maximum” inhibition scenario. In our “extreme” scenario,

where all of the dose is completely absorbed and escapes first-pass extraction, a 5.3- to 7.2-fold reduction in apparent oral clearance of midazolam might be observed. Predictions for all three competitive inhibition scenarios fell short of the 13.5-fold decrease in midazolam oral clearance observed by *Garg et al*.[73]

For the predicted interaction with tacrolimus, an approximate 3.0- to 6.2-fold reduction in oral clearance was predicted in the "least" inhibition scenario. A 9.2- to 14-fold reduction in oral clearance was observed for the "maximum" inhibition scenario, and a 14- to 21-fold reduction was predicted in the "extreme" scenario where total administered dose is absorbed and escapes first-pass processes. Here again, the predictions of all three competitive inhibition scenarios fell short of the observed interaction of 67-fold reduction in tacrolimus oral clearance.[67]

Table 2.1. Summary of Static DDI Model Predictions

Parameter	Midazolam	Tacrolimus
F_a	0.90*	0.96*
F_g	0.51*	0.14*
$F_{g,inh}$ (least)	0.68 to 0.77	0.23 to 0.31
$F'_{g,inh}$ (maximum)	0.94 to 0.94	0.70 to 0.71
F_h	0.67*	0.97*
$F_{h,inh}$ (least)	0.79 to 0.85	0.98 to 0.99
$F'_{h,inh}$ (maximum)	0.82 to 0.85	0.99 to 0.99
F_{total}	0.25*	0.13*
$F_{total,inh}$ (least)	0.49 to 0.59	0.22 to 0.30
$F'_{total,inh}$ (maximum)	0.69 to 0.72	0.66 to 0.68
CL_h, L/h	30.0*	2.69*
$CL_{h,inh}$, L/h	19 to 14	1.5 to 0.98
CL_{oral}, L/h	98.0	20.7
$CL_{oral,inh}$ (least), L/h	38 to 23	6.8 to 3.3
$CL'_{oral,inh}$ (maximum), L/h	27 to 19	2.3 to 1.5
$CL_{oral}/CL_{oral,inh}$ (least)	2.6 to 4.2	3.0 to 6.2
$CL_{oral}/CL'_{oral,inh}$ (maximum)	3.7 to 5.2	9.2 to 14
$CL_{oral}/CL_{h,inh}$ (1st pass abolished)	5.3 to 7.2	14 to 21
Observed $CL_{oral}/CL_{oral,inh}$	13.5*	66.7*

*Denotes value taken directly or inferred from the literature;[67, 73, 74, 77] (least) pertains to the scenario governed by purely systemic inhibitor concentrations; (maximum) pertains to the scenario featuring increased local concentrations at sites of first-pass elimination; (abolished) pertains to the "extreme" scenario where first-pass metabolism is abolished.

2.4.2 Time-Dependence of Inhibition

We evaluated telaprevir for time-dependent inhibition (TDI). For both substrates, leftward shifts in their IC_{50} curves were observed following a 30-min pre-incubation with telaprevir (Figure 2.1) suggesting that inhibition of CYP3A is time-dependent. The IC_{50} for midazolam was lowered from 0.74 µM to 0.19 µM, a 3.8-fold shift that was statistically significant ($p < 0.05$). Likewise, the IC_{50} for tacrolimus was lowered from 4.0 µM to 0.36 µM, an 11-fold shift that was also statistically significant. An apparent activation of 13-DMT

formation occurred at lower tacrolimus concentrations in the IC_{50} experiment that was not subjected to pre-incubation. This observation may be explained by allosterism of CYP3A which is not accounted for in the classical IC_{50} model.

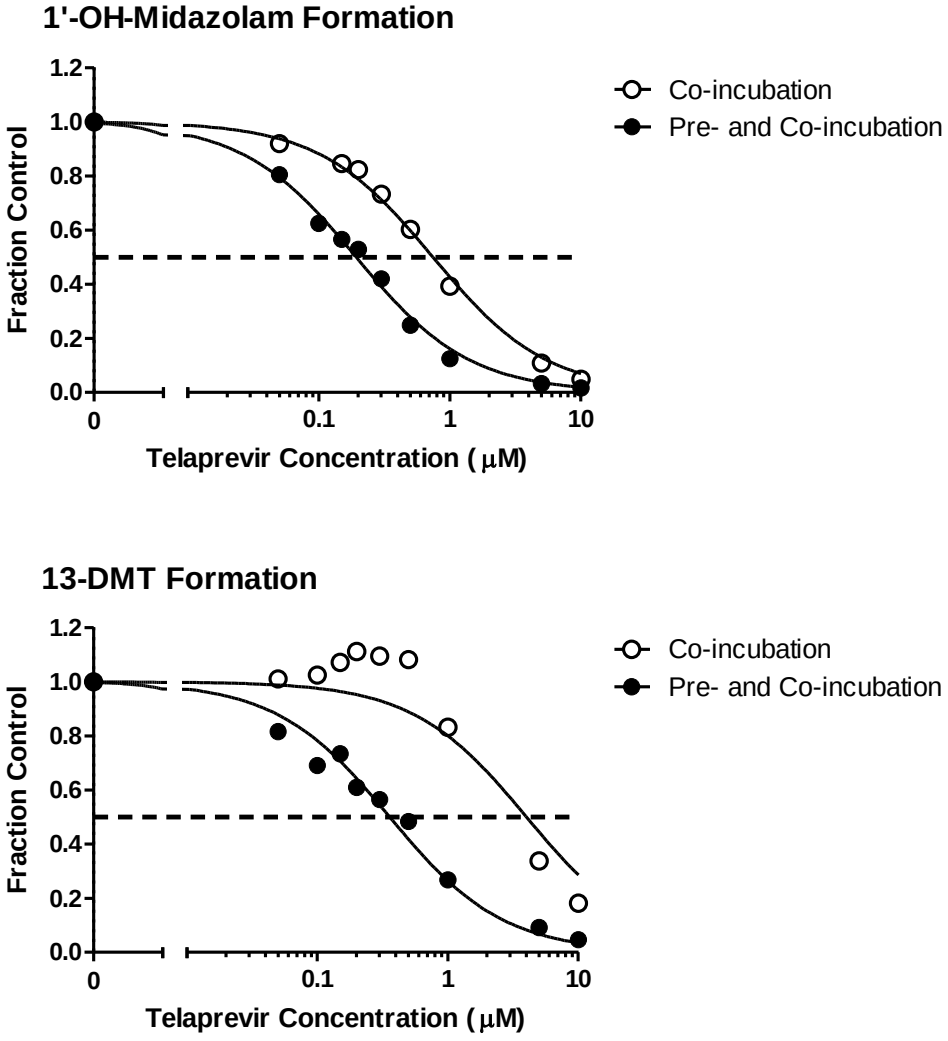

Figure 2.1. Time-dependent inhibition of CYP3A by telaprevir. Comparison of telaprevir IC_{50} curve for the co-incubation experiment (○) versus pre- and co-incubation experiment (●) for midazolam (top) and tacrolimus (bottom). The solid line represents the fit to an IC_{50} model.

2.4.3 Reversibility and NADPH-Dependence of Time-Dependent Inhibition

A TDI was also demonstrated in the follow-up study; the results are depicted in Figure 2.2. As the pre-incubation duration increased, 1'-OH-MDZ formation rate showed a progressive decline provided NADPH was present during pre-incubation. The TDI disappeared when pre-incubations were performed in the absence of NADPH. Pre-incubation with telaprevir also inhibited tacrolimus oxidation to 13-DMT in a time-dependent manner contingent upon the presence of NADPH.

In order to assess whether the observed TDI reflected irreversible inactivation of CYP3A, we performed a dilution experiment. A pre-incubation with telaprevir was performed using a 20-fold higher concentration of HLM; the pre-incubated HLM mixture was then diluted 20-fold prior to substrate incubation. The reporter reaction with either midazolam or tacrolimus in the 0-min telaprevir pre-incubation time-group was comparable to its vehicle control, indicating that competitive inhibition by the concentration of telaprevir in the diluted microsomal incubate was minimal or nearly absent. In the case of midazolam, dilution effectively reversed the inhibition observed after pre-incubation with telaprevir, as indicated by the minimal difference (< 20%) in 1'-OH-MDZ formation rates between zero-time and either 15 or 30 min of pre-incubation. The nature of TDI of tacrolimus oxidation appeared to be more complicated compared to that of midazolam. A reduction in the magnitude of the TDI was indeed observed after dilution; however, a significant component of non-reversible or very slowly reversible inhibition remained. In fact, for the 30 min pre-incubation, the degree of inhibition observed after dilution hardly differed from that observed in the no-dilution group.

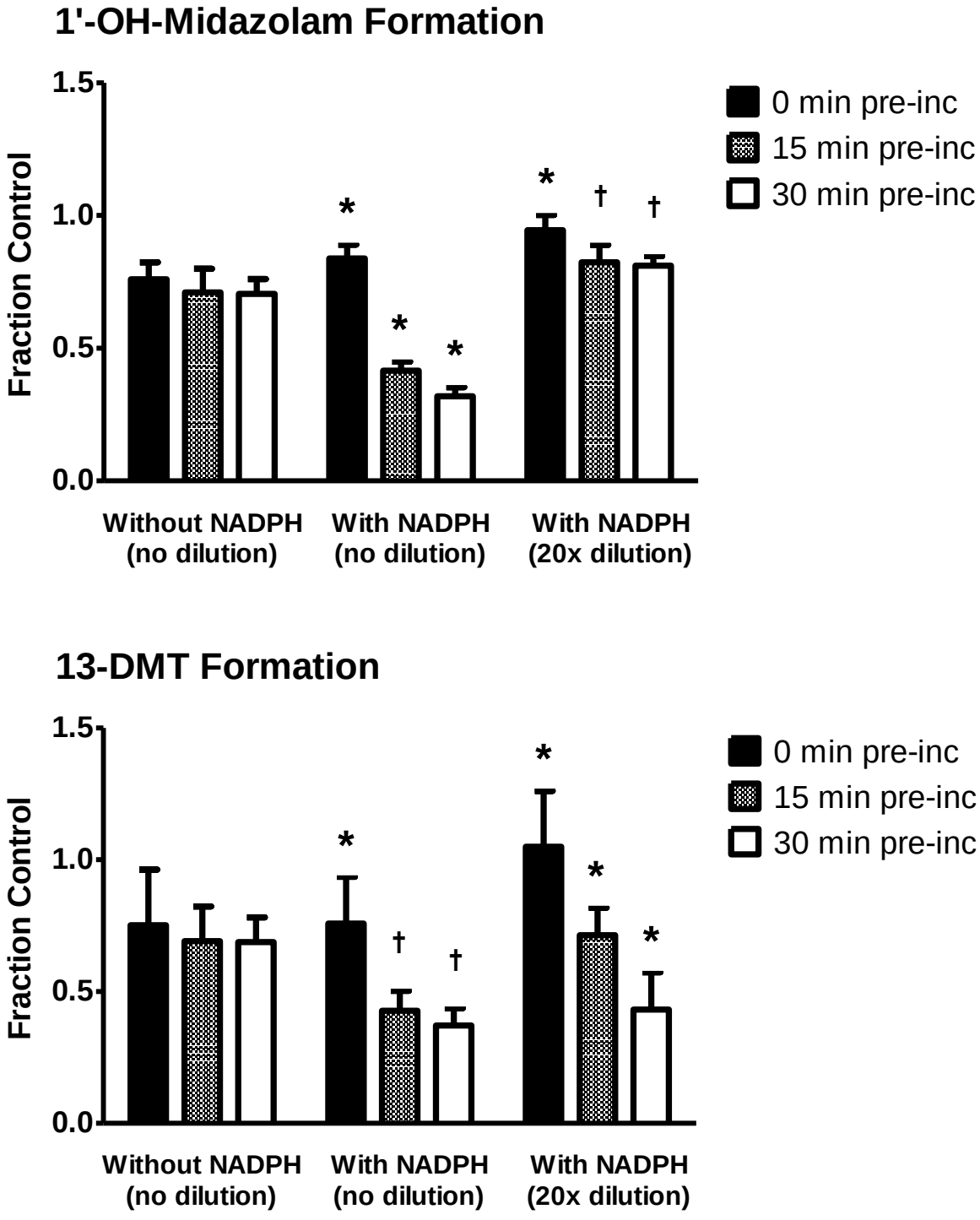

Figure 2.2. Reversibility of telaprevir-mediated time dependent inhibition of CYP3A. Determination of NADPH-dependence and reversibility of time-dependent inhibition of 13-DMT formation (top) and 1'-OH-MDZ formation (bottom) by telaprevir. Error bars represent standard deviation. (*) Denotes statistically significant difference ($p < 0.05$) between the mean of this time point and those of the other time points within a treatment group. † denotes statistically significant difference ($p < 0.05$) between the mean of this time point and mean of the zero-time pre-incubations within a treatment group.

2.5 Discussion

Through the use of established mechanistic static DDI models, we predicted the degree of reduction in oral clearance of two sensitive CYP3A substrates ― midazolam and tacrolimus for the scenario when inhibition mechanism was simply limited to competitive inhibition by the parent drug and its primary metabolite VRT-127394. Our model grossly underestimated the magnitude of telaprevir interactions, even after recognizing the highest possible transient, local inhibitor concentrations in the intestinal mucosa and hepatoportal blood during first-pass. All this was overshadowed by the fact that even when we assumed complete abolition of all first-pass processes (F_{total} = 1), we still failed to predict the magnitude of the observed DDI. This observation is especially instructive in the case of tacrolimus; abolition of first-pass metabolism would at most result in a 21-fold decrease in oral clearance, which is in contrast to the reported 67-fold decrease in a recent healthy human subject study.

Collectively, the competitive inhibition model suggests that 1) profound inhibition must occur during both first-pass and systemic phase of drug clearance; 2) the degree of competitive inhibition estimated based upon the referenced *in vitro* K_i is either inaccurate (i.e., *in vivo* K_i differ drastically from *in vivo* K_i) or presence of other mechanisms of inhibition must be considered; and 3) the mechanism of telaprevir-precipitated interactions is complicated by substrate-dependence (i.e., possibly explained by some sort of reciprocal substrate-inhibitor interaction at the CYP3A binding sites).

There have been reports of putative MBI involving the parent telaprevir. While we were able to confirm the existence of TDI, it was observed to be partially or fully reversible depending on the substrate selected. This reversibility, particularly with midazolam as the CYP3A substrate, casts doubt on parent telaprevir as a mechanism-based inhibitor, and points to the possible

formation of potent, reversibly acting inhibitory metabolites during pre-incubation. Vertex has reported that telaprevir can spontaneously convert to VRT-127394 in circulation; however, we were not able to detect the presence of this diastereomeric metabolite in our incubations without the availability of an authentic standard. We do not believe the formation of VRT-127394 can easily explain the remarkable IC_{50} shift following pre-incubation since the competitive K_i of VRT-127394 is about equal to that of telaprevir.[68] Similar *in vitro* findings of reversible TDI have been reported with another first-generation HCV protease inhibitor, boceprevir.[82] Furthermore, observations of reversible TDI involving cytochrome P450s is not limited to the HCV protease inhibitors. Reversibility in TDI of cytochrome P450s has been reported for both R-fluoxetine and amiodarone,[83] both of which are known to form inhibitory metabolites. Due to the potential for TDI to be of a reversible nature, the importance of incorporating a "dilution" step in experiments to measure the kinetics of enzyme inactivation cannot be overstated. In their *in vitro* study of telaprevir's inhibition of tacrolimus metabolism,[69] *Oda and Yamano* failed to mention the inclusion of a dilution step (or any other means to eliminate the carryover of telaprevir from the pre-incubation) in their MBI experiment for generating estimates of enzyme inactivation parameters k_{inact} and K_I. As a result, their model predictions of the *in vivo* DDI between telaprevir and tacrolimus, based on the assumption of MBI of CYP3A by parent telaprevir, may not be valid. Until we ascertain the exact nature of the TDI, attempts at *in vitro*-to-*in vivo* scaling of drug interactions with telaprevir involving CYP3A is premature.

From a general perspective, the distinction between reversible and irreversible TDI has important clinical implications in regards to the outcomes of DDI. In the case of an irreversible TDI, such as MBI, the time to reach maximum inhibition following addition of the inhibitor and the time it takes for inhibition to dissipate following withdrawal of the inhibitor depends on both

the elimination half-life of the inhibitor as well as the turnover half-life of the enzyme. If the inhibitor has a relatively short half-life as in the case for telaprevir (< 24 hrs), the half-life of the CYP3A protein in the intestinal mucosa and the liver becomes the rate-limiting process. In contrast, if the TDI is reversible and attributable to the formation of a an equally or more potent inhibitory metabolite, the dynamics of inhibition during or post inhibitor treatment will depend on either the elimination half-life of the parent drug if the washout kinetics of the inhibitory metabolite is formation-rate-limited, or the elimination half-life of the inhibitory metabolite if that is rate-limiting for the washout of the metabolite. Hence, the conclusion of an MBI should not be based solely on the observation of TDI in an IC_{50} shift study; assessment of irreversibility in inhibition should always be the critical test of a MBI.

Finally, it is important to recognize that telaprevir could precipitate DDI via non-CYP3A related mechanisms. Specifically, telaprevir is known to inhibit intestinal P-glycoprotein, which has been shown to result in increased in digoxin absorption.[73] It is conceivable that the profound *in vivo* interaction between telaprevir and tacrolimus stems from the simultaneous inhibition of intestinal CYP3A and P-glycoprotein, disrupting the interplay between CYP3A and P-glycoprotein at the intestinal mucosa.[34] However, it should be noted that a complete halt to intestinal metabolism and efflux transport processes still cannot fully account for the magnitude of the observed DDI, as illustrated by the under-prediction of our first-pass "abolition" modeling scenario. Interplay between CYP3A and P-glycoprotein has also been suggested to occur at the bile canaliculi, which may play a role in the hepatic clearance of tacrolimus.[84] Dual-inhibition of CYP3A and P-glycoprotein at the bile canaliculi could have an impact on both first-pass and systemic extraction of tacrolimus by the liver. It is also worth noting that tacrolimus itself has been associated with time-dependent inhibition of CYP3A.[85] Modulation in such tacrolimus-

mediated inhibitory processes could contribute to the magnitude of the observed DDI. The apparent activation of 13-DMT formation seen at low telaprevir concentrations (Figure 2.1) hints at allosteric effects, which could add further complexity to the kinetics of this interaction.

3 Functional Comparison of Intestinal Cells for Investigations of Intestinal Drug Permeability and First-Pass Metabolism

Portions of this chapter were published in Drug Metab Dispos. 2016 Mar;44(3):329-35 under the first-authorship of Dr. Yoshiyuki Yamaura.

3.1 Abstract

To further the development of a model for simultaneously assessing intestinal absorption and first-pass metabolism *in vitro*, Caco-2, LS180, T84 and fSIEC were cultured on permeable inserts and the integrity of cell monolayers, CYP3A4 activity and the induction of enzymes and transporters involved intestinal drug disposition were measured. Caco-2, T84 and fSIEC all formed tight junctions, as assessed by immunofluorescence microscopy for zonula occludens-1 (ZO-1), which was well organized into circumscribing strands in T84, Caco-2 and fSIEC, but was diffuse in LS180 cells. The TEER value for LS180 monolayers was lower than that for Caco-2, T84 and fSIEC. In addition, the apical-to-basolateral permeability of the paracellular marker, lucifer yellow, across LS180 monolayers was higher than in fSIEC, T84 and Caco-2 monolayers. The transcellular marker, propranolol exhibited similar permeability across all cells. With regard to metabolic capacity, T84 and LS180 cells showed comparable basal midazolam hydroxylation activity and it was inducible by rifampin and $1\alpha,25(OH)_2D_3$ in LS180 cells, but only marginally so in T84 cells. The basal CYP3A4 activity of fSIEC and Caco-2 cells was much lower and not inducible. Interestingly, some of the drug transporters expressed in LS180 and Caco-2 cells were induced by either $1\alpha,25(OH)_2D_3$ or rifampin or both, but there were only limited effects in the other two cell lines. These results suggest that when cultured under conventional 2-dimensional conditions, none of the cell lines tested fully replicated the drug disposition properties of the small intestine and that the search for an ideal screening tool must continue. Encouraged by observations of more *in vivo*-like phenotype of primary human proximal tubule epithelial cells in 3-dimensional microfluidic platforms, preliminary investigations were undertaken to evaluate whether primary fSIECs would also adopt a more *in*

vivo-like phenotype and further progress towards a more faithful recapitulation of intestinal drug absorption processes.

3.2 Introduction to Chapter 3

Within the pharmaceutical industry, the oral bioavailability of lead compounds is frequently optimized by enhancing intestinal permeability and reducing first-pass metabolism. Caco-2 cell monolayers are routinely used as an *in vitro* intestinal permeability screening model. The permeability of drugs across Caco-2 monolayers has been shown to correlate well with the percent of drug absorbed in humans for both passively absorbed and actively transported compounds.[86, 87] However, Caco-2 cells do not robustly express CYP3A4 under standard culturing conditions.[88] CYP3A4 metabolizes a wide range of chemically diverse compounds. Moreover, the enzyme is the most abundant drug-metabolizing P450 in the small intestine and participates in first-pass metabolism of drugs.[7, 8] Consequently, CYP3A4 is an important enzyme when considering the potential for drug-drug interactions (DDIs) at the site of the intestinal epithelium.[89]

The deficiency of CYP3A4 expression in Caco-2 cells makes them a poorly suited model for studying intestinal first-pass metabolism and DDIs. To resolve this deficiency, some groups have tried to transfect Caco-2 cells with CYP3A4 cDNA.[90, 91] However, the resultant expression of CYP3A4 protein was relatively low and unstable in these transfected cells. It has also been reported that CYP3A4 expression levels can be induced by treatment of a Caco-2 cell subclone with $1\alpha,25(OH)_2D_3$.[88] This model has been used to examine first-pass metabolism of midazolam and saquinavir.[92, 93] However, CYP3A4 expression in these cells is still relatively low compared to human duodenal mucosa.[8, 92] Furthermore, these Caco-2 subclones require culturing for an additional two weeks post confluence in order for induction and differentiation to occur. As such, experiments using these cells can be time-consuming and not compatible with high-throughput screening of numerous compounds. Additionally, the baseline-induced Caco-2

subclone does not undergo further induction of CYP3A4 by rifampin or other prototypical inducers.[35]

Other colonic carcinoma cells lines such as LS180 and T84 cells could potentially provide a viable alternative for simultaneously assessing the intestinal permeability and first-metabolism of drugs. Although LS180 cells exhibit basal and inducible CYP3A4 activity,[94] they are thought not to form tight junctions in culture. In contrast, T84 cells are known to form tight junctions.[95] However, expression of CYP3A4 by T84 cells is controversial and its inducibility has not been reported.[96, 97] It is worth noting that this cell line expresses pregnane X receptors (PXR), which is one of the important nuclear transcription factors mediating CYP3A4 induction. Additionally, induction of the efflux transporter P-glycoprotein (MDR1) been observed in T84 cells treated with the PXR ligand, rifampin.[98]

The growing commercial availability of primary human fetal small intestinal epithelial cells (fSIEC) provides a unique alternative to immortal colon cancer cell lines. While some work has been done to characterize the pharmacokinetic properties of both stem-cell derived and primary human intestinal epithelial cells,[99] little is known about the metabolic properties with respect to CYP3A4 activity. Additionally, it is not known whether the primary human intestinal cells evaluated in the literature are specifically sourced from the small intestine or if they originate from the colon.

In this chapter, we evaluated LS180, T84, Caco-2 and human fSIEC to further the development of an *in vitro* model for the simultaneous assessment of intestinal permeability and first-pass metabolism. To characterize these cells, we examined TEER, tight junction protein localization, CYP3A4-mediated metabolism and induction of mRNA transcripts coding for proteins related to intestinal drug disposition. We then further evaluated whether human fSIECs

could be cultured under fluid sheer stress in a 3-dimensional environment as preliminary assessment of their suitability for incorporation in a small intestinal microphysiological system (SI-MPS).

3.3 Materials and Methods

3.3.1 Chemicals and Reagents

Rifampicin, 5-aza-2'-deoxycytidine (5-aza-dC), bovine serum albumin, cell dissociation solution for LS180 cells, PCR primer pairs (BCRP, MDR1, MRP2 and OCT1), HBSS, HEPES buffer, Triton X-100, propranolol, atenolol and furosemide were purchased from Sigma-Aldrich (St. Louis, MO). D-Sucrose was obtained from Fisher Scientific (Itasca, IL). 16% Formaldehyde (methanol free) was purchased from polysciences (Warrington, PA). $1\alpha,25(OH)_2D_3$ was obtained from Calbiochem (La Jolla, CA). MDZ, d4-MDZ and d4-1´-OH MDZ were purchased from Cerilliant (Round Rock, TX). 1´-OH MDZ was purchased from Ultrafine (Manchester, UK). DPBS, DPBS^{++}, MEM, DMEM/F12, DMEM, penicillin-streptomycin, NEAA, TRIzol reagent, High Capacity cDNA Reverse Transcription Kit with RNase Inhibitor, Power SYBR green PCR master mix, PCR primer pairs (CYP3A4, GAPDH, PXR, UGT1A1 and VDR), Rabbit anti-ZO-1 antibody (cat#402200), Alexa Fluor 488 Donkey anti-rabbit IgG, Alexa Fluor 594 Donkey anti-rabbit IgG, ProLong Gold Antifade reagent with DAPI and lucifer yellow biocytin were obtained from Life technologies (Carlsbad, CA). Mouse anti-CYP3A antibody was purchased from Santa Cruz Biotechnology (Dallas, TX). Rabbit anti-villin and mouse anti-sodium potassium ATPase (Na^+/K^+ATPase) were obtained from abcam (Cambridge, UK). FBS was purchased from Atlanta Biologicals (Lawrenceville, GA). Sodium pyruvate and Trypsin EDTA were purchased from Cellgro (Herindon, VA). Cell dissociation solution for fSIEC, epithelial pro-conditioned media

and vessel coating solution were purchased from DV Biologics (Costa Mesa, CA). Wide bore microfluidic platforms were custom made and provided by Nortis (Woodinville, WA).

3.3.2 Statistical Analysis

Data are presented as mean ± S.D. The effect of rifampicin and 1α,25$(OH)_2D_3$ on midazolam 1´-hydroxylation and mRNA expression levels was assessed by comparison to vehicle controls and presented as the mean ± S.D.. Overall standard deviation for ratios of two means with independent standard deviations was calculated using a propagation of error equation. Statistical significance ($p < 0.05$) was determined via unpaired t-tests. All statistical analyses were conducted using GraphPad Prism version 5.04 (GraphPad Software, La Jolla, CA).

3.3.3 Cell Culture in Transwell Inserts

LS180 (passage 25-34), T84 (passage 56-66) and Caco-2 cells (passage 26-35) were obtained from American Type Culture Collection (Manassas, VA). fSIEC, 14.9 weeks gestational age, were obtained from DV Biologics (Costa Mesa, CA) and experiments were conducted at passage 3-8. Cells were maintained at 37°C in a humidified incubator with 5% CO_2. LS180 cells were cultured in MEM supplemented with 10% FBS, 1% penicillin-streptomycin and 1% sodium pyruvate. T84 cells were cultured in DMEM/F12 supplemented with 10% FBS and 1% penicillin-streptomycin. Caco-2 cells were cultured in DMEM supplemented with 10% FBS, 1% penicillin-streptomycin and 1% NEAA. fSIEC were cultured in epithelial pro-conditioned media (DV Biologics, Costa Mesa, CA, cat#D-Pro-015-100). The cells were passaged by addition of cell dissociation solutions (for LS180 and fSIEC) or trypsin EDTA (for T84 and Caco-2) at 80% confluence. Cells were seeded onto polyethylene-terephthalate, 0.4 µm

pore size filter inserts for 24 well plates (0.3 cm^2 growth area (BD Biosciences, Franklin Lakes, NJ, cat#353095), or 0.336 cm^2 growth area (Greiner bio-one, Monroe, NC, cat#662641) at a density of 5×10^5 cells/cm^2 and maintained by changing medium two or three times a week. For the experimental treatment, the medium was removed and the cells were washed twice with $DPBS^{++}$ and then treated with medium containing the compound or vehicle for 48 hours. Stock solutions of rifampicin (50 mM) and $1\alpha,25(OH)_2D_3$ (1 μM) were prepared in DMSO and ethanol, respectively and were diluted 1000-fold in medium. All FBS used during experimental treatment was resin-charcoal-treated. To examine epigenetic mechanisms, T84 cells were treated with vehicle (0.1% DMSO) or 5-aza-dC at concentrations of 0.2 to 20 μM for 24 hours before treatment with rifampicin and $1\alpha,25(OH)_2D_3$.

3.3.4 CYP3A Activity Assessment

After an experimental treatment, cells were washed twice with $DPBS^{++}$, then 0.3 mL of culture medium containing midazolam (MDZ) at a final concentration of 8 μM (0.1% DMSO) was added to the filter insert (apical compartment) and 0.7 mL of medium without MDZ was added to the basolateral compartment. The cells were incubated for 60 min, then apical and basolateral media were collected and stored at -80°C. MDZ and 1´-OH MDZ were measured using LC-MS/MS on an Agilent 6410 QQQ equipped with HPLC1290 system (Agilent Technologies, Palo Alto, CA). After thawing, 10 μL of each sample (apical samples were 5-fold diluted with blank media) were mixed with 20 μL of methanol and 100 μL of internal standard (ISTD) solution containing 5 ng/mL d4-MDZ and 10 ng/mL d4-1´-OH MDZ in acetonitrile. A series of dilutions of MDZ and 1'-OH MDZ standards were prepared in methanol as stock solutions and stored at -80 °C. The standard curve samples were prepared by mixing 10 μL of

each these stock solutions and 10 μL of blank medium, and then adding 100 μL of ISTD solution. The samples were then centrifuged for 5 min at 12,000 x *g* and 10 μL of the supernatant was analyzed via LC/MS-MS. Chromatographic separations were achieved with a Zorbax SB-C18, 5 μm, 2.1×150 mm column (Agilent Technologies) using 10 mM ammonium acetate (pH 4.0) (A) and acetonitrile (B) as a mobile phase. The flow rate was 0.25 mL/min with a gradient as follows: 45% B for 1.5 minutes, then increased to 80% linearly over 2.5 minutes, held at 80% for 2 minutes, then equilibrated back to 45% for 2 minutes. The following MRM transitions were monitored: m/z 326.0 > 291.2 for MDZ, m/z 330.0 > 295.0 for d4-MDZ, m/z 342.0 > 168.1 for 1'-OH MDZ and m/z 346.0 > 168.0 for d4-1'-OH MDZ in the positive ion mode.

3.3.5 RNA Isolation and qRT-PCR Analysis

After experimental treatment, cells collected from each insert were homogenized in 0.25 mL of TRIzol reagent and stored at -80°C. Total cellular RNA was isolated according to the manufacturer-supplied protocol for TRIzol reagent. The isolated RNA was dissolved in nuclease-free water and the concentration was determined using a Nanodrop spectrophotometer ND-1000 (Thermo Scientific, Wilmington, DE). Reverse transcription was performed according to the manufacturer's instructions for the high capacity cDNA reverse transcription kit. For each reaction, 2 μg of isolated RNA was mixed with dNTP, random hexamer primers, RNase inhibitor and MultiScribe reverse transcriptase in reaction buffer in a total volume of 20 μL. The reverse transcription condition was set as 25°C for 10 minutes, 37°C for 120 min and 85°C for 5 seconds, using a PTC-200 DNA engine cycler (Bio-Rad, Hercules, CA). qRT-PCR was performed using gene-specific primers and the Power SYBR green master mix with a ABI 7900HT system (Applied Biosystems, Bedford, MA). The PCR mixture consisted of 1 μL of

cDNA, gene-specific forward and reverse primers (20 pmol each), Power SYBR green master mix and nuclease-free water, in a total volume of 20 µL for each reaction. The following program was used: a denaturation step at 95°C for 10 min, 40 cycles of PCR (denaturation 95°C for 30 seconds; annealing 65°C for 30 seconds; and extension 72°C for 30 seconds), followed by 72°C for 5 minutes and then a dissociation/melting step (95°C for 15 seconds, 65°C for 15 seconds, 95°C for 15 seconds, 25°C for 5 minutes). All tested gene products were quantified using the comparative ΔΔCt calculation for relative quantification of gene expression, normalized to glyceraldehyde 3-phosphate dehydrogenase (GAPDH).

3.3.6 Immunocytochemistry and Confocal Microscopy of Cells Cultured in Transwell Inserts

Cell monolayers grown on filter inserts were washed twice with $DPBS^{++}$, fixed in 4% formaldehyde in $DPBS^{++}$ containing 2% D-sucrose for 15 minutes at room temperature, washed twice with $DPBS^{++}$ and then incubated in 50 mM ammonium chloride for 30 minutes to quench unreacted aldehyde groups. The cells were washed twice more with $DPBS^{++}$ and then blocked and permeabilized in PTB for 30 minutes. Subsequently, the cells were incubated with a 500-fold dilution of primary antibody (rabbit anti-ZO-1) in PTB for 30 minutes at room temperature or overnight at 4°C. The cell monolayers were then washed three times with $DPBS^{++}$ and incubated with a 1000-fold dilution of fluorescently-conjugated secondary antibody (Alexa Fluor 488 Donkey anti-rabbit IgG) in PTB for 30 minutes at room temperature. After washing with $DPBS^{++}$ three additional times, the filters were cut out from their plastic inserts and placed on glass microscope slides. The inserts were then mounted with ProLong Gold Antifade reagent with DAPI and analyzed on a Nikon A1 confocal microscope (Nikon, Melville, NY).

3.3.7 TEER Measurement

Cell monolayer integration was evaluated by measuring the TEER using a Millicell ERS (Millipore, Bedford, MA). For a given set of cultures, a single filter insert without cells was measured for background resistance. TEER was determined as the product of the background-corrected resistance and the growth area of the insert.

3.3.8 Assessment of Permeability

The cell monolayers were washed with transport buffer (10 mM HEPES in HBSS, pH 7.4) and maintained at 37°C until use. Stock solutions of test compound (lucifer yellow (60 mM), propranolol (20 mM) and atenolol (60 mM)) were prepared in DMSO and diluted 200-fold in transport buffer to make compound solution (final concentrations were 300 µM, 100 µM and 300 µM, respectively). For the lucifer yellow permeability measurement, 0.3 mL of compound solution was added to filter insert, while 0.7 mL of receiver buffer (transport buffer containing 0.5% DMSO) was added to the basolateral compartment. After 60 min incubation at 37°C, 300 µL of aliquots were withdrawn from basolateral compartment. The samples were analyzed by fluorescence detection using a Spectra MAX-Gemini XS microplate reader (Molecular Devices, Sunnyvale, CA) with excitation filter at 485 nm and emission filter at 538 nm. For propranolol and atenolol permeability measurements, 0.32 mL of the respective compound solution was added to filter inserts, while 0.7 mL of receiver buffer was added to the basolateral compartments. 20 µL of aliquots were withdrawn from the insert at 0 min, 70 µL of aliquots were withdrawn from the basolateral compartment and replaced with an equal volume of receiver buffer: at 15 to 60 min for propranolol; at 60 to 120 min for atenolol. Then 20 µL of

aliquots were withdrawn from the insert. The samples were stored at -80□C until analysis. Propranolol and atenolol were measured using LC-MS/MS on an Agilent 6410 QQQ equipped with UPLC1290 system. After thawing, 50 µL of samples (apical samples were 100-fold, basolateral samples of propranolol were 5-fold diluted with blank receiver buffer) were mixed with 50 µL of ISTD solution (furosemide, 25 µg/mL in acetonitrile). A series of dilutions of propranolol and atenolol standards were prepared in methanol as stock solutions and stored at -80°C. The standard curve samples were prepared by mixing 5 µL of stock solution and 50 µL of blank receiver buffer, and then mixed with 50 µL of ISTD solution. 20 µL of the samples was analyzed. Chromatographic separations were achieved with a Zorbax SB-C18, 5 µm, 2.1 × 150 mm column (Agilent Technologies) using 10 mM ammonium acetate (pH 4.0) (A) and acetonitrile (B) as a mobile phase. The flow rate was 0.25 mL/min with a gradient as follows: 25% B for 1.5 minutes, then increased to 75% linearly over 2 minutes, held at 75% for 4.5 minutes, then equilibrated back to 25% for 4 minutes. The following MRM transitions were monitored: m/z 260.31 > 116.1 for propranolol, m/z 267.31 > 145 for atenolol in the positive ion mode, m/z 329.7 > 285.9 for furosemide in the negative ion mode.

The P_{app} (cm/s) for each marker compound was calculated according to following equation:

$$P_{app} = \frac{dQ}{dt} \cdot \frac{1}{AC_0}$$

where dQ/dt is the rate of compound transfer (pmol/s) into the basolateral compartment under sink conditions (where less than 20% of the compound was transferred across the cell

monolayer), A is the surface area of the filter insert (cm^2), and C_0 is the initial concentration of the compound in the apical compartment.

3.3.9 Preliminary Characterization of fSIECs Cultured in Wide Diameter Three-Dimensional MPS

As with the preparation of the 0.12 x 6 mm "regular diameter lumen" microfluidic platforms, the 0.43 x 5.8 mm "wide diameter lumen" platforms (model V4.23) were filled with 6 mg/mL rat tail collagen type I on ice and left for 30 minutes at 4°C. The collagen I was then allowed to polymerize at room temperature overnight. On the day of cell seeding, the microfiber mandrel was removed from each platform, leaving behind a hollow channel traversing the collagen I matrix. This channel was treated with a proprietary vessel coating solution from DV Biologics for 1 hour prior to cell seeding. The lumens were then equilibrated for 45 minutes with D-PRO media. In order to constitute a small intestinal microphysiological system (SI-MPS), 2-dimensional confluent monolayers of human fSIECs (passages 4 to 7) were detached from the cell culture flasks (used for cell expansion) by treatment with DV Biologics proprietary cell dissociation solution. The detached cell aggregates were washed with DMEM media containing 10% FBS, centrifuged at 200 g for 5 minutes, and suspended in D-PRO media (4 $\mu L/cm^2$ of originating culture confluent flask

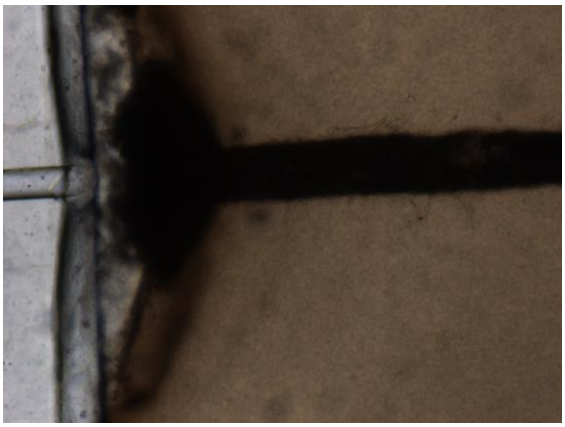

Figure 3.1. Occlusion of regular diameter lumen MPS seeded with fSIECs. Light microscopic image taken 72 hours after injection with fSIECs. Occlusion of lumen and delamination of Collagen I matrix is observed at upstream junction with polydimethylsiloxane inflow channel.

surface area). The suspension of fSIECs was allowed to sit for 5 minutes and 5 μL the upper region of the cell aggregate suspension was injected into custom 0.43 x 5.8 mm "wide diameter lumen" microfluidic platforms from Nortis. The need for customized (model V4.23) wide channel platforms was determined based upon initial observations of rapid channel occlusion following the seeding of fSIECs into 0.12 x 6 mm "standard diameter lumen" microfluidic platforms (Figure 3.1). Cells were allowed to adhere to the coated collagen I matrix for 30 minutes before media flow was reinitiated at 1 μL/min. Cell coverage and integrity of the tubule structure were assessed under light microscopy daily. At 6 days, SI-MPS were fixed with 4% paraformaldehyde solution, subjected to ICC staining, and imaged as previously described for the PT-MPS in Chapter 4. A 1:100 dilution of the antibodies for rabbit anti-villin and mouse anti-Na^+/K^+ ATPase were employed. Human fSIECs were also cultured conventional 2-dimensional Transwell® inserts, as described in Section 3.3.3, for ICC comparison of cell polarization. The ICC staining for fSIECs in Transwell® inserts followed the protocol outlined in Section 3.3.6, using a 1:100 dilution for both rabbit anti-villin and mouse anti-Na^+/K^+ ATPase.

3.4 Results

3.4.1 Induction of CYP3A4 Metabolic Activity

The effects of the prototypical PXR ligand, rifampicin, and the VDR ligand, 1α,25$(OH)_2D_3$, on MDZ 1´-hydroxylation in cells cultured on permeable inserts are shown in Figure 3.2. LS180 cells showed basal CYP3A4 activity that was significantly induced by both rifampicin and 1α,25$(OH)_2D_3$ as previously reported.[92] T84 cells showed basal

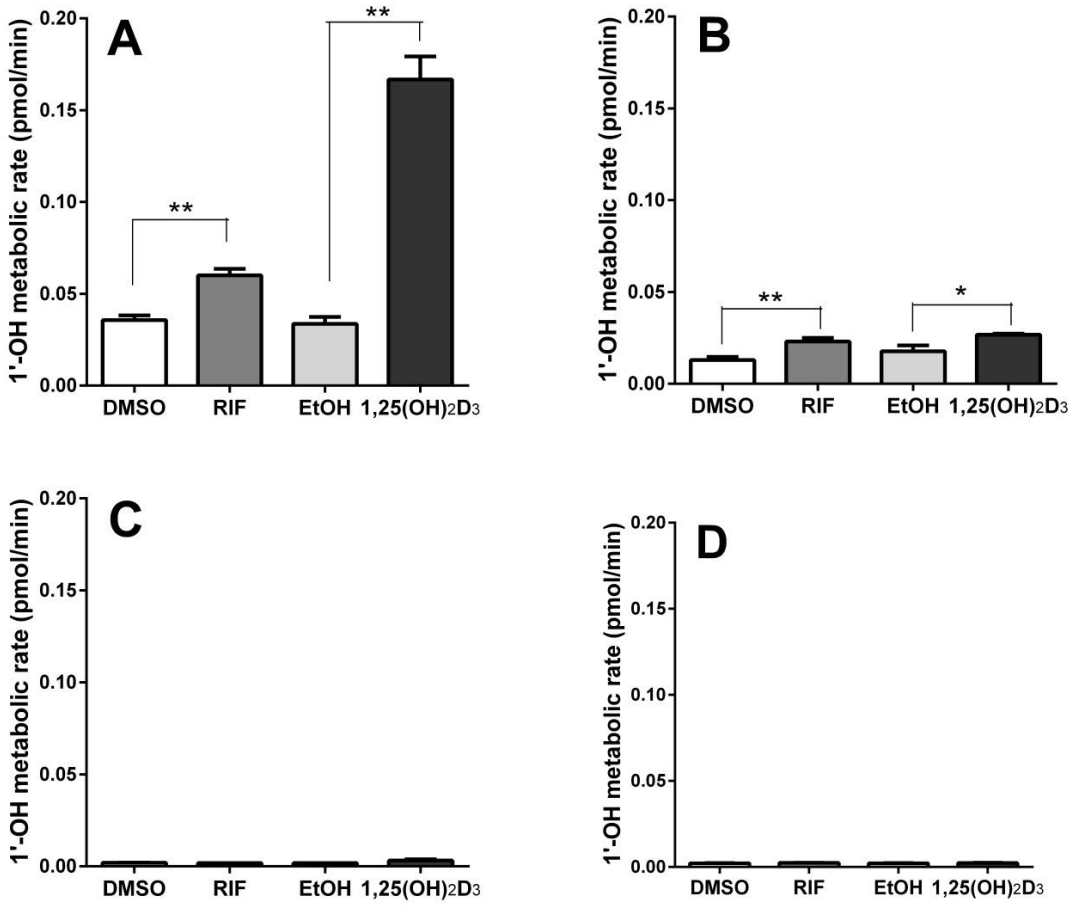

Figure 3.2. Inducibility of CYP3A activity by in intestinal cell lines. Effect of rifampicin (RIF) and 1α,25-dihydroxyvitamin D3 (1α,25$(OH)_2D_3$) on the MDZ 1'-hydroxylation activities in LS180 (A), T84 (B), Caco-2 (C) and fSIEC (D). The cells were cultured on filter inserts for 9 days (fSIEC), 12 days (LS180 and T84 cells) or 19 days (Caco-2) then treated with vehicle (0.1% DMSO or 0.1% ethanol) or inducers (50 μM RIF or 1 nM 1α,25$(OH)_2D_3$) for 48 hours. Data represent the mean ± S.D. for three replicate cultures. *, $p < 0.05$, **, $p < 0.01$

CYP3A4 activity that was comparable to LS180 cells. However, their inducibility through both PXR and VDR pathways was much lower than that seen with LS180 cells. It was confirmed that Caco-2 cells do not possess substantial levels of basal CYP3A4 activity.[86] Furthermore, both rifampicin and 1α,25$(OH)_2D_3$ failed to significantly increase 1´-OH-MDZ formation in Caco-2 cells. Compared to LS180 cells, fSIEC demonstrated similarly low and poorly inducible CYP3A4 activity as that seen for Caco-2 cells.

3.4.2 Induction of mRNA Expression

The effects of rifampicin and 1α,25$(OH)_2D_3$ on gene expression are shown in Figure 3.3. In summary, statistically significant increases in CYP3A4 mRNA was observed with both rifampicin and 1α,25$(OH)_2D_3$ treatment of LS180 cells. There was also a significant induction of MRP2 mRNA observed in LS180 cells treated with 1α,25$(OH)_2D_3$ but not rifampicin. In T84 cells, the only statistically significant change was a 2.2 fold-increase in BCRP mRNA after treatment with rifampicin. We did not observe an induction of MDR1 mRNA transcripts with rifampin treatment, as has been observed previously.[98] Overall, T84 cell response to the inducing agents appeared to be more muted and less variable than the other candidate cells. Furthermore, 5-aza-dC was unable to restore CYP3A4 inducibility (Figure 3.4). Caco-2 cells showed statistically significant 4.5-fold increase in OCT1 mRNA after 1α,25$(OH)_2D_3$ treatment. Caco-2 cells also experienced a statistically significant 17% decrease in UGT1A1 mRNA following treatment with 1α,25$(OH)_2D_3$. In general, the induction of mRNA transcripts in Caco-2 cells appeared to be more sensitive to 1α,25$(OH)_2D_3$ than rifampicin treatment. Finally, a statistically significant 50-fold decrease in BCRP mRNA was observed in fSIEC treated with 1α,25$(OH)_2D_3$.

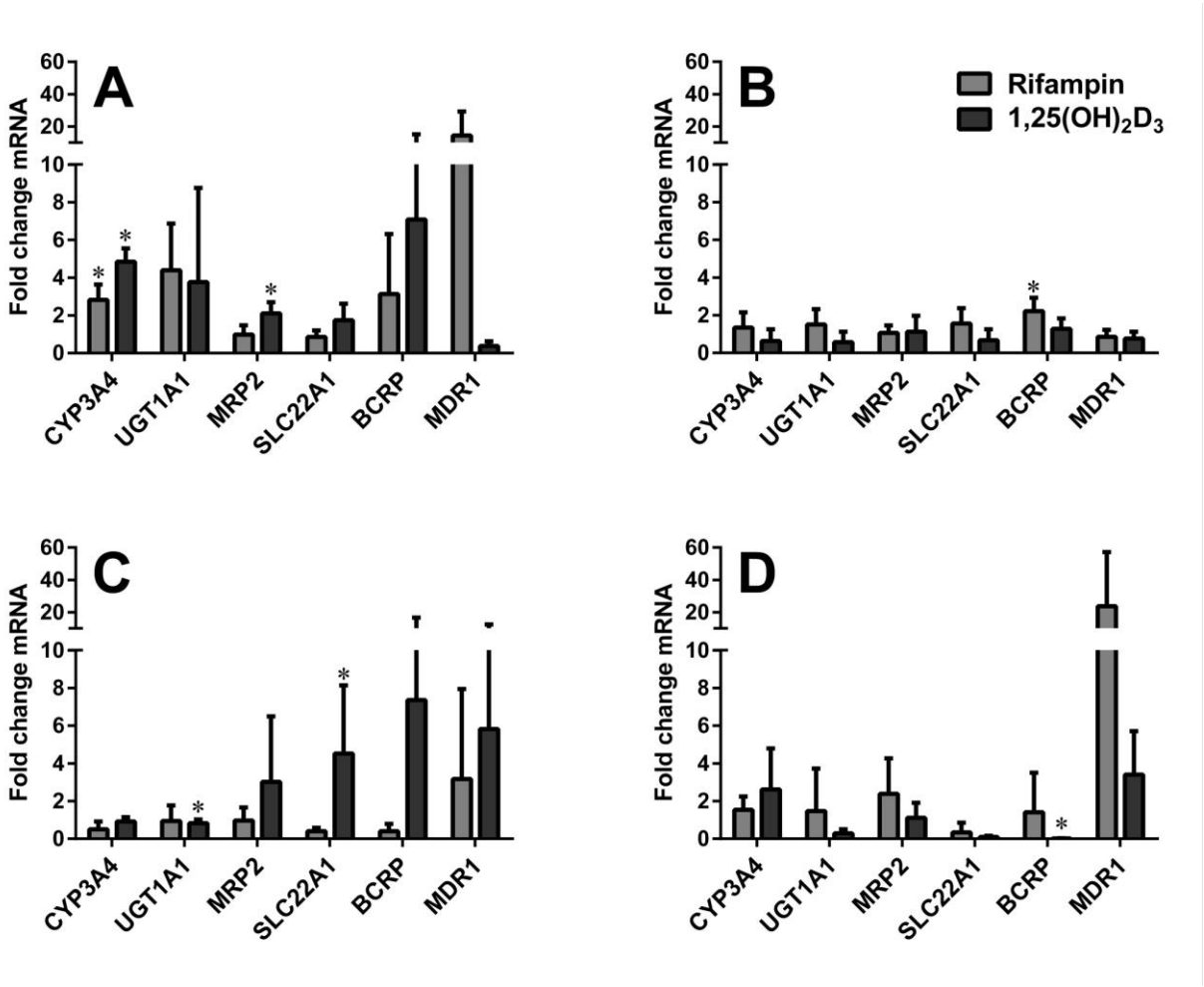

Figure 3.3. Inducibility of gene expression for drug metabolizing enzymes and transporters in intestinal cell lines. Effects of rifampin (RIF) and 1α,25-dihydroxyvitamin D3 (1α,25$(OH)_2D_3$) on mRNA expression in LS180 (A), T84 (B) Caco-2 (C) and fSIEC (D) cells. The cells were cultured on permeable filter inserts for 9 days (fSIEC), 12 days (LS180 and T84 cells) or 19 days (Caco-2) then treated with vehicle (0.1% DMSO or 0.1% ethanol) or inducers (50 μM RIF or 1 nM 1α,25$(OH)_2D_3$) for 48 hours. Data are presented as a ratio of the GAPDH-normalized measurements obtained with inducer treatment compared to the vehicle (0.1% DMSO or 0.1% ethanol) treatment for 3 replicate cultures of both vehicle and inducer treatment groups. Error bars represent the standard deviation of the induction ratio as determined via a propagation of error calculation.[81] (*) Indicates statistical significance ($p < 0.05$) of the induction effect as determined unpaired t-test comparing treatment to its respective vehicle control.

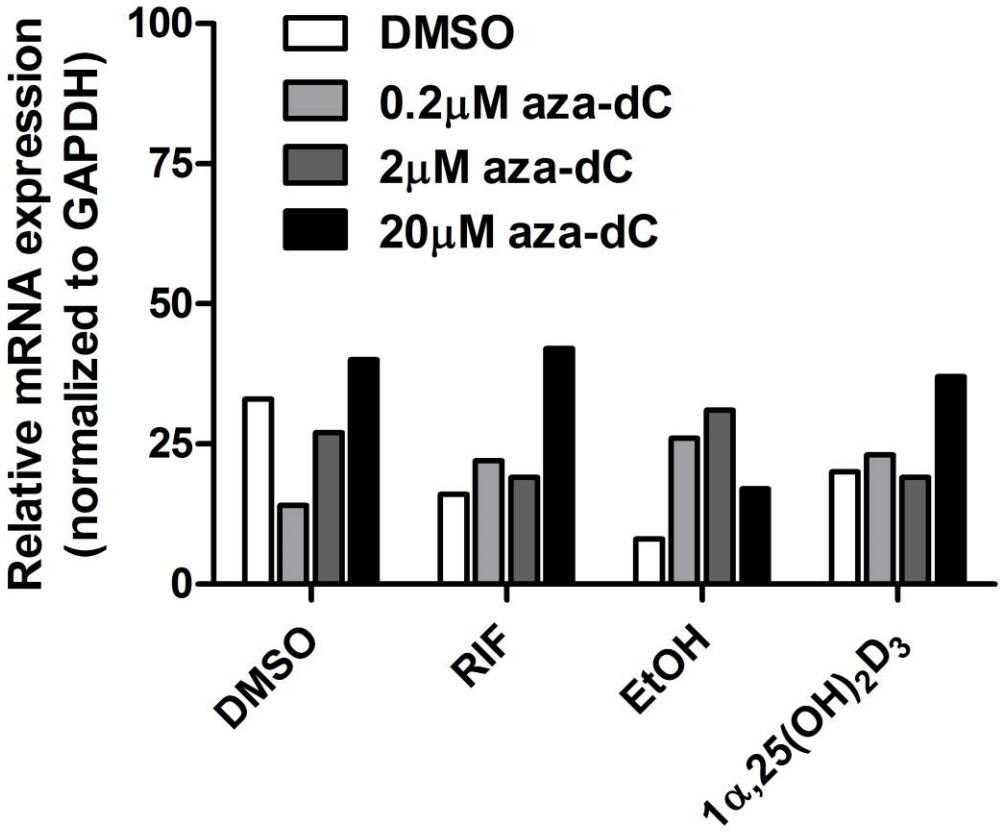

Figure 3.4. Lack of restoration of CYP3A4 inducibility by 5-aza-dC. T84 cells were treated with vehicle (0.1% DMSO) or 5-aza-dC at concentrations of 0.2 to 20 μM for 24 hours before treatment with 50 μM rifampicin, 1 nM $1\alpha,25(OH)_2D_3$, or their respective vehicle controls (ethanol or DMSO). 5-aza-dC did not modulate the effect on CYP3A4 induction, suggesting DNA methylation is not the origin of blunted PXR- and VDR-dependent induction in the cells.

3.4.3 Cell Monolayer and Tight Junction Integrity

The time-dependences of TEER values for three cell lines are shown in Figure 3.5. The TEER values for Caco-2 and T84 cells reached approximately 500 and 2000 $\Omega \cdot cm^2$, respectively, after about 10 days. In contrast, LS180 cells showed much lower TEER values, at about 15 $\Omega \cdot cm^2$ throughout the 18-day experimental period. At 50 $\Omega \cdot cm^2$, TEER values for

fSIEC were slightly higher than LS180 cells. However, integrity of tight junctions appeared to weaken over time in the fSIEC monolayers, dropping closer to that of LS180 cells after 14 days in culture.

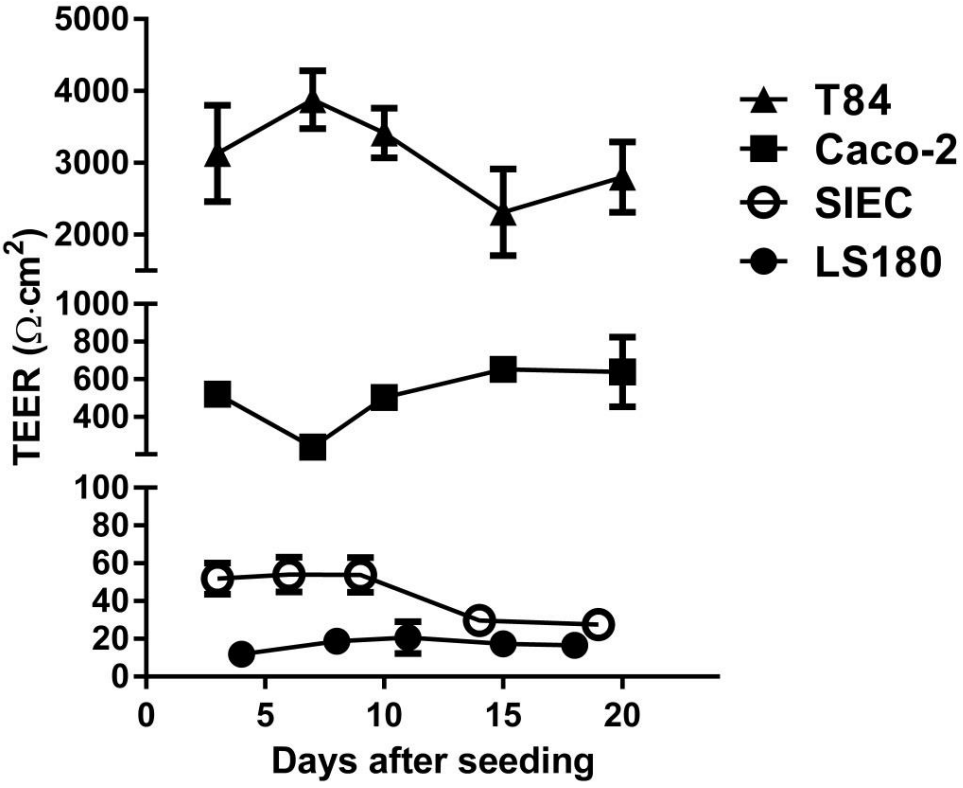

Figure 3.5. Barrier integrity of intestinal cell lines in Transwell culture. Time-dependent transepithelial electrical resistance (TEER) development of LS180, T84, Caco-2 and small intestinal epithelial cells (fSIEC) grown on permeable filter support. Data represent mean ± S.D. for 3 replicate cultures.

Distribution of tight junction protein ZO-1 was well organized into circumscribing strands around fSIEC, T84 and Caco-2 cells, but was more diffuse in LS180 cells (Figure 3.6). An intracellular region showed some stronger signal in the LS180 cells. This could perhaps suggest a Golgi apparatus localization of the protein, but no efforts to confirm this possibility were undertaken.

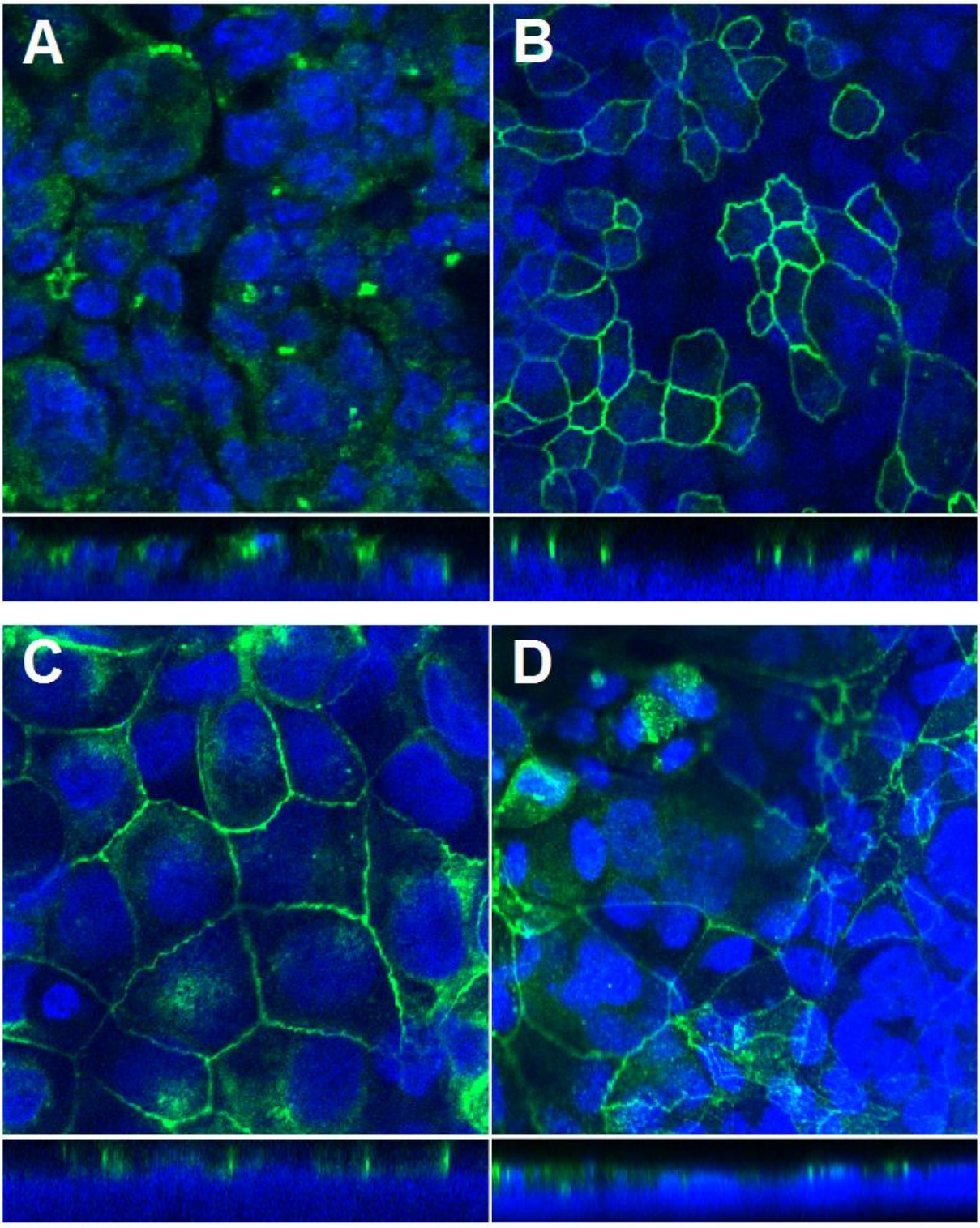

Figure 3.6. Tight junction formation in intestinal cell lines. Cellular localization of tight junction protein ZO-1 in LS180 **(A)**, T84 **(B)**, Caco-2 **(C)** and fSIEC **(D)** by confocal microscopy. The cells were cultured on permeable filter support for 7 days (LS180 and T84), 9 days (fSIEC) or 20 days (Caco-2). The cellular localization of ZO-1 was detected by a rabbit anti-ZO-1 antibody and an Alexa Fluor 488 donkey anti-rabbit IgG secondary antibody (Green). Nuclei were counter-stained with DAPI (Blue).

3.4.4 Drug Permeability

Permeability of the paracellular marker compound, lucifer yellow, was comparably low (less than 1×10^{-6} cm/s) in all cell types except LS180 (Figure 3.7). Propranolol permeability was similar across all 4-cell types. Atenolol permeability was low in T84 and Caco-2 cells but much higher in LS180 and, especially, fSIEC.

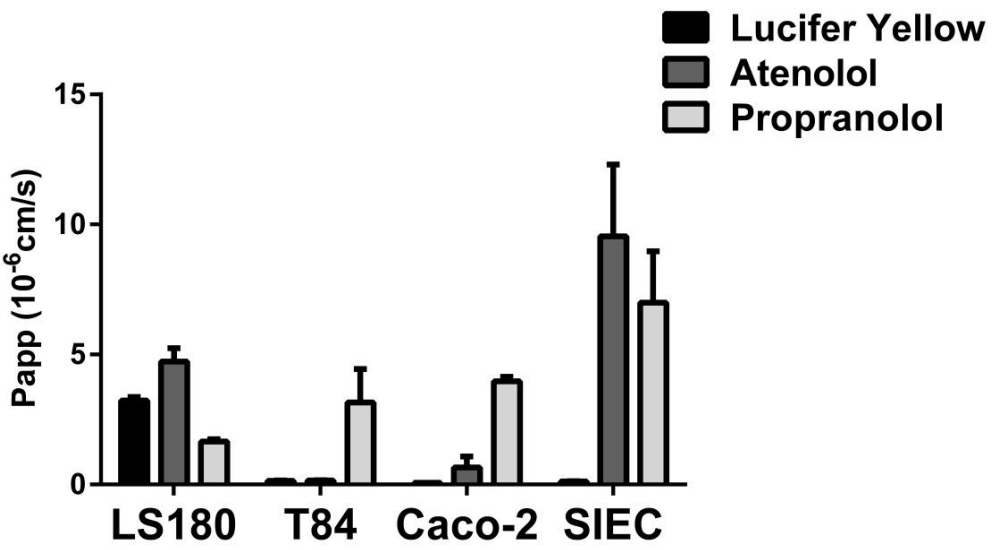

Figure 3.7. Permeability of intestinal cell monolayers to prototypical permeability markers. Permeability coefficients (P_{app}) for the compounds transported by passive diffusion across filter-grown LS180, T84, Caco-2 and small intestinal epithelial cells (fSIEC). The cells were cultured on permeable filter inserts for 7 days (LS180 and T84), 9 days (fSIEC) or 21 days (Caco-2). Data is in arbitrary units and represent mean ± S.D. for three replicate cultures.

3.4.5 Preliminary Characterization of fSIECs Cultured in Wide Diameter Lumen Three-Dimensional MPS

Human fSIECs formed monolayers in traditional 2-dimensional culture as seen in Figure 3.8A. Culture in "wide diameter lumen" microfluidic platforms promoted aggregation and formation of villous-like structures (Figure 3.8B) in addition to patches of relatively flatter monolayers of cells. The villous like structures were approximately 100 µm in length and

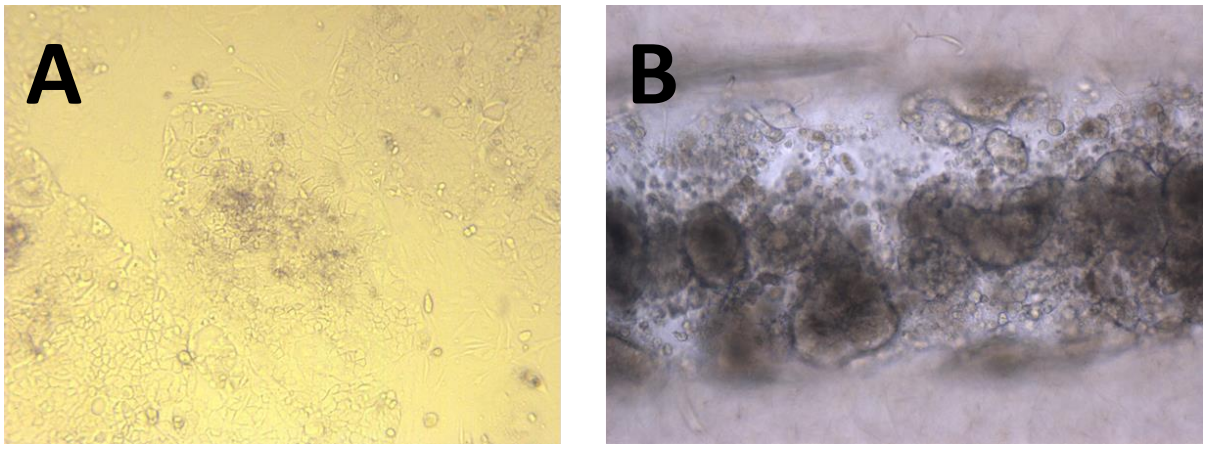

Figure 3.8. Cultures of human fSIECs in flasks and wide-diameter channel SI-MPS. (A) Conventional 2-dimensional human fSIECs at 5 days culture in cell culture flasks. Cells predominantly form monolayers. **(B)** Human fSIECs 24 hours after cell seeding in a "wide diameter lumen" Nortis microfluidic platform. The wide diameter reduces the immediate occlusion of the luminal space. Image was taken from a segment of the lumen where human fSIECs form into characteristic aggregates and villous-like structures (approximately 100 μm in length).

adhered to the collagen matrix. Interestingly, these fSIEC aggregates were oriented with their apical membrane outward, like human small intestinal villi *in vivo*, and unlike the inside-out phenotype describing many enteroids in the published literature (Figure 3.9B).[100, 101] For comparison human fSIECs cultured in 2-dimensional Transwell® inserts formed monolayers and were oriented with apical membranes facing the liquid culture media and basolateral membrane abutting the surface of the extracellular matrix-coated plastic insert membrane (Figure 3.9A).

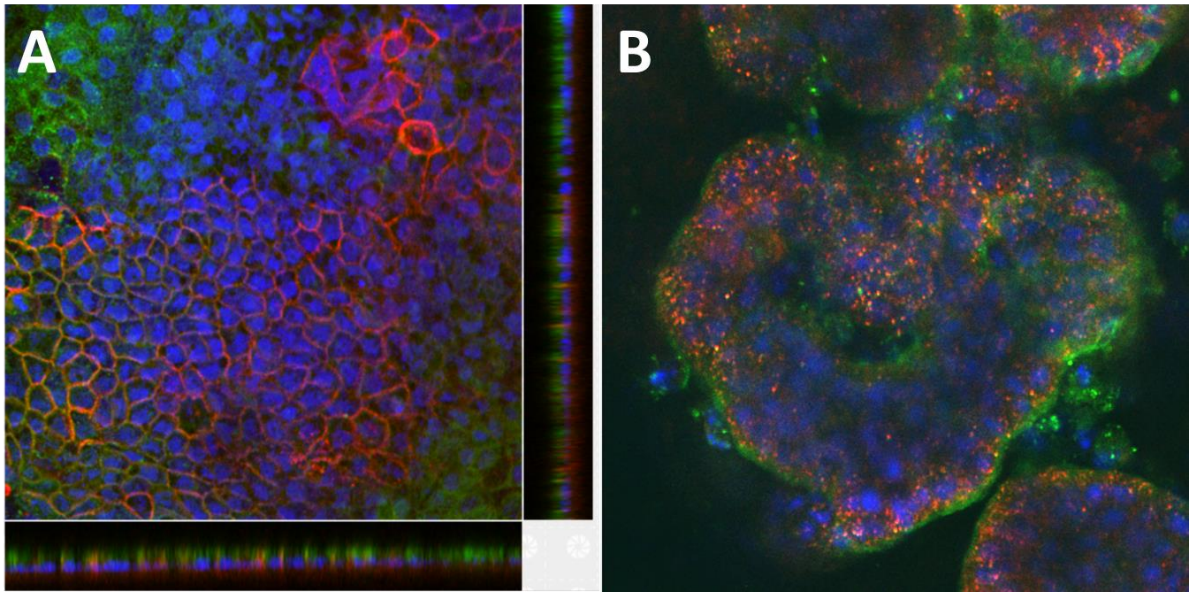

Figure 3.9. Formation of multicellular structures in fSIECs upon culturing in wide-diameter channel SI-MPS
(A) Conventional 2-dimensional human fSIECs at 6 days culture in **(A)** Transwell® inserts express villin (green) preferentially along the apical cell membranes facing the media and sodium-potassium ATPase (red) along the basolateral membranes facing neighboring cells and the extracellular matrix coated plastic filter inserts. **(B)** The villous-like multicellular structure of human fSIECs in the SI-MPS express villin (green) adjacent to the SI-MPS luminal perfusate, analogous to the subcellular localization of villin in the apical membranes of enterocytes of intestinal villi *in vivo*. Sodium-potassium ATPase (red) provides a counterstain for the enterocytes basolateral membranes.

3.5 Discussion

The development of a high-throughput *in vitro* system to simultaneously assess intestinal drug-transport and metabolism is crucial to improving our understanding the role of the intestine in drug disposition. Through the experiments outlined in this paper, we have explored three candidate cell sources (LS180, T84 and fSIEC) as alternatives to the traditional Caco-2 monolayers that have been plagued by poor and variable CYP3A4 enzymatic activity.[88, 90, 91] Our results confirmed the limitations of the monolayers of Caco-2 and LS180 cells. We demonstrated that LS180 cells robustly express CYP3A4 and that such expression is inducible by both rifampicin and $1\alpha,25(OH)_2D_3$. However, their lack of tight junction formation permits an unacceptably high degree of paracellular transport, as evidenced by the permeability of lucifer yellow across LS180 cell monolayers cultured on permeable inserts. The high degree of permeability also seen with the hydrophilic compound, atenolol, is likely due to extensive paracellular flux. While LS180 monolayers may be suitable for drug-metabolism and induction studies, they would not make suitable candidates for the simultaneous assessment of permeability and drug transport and potential functional interplay between those processes. Alternatively, T84 cells seem to express both basal CYP3A4 activity and tight junctions. Monolayers of these cells could theoretically be used to simultaneously explore passive transcellular drug permeability and CYP3A4-mediated metabolism. However, $1\alpha,25(OH)_2D_3$-mediated induction of CYP3A4 activity and mRNA expression in T84 cells was much lower than that of LS180 cells.

To explore the mechanisms underlying a lack of inducibility of T84 cells, we examined epigenetic mechanisms by the treatment of the cells with varying concentrations of the DNA methylation inhibitor, 5-aza-dC. No marked effect on CYP3A4 mRNA expression was observed,

thus further studies are needed to understand this cellular characteristic. A lack of inducibility of CYP3A4 in these cells is a technical limitation, however, they hold potential as an improvement upon Caco-2 monolayers, particularly for compounds where reduced bioavailability from basal CYP3A4-mediated first-pass metabolism is a concern.

As a novel approach, we also explored using fSIEC to recapitulate the intestinal epithelial barrier. We confirmed low CYP3A4 expression in fSIEC as previously reported in fetal proximal small bowel sections and additionally demonstrated that the CYP3A4 was much less inducible by rifampicin and $1\alpha,25(OH)_2D_3$.[102] Low permeability of lucifer yellow, combined with the observation of circumscribing strands of ZO-1 signal upon immunocytochemistry staining, confirmed the presence of tight junctions in fSIEC monolayers. At approximately 50 $\Omega \cdot cm^2$, TEER values for the fSIEC monolayers were substantially less than that of T84 or Caco-2 but strikingly close to the 40 $\Omega \cdot cm^2$ reported for human small intestine in an Ussing chamber.[32] This is in contrast to the slightly higher 100 $\Omega \cdot cm^2$ seen in fSIEC monolayers derived from adult intestinal stems cells or the 200 $\Omega \cdot cm^2$ seen in those derived from induced pluripotent stem cells (iPSC).[99, 103] In addition to iPSC-derived SIEC, *Kauffman et al.* also assessed TEER values in primary human intestinal epithelial cells from an unstated region of the intestine. Monolayers of these primary cells produced a TEER values exceeding 1500 $\Omega \cdot cm^2$, suggesting a colonic, rather than small intestinal phenotype.[104] Despite similar lucifer yellow permeability to T84 and Caco-2 cells, the mean apparent permeability for atenolol was much higher in fSIEC monolayers. This could point to a reduction in transporter-mediated efflux processes or an increase in active uptake of atenolol in fSIEC over T84, Caco-2 or LS180 cells. Despite its very poor permeability, atenolol has a moderate oral bioavailability at 50%.[105] It is also reported that the systemic exposure to atenolol is markedly reduced by apple juice ingestion, a

phenomena attributed to the inhibition of intestinal OATP2B1 by constituents present in apple juice.[106] It is possible that a system possessing more *in vivo*-like expression of uptake transporters could help serve as a useful tool in preventing the needless abandonment of compounds with poor passive permeability, but which would still have sufficient bioavailability *in vivo*. It is also worth noting that while atenolol transport across Caco-2 monolayers was poor, there was a 4.5-fold induction in OCT1 mRNA after treating Caco-2 cells with $1\alpha,25(OH)_2D_3$. Further exploration of inducibility of transporters involved in the uptake of organic cations such as atenolol in traditional Caco-2 cells may be warranted.

As a whole, the experiments outlined herein confirm the poor suitability of both LS180 and Caco-2 cells for the simultaneous assessment of intestinal permeability and first-pass CYP3A4-mediated metabolism. T84 cells may present as a useful cell model for this role but have a shortcoming in their insensitivity to the induction of CYP3A4 by both rifampin and $1\alpha,25(OH)_2D_3$. fSIEC monolayers formed tight junctions, possessing a comparable TEER to that seen in the human small intestine. This makes them an attractive candidate for studies of intestinal permeability. However, the low activity of CYP3A4 makes monolayers of these cells poorly suited for the complex assessment of first-pass intestinal metabolism and permeability.

With the rising interest in developing 3-dimensional microphysiological cell culture systems, there is the hope that a more faithful recapitulation of the native *in vivo* environment will help retain the necessary phenotype for the *in vitro* assessment of the role of enterocytes in the first-pass metabolism and absorption of xenobiotics. Our preliminary findings suggests that fSIECs, when cultured in the more organotypic environment of the MPS, exhibit proper cell polarization and assemble into complex multicellular structures with a striking resemblance to the villi of the small intestine. Further characterization of these multicellular structures is

required to confirm whether they retain an *in vivo*-like pattern in the expression and functionality of CYP3A4 along the crypt-villus axis.

If established, such a system could be linked with the renal proximal tubule microphysiological system (PT-MPS) described in Chapters 4 and 5. An integrated multi-organ system, incorporating both small intestinal and renal proximal tubular modules, would constitute a suitable platform for exploring the crosstalk between the two organs. With the help of collaborators at Johns Hopkins University, we have already successfully linked the PT-MPS with a static 2-dimensional intestinal model to study the absorption and unidirectional sequential inter-organ disposition of vitamin D and its metabolites.[107] Because the renal proximal tubule is the principal site for the formation of $1\alpha,25(OH)_2D_3$, an endogenous regulator of intestinal P-gp and CYP3A4 expression,[88] a move to bidirectional coupling of the PT-MPS with the SI-MPS or other *in vitro* intestinal model could provide mechanistic insights into relationship between vitamin D status, intestinal first pass metabolism and absorption of xenobiotics.

4 Development of a Microphysiological Model of the Human Renal Proximal Tubule

Portions of this chapter were published in Kidney Int. 2016 Sep;90(3):627-37.
Co-first-authorship was shared with Alenka Chapron and Elijah Weber.

4.1 Abstract

The development of a 3-dimensional microphysiological system (MPS), incorporating human proximal tubule epithelial cells (PTECs), represents a major step towards a more faithful *in vitro* recapitulation of the *in vivo* renal tubular environment. Such a model would enable investigators to explore the complex mechanisms underpinning alterations in renal function that accompany disease and xenobiotic exposure. With this goal in mind, PTECs were isolated from human renal cortex and cultured in the Nortis MPS platform under conditions of fluid sheer stress. Polarization of PTECs in the MPS was demonstrated by the enrichment of apical proteins along the luminal interface and localization of Na^+/K^+ ATPase along the basolateral cell surfaces abutting the extracellular matrix. Electron micrographs further revealed the presence of hallmark structural features of PTECs *in vivo*. In addition, PTECs cultured in the MPS system exhibited glucose reabsorption, glutathione reclamation, and ammoniagenesis, key physiologic functions of the renal tubular epithelium.

The renal proximal tubular epithelium is also the major site for conversion of $25OHD_3$ to bioactive $1\alpha,25(OH)_2D_3$ and inactive $24,25(OH)_2D_3$. The $1\alpha,25(OH)_2D_3$ produced in PTECs exerts Vitamin D Receptor (VDR)-dependent intracrine and endocrine effects that are important in regulating systemic mineral homeostasis. To demonstrate vitamin D functionality, the cells were cultured with $25OHD_3$, which resulted in the formation of quantifiable levels of $1\alpha,25(OH)_2D_3$ and $24,25(OH)_2D_3$. When challenged with exogenous $1\alpha,25(OH)_2D_3$, there was a rapid increase in the VDR target gene, CYP24A1. This was accompanied by an increase in the CYP24A1 enzymatic activity.

4.2 Introduction to Chapter 4

The renal proximal tubule is important to many physiological processes. However, *in vivo* evaluations of the mechanisms underpinning these complex physiological processes would require a feasible and ethical means of directly delivering to and sampling from proximal tubules. Micropuncture studies and *ex vivo* animal kidney perfusions in have long served as surrogates for human studies.[108, 109] However, non-human animal physiology can vary substantially from that of humans and replacement of the models is critical to achieve a more accurate understanding of human proximal tubule function.

Advancements in primary human cell isolation and culture techniques have provided the necessary resident cell types (e.g. PTECs, pericytes, microvascual endothelial cells) for the bottom-up *ex vivo* reconstruction of the renal proximal tubule.[37] Recent improvements in nanofabrication and technology provide a means to culture these cells free from artificial materials and at a proximity and 3-dimensional orientation that mimics the anatomy and physiology of the proximal tubular microenvironment.[37] Observations of the positive effects of physiologically relevant fluid sheer stress on promoting a more *in vivo*-like cell phenotype have provided another critical piece in our understanding of how to recapitulate organ functions *ex vivo*.[110, 111]

Using these advancements in primary cell culture, nanofabrication and microfluidics, we have recapitulated the human proximal tubular epithelium. Many of the physiological functions of the renal proximal tubule take place in the epithelium, and recapitulating this component of the proximal tubule represents a major step towards the full integration of all the resident cell types of the proximal tubular microenvironment

This chapter describes the development of a 3-dimensional proximal tubular microphysiological system (PT-MPS). The PT-MPS exhibits long-term cell viability, retains polarized expression and function of proteins essential for reabsorptive transport, responds to physiological stimuli, and performs critical biochemical synthetic activities.

4.3 Materials and Methods

4.3.1 Chemicals and Reagents

Bovine serum albumin, acivicin, hydrocortisone, and Triton X-100 were purchased from Sigma-Aldrich (St. Louis, MO). Buffered formalin acetate was purchased from Fisher Scientific (Pittsburgh, PA). Dapagliflozin and vitamin D metabolites were obtained from Toronto Research Chemicals (Toronto, Ontario). Dulbecco's phosphate-buffered saline with (DPBS) and without ($DPBS^{++}$) calcium and magnesium, 50:50 Dulbecco's modified eagle medium with Ham's F-12 (DMEM/F12), penicillin-streptomycin-amphotericin B, insulin-transferrin-selenium A solution (ITS-A), TRIzol reagent, High Capacity cDNA Reverse Transcription Kit with RNase Inhibitor, TaqMan gene expression assays, fetal bovine serum, and Trypsin EDTA were purchased from Life-Technologies (Carlsbad, CA). Microfluidic platforms were obtained from Nortis (Woodinville, WA). Non-pepsinized rat tail collagen I was purchased from Ibidi (Martinsried, Germany). The colorimetric ammonia assay kit was purchased from Abcam (Cambridge, UK). Mouse collagen IV and tissue culture-treated flasks were obtained from Corning (Corning, NY). 2-(N-(7-nitrobenz-2-oxa-1,3-diazol-4-yl)Amino)-2-deoxyglucose (2-NBDG) was acquired from Cayman Chemicals (Ann Arbor, MI). LIVE/DEAD Viability/Cytotoxicity assay and SlowFade Gold antifade reagent with 4',6-diamidino-2-phenylindole (DAPI) was purchased from Invitrogen (Carlsbad, CA). Primary antibodies against human CD13, E-Cadherin, aquaporin 1,

aquaporin 2, sodium glucose co-transporter-2, γ-glutamyl transferase, acetylated tubulin and fluorescently tagged secondary antibodies were all purchased from Abcam (Cambridge, UK). Primary antibodies against zonula occludens-1 (ZO-1) were purchased from Invitrogen (Carlsbad, CA). Primary antibodies against CYP24A1 and CYP27B1 were obtained from Santa Cruz Biotechnology (Dallas, TX). Na^+/K^+ ATPase was obtained from Fisher Scientific (Pittsburgh, PA).

4.3.2 Human PTEC Isolation and Propagation

Human kidney cortical tissue was obtained from healthy surgical resections of renal cell carcinomas performed at the University of Washington Medical Center. The human subject protocol was approved by the University of Washington Institutional Review Board (protocol # STUDY00001297). Healthy portions of the surgical specimen were dissected, stored at 4°C in Hanks balanced salt solution (HBSS) buffer containing penicillin-streptomycin until the time of processing (within 24 hours).

In order to isolate human proximal tubule epithelial cells (PTECs), the renal cortical tissue was diced by hand with steel razors in a cell culture hood under sterile conditions. The resultant tissue slurry was then incubated under agitation (250 rpm) for 30 minutes at 37°C in a filter-sterilized 1 mg/mL solution of collagenase type IV in HBSS buffer. The collagenase was quenched by the addition of horse serum and remaining undisintegrated tissue was allowed to settle in conical tubes for 2 minutes. The free cell-containing supernatant was transferred to new conical tubes and washed with 37°C PTEC culture media (DMEM/F12 media supplemented with insulin, transferrin, selenium, penicillin, streptomycin, amphotericin B and 50 nM hydrocortisone). The cell suspension was then centrifuged at 200 g for 5 minutes and the

supernatant was aspirated. The cell pellet was then resuspended in PTEC culture media and transferred to tissue culture flasks. Cell culture media was replaced after 24 hours and then every 3 days thereafter until the flasks are populated with cells to 70-100% confluence. Cells were expanded and subcultured on collagen IV-coated tissue culture treated flasks. Cell detachment was performed using 0.05% trypsin with ethylenediamine tetraacetic acid and DMEM/F12 media containing 10% FBS was used for enzymatic quenching. Consistency of gross cellular morphology across donors and passage numbers is shown in Figure 4.1. Cells at passages 1 through 4 were used in the subsequent experiments.

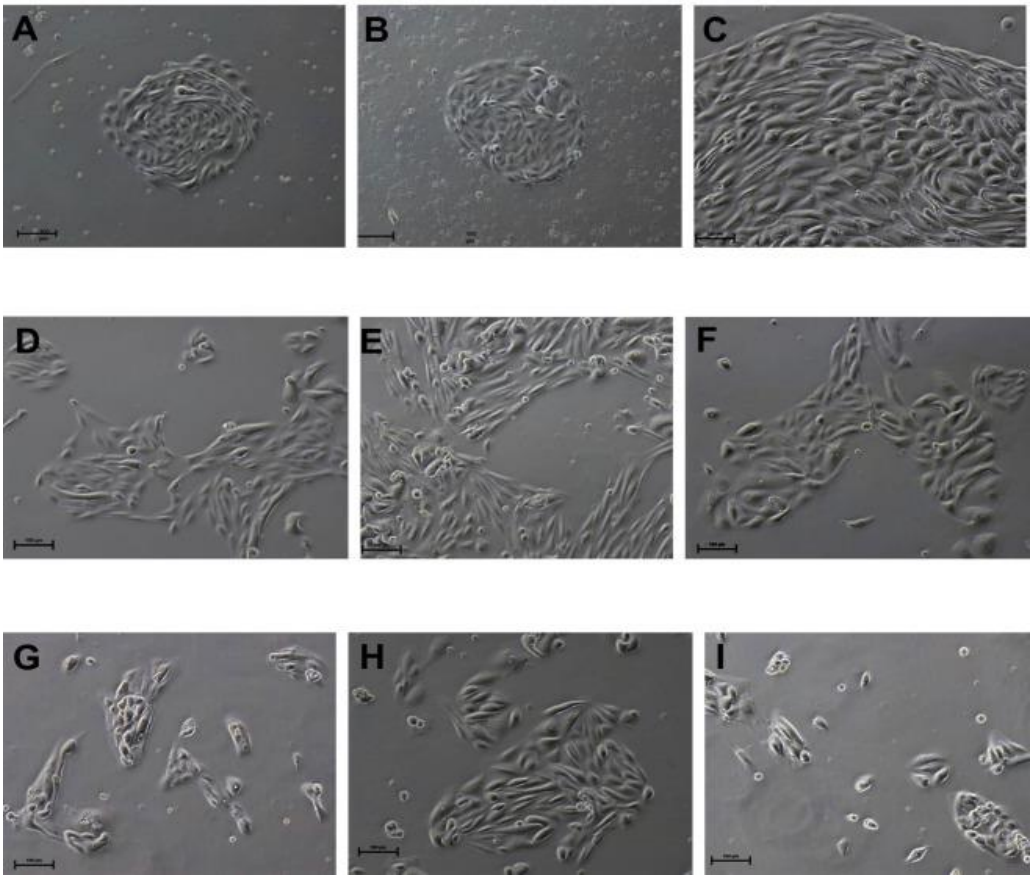

Figure 4.1. Cell morphology across donors and passages. (**A**) Passage 0 cells after 8 days in culture from 68-year-old woman; (**B**) passage 0 cells after 8 days in culture from 60-year-old man; (**C**) passage 0 cells after 25 days in culture from 66-year-old man; (**D, E**) passage 1 cells after 7 days in culture from 63-year-old man; (**F**) passage 1 cells after 5 days in culture from 70-year-old man; (**G**) passage 2 cells after 8 days in culture from 59-year-old man; (**H**) passage 3 cells after 6 days in culture from 71-year-old man; (**I**) passage 3 cells after 15 days in culture from 81-year-old man. Bars = 100 μm.

4.3.3 Cell Seeding and Culture in the PT-MPS

The 3-dimensional microfluidic cell culture platform used in these studies was developed by Nortis Inc. In brief, the unmodified platform is constructed of gas-permeable polydimethylsiloxane (PDMS) housed in a polycarbonate base with an embedded microscope coverslip to facilitate cell imaging. Channels through the PDMS provide access to a chamber that can be filled with an extracellular matrix provided it has sufficient polymerization properties. A microfiber mandrel that crosses this extracellular matrix compartment (120 μm x 6 mm) can be removed following matrix polymerization to provide a hollow lumen through the matrix. This lumen can be coated with additional extracellular matrices. Using access ports through channels in the PDMS, a constant infusion of cell culture medium can be supplied via syringe pumps or Nortis' proprietary system that uses pressurized gas. The constant media perfusion helps to achieve *in vivo*-like conditions within the MPS by constantly supplying adequate oxygen and nutrition to the PTECs and providing an environment of *in vivo*-like fluid sheer stress. Fluid sheer stress has been shown to promote polarization of renal epithelial cells,[111] a property critical to achieving vectorial transport, and subsequently estimating the analogous processes *in vivo*.

For the experiments outlined in this chapter, all microfluidic platforms were filled with 6 mg/mL rat tail collagen type I on ice. Microfluidic platforms were then left for 30 minutes at 4°C, and then collagen I was allowed to polymerize at room temperature overnight. On the day of cell seeding, the microfiber mandrel was removed from each device, leaving behind a hollow channel traversing the collagen I matrix. This channel was coated with 5 μg/mL mouse collagen type IV for 45 minutes prior to cell seeding.

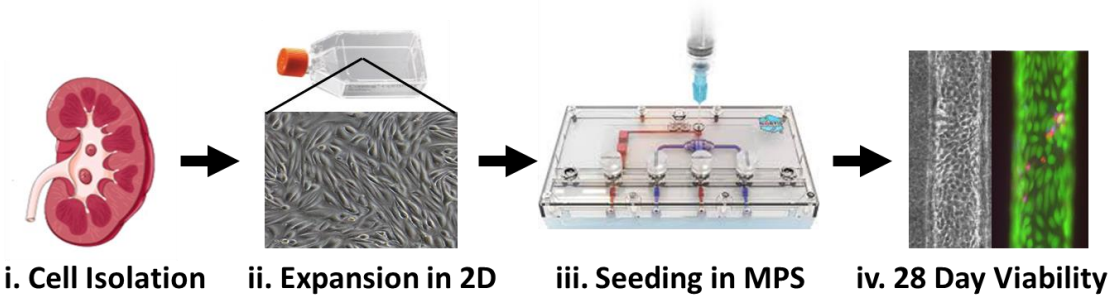

Figure 4.2. Scheme depicting construction of human proximal tubule microphysiological system. (i) Cell isolation from human kidney cortex. (ii) Cell culture in conventional culture flasks. (iii) Cell seeding and culture in 3-dimensional proximal tubule microphysiological system. (iv) Phase contrast and viability of PTECs in MPS at day 28. Cell viability was determined using a LIVE/DEAD viability assay according to the manufacturer-supplied protocol.

In order to constitute a PT-MPS, 2-dimensional monolayers of PTECs (passages 1 to 4) were detached from the cell culture flasks (used for cell expansion) by treatment with 0.05% Trypsin-ethylenediamine tetraacetic acid to obtain single-cell suspensions. The cells were washed with DMEM/F12 containing 10% FBS and resuspended at an approximate concentration of 15 to 20 × 10^6 cells/mL. Approximately 5 µL of cell suspension was injected into the collagen IV–coated lumen. Cells were allowed to adhere to the collagen matrix before media flow was reinitiated at 0.5 µL/min. Approximately 5000 to 10000 PTECs can be cultured in a single PT-MPS unit. Cell coverage and integrity of the tubule structure were assessed under light microscopy prior to all experiments. For all experiments, microfluidic platforms contained PTECs grown for 2 to 3 weeks after initial cell seeding. A general overview of cell isolation and seeding workflow is depicted in Figure 4.2.

4.3.4 Immunocytochemistry

Proximal tubule epithelial cells in MPS platforms were fixed with 10% Buffered formalin acetate or 4% paraformaldehyde in Dulbecco's phosphate-buffered saline with calcium and magnesium ($DPBS^{++}$) for 1 hour, permeabilized with 0.5% Triton X-100, and blocked with 5% bovine serum albumin (BSA) for 40 minutes. Subsequently, cells were incubated with different dilutions of primary antibodies overnight at 4°C. Primary antibodies included CD13 (mouse, 1:100), E-Cadherin (mouse, 1:100), ZO-1 (rabbit, 1:100,), Aquaporin 1 (rabbit, 1:100), Aquaporin 2 (rabbit, 1:100), uromodulin, prominin-2, Na^+/K^+ ATPase (mouse, 1:100), SGLT2 (rabbit, 1:100), GGT (mouse, 1:100), acetylated tubulin (mouse, 1:100), CYP24A1 (mouse, 1:100), and CYP27B1 (rabbit, 1:100). After washing, fluorescently labeled secondary antibodies were added for 1 hour at room temperature. Donkey anti-rabbit IgG (1:1000) or donkey anti-mouse IgG (1:1000) were used as secondary antibodies. Cells were mounted using SlowFade Gold antifade reagent with DAPI to visualize cell nuclei.

Phase contrast and fluorescent images were taken with a Nikon Eclipse T*i*-S and inverted spinning disk microscope (3i-Intelligent Imaging Innovations, Denver, CO). Acquired images were processed either in ImageJ 1.48v (National Institutes of Health) or Slidebook software (Intelligent Imaging Innovations). Confocal images were captured on a Carl Zeiss LSM 780 confocal microscope (Carl Zeiss Microscopy, Jena, Germany) using a Zeiss C-Apochromat 40x/1.1 water immersion objective. *Z*-sections were taken at 2 µm intervals through the depth of the tubule, typically a distance of 120 µm. Acquired confocal images were processed in Volocity 6.3 3D Image analysis software (Perkin Elmer, Waltham, MA).

4.3.5 Transmission Electron Microscopy

In order to elucidate the ultrastructure of PTECs cultured in the MPS, transmission electron microscopy was employed. PT-MPS units were fixed in 1/2× Karnovsky fixative (2.5% glutaraldehyde with 2% formaldehyde in 0.1 M buffer). Samples were postfixed in osmium tetroxide and processed, sectioned, and examined according to protocols described previously.[112]

4.3.6 γ-Glutamyl Transferase Activity

The presence and functioning of γ-glutamyl transferase (GGT) was demonstrated by metabolism of glutathione disulfide (GSSG) in PT-MPS units cultured to >50% cell confluence. To test for GGT activity, PT-MPS units were perfused at 1 μL/min with the previously described standard PTEC culture media with 4 μM of GSSG added. Efflux media samples were collected at hourly intervals for a total of 4 hours. After the first phase of collection, the PT-MPS units were perfused overnight using fresh media to ensure sufficient washout of GSSG. To verify specificity of GSSG processing by GGT, PT-MPS units were reperfused with 4 μM GSSG in the presence of GGT inhibitor–acivicin (1 μM), and effluent media samples were collected hourly for a total of 4 hours. GSSG concentration in the effluent perfusate was measured via liquid chromatography–tandem mass spectrometry (LC-MS/MS). Analysis of GSSG was accomplished from direct injection of 2 μL of the perfusate efflux samples, without any sample preparation, onto an Agilent Technologies (Santa Clara, CA) model 1290 HPLC equipped with binary pump, thermostated auto-sampler, and heated column compartment. The autosampler compartment was maintained at 4°C. A 2.1 mm x 150 mm, 5 μm Develosil Rp-Aqueous C30 column (Phenomenex, Torrance, CA) was used and maintained at 35°C. The mobile phase consisted of

0.1% formic acid (A) and methanol (B) at a flow rate of 0.2 mL/min. The following mobile phase gradient was employed: 0% B held 0-3.5 min, 0-20% over 3.5-6 min, 20% held at 6-8.1 min, 20-0% B at 8.1-8.2 min. The HPLC was coupled to an Agilent Technologies (Santa Clara, CA) model G6410B triple quadrupole mass spectrometer. The mass spectrometer was operated in the ESI+ mode with the following operating parameters: GSSG transition — m/z 613.0 □ 231.0, fragmentor — 135 volts, CE — 36 volts, VCAP — 3500 volts, drying gas — 10 L/min nitrogen at 350°C, and nebulizer gas — nitrogen at 35 psi. As the GSSG appeared to be unstable in cell media even at 4°C in the autosampler, a single standard of GSSG spiked into blank media was injected prior to the samples in order to confirm retention time and estimate instrument response of GSSG. Responses were measured in absolute height counts. Results are presented as recovery of GSSG expressed as a percentage of nominal input in the presence and absence of GGT inhibitor. Differences in GSSG recovery were evaluated with t-tests, paired by individual PT-MPS units before an after acivicin co-treatment.

4.3.7 Glucose Reabsorption

In preparation for the assessment of SGLT2-mediated glucose reabsorption, PT-MPS units were perfused with standard PTEC culture media for at least 2 weeks prior to being tested for glucose reabsorption. Glucose uptake was assessed using a fluorescent glucose analog, 2-NBDG. Twelve hours prior to testing, PTEC perfusion was switched to culture media with a lower, physiological, glucose concentration (100 mg/dl). After 12 hours of pretreatment, PT-MPS units were perfused with media containing 200 μg/mL (0.6 mM) of 2-NBDG in the presence or absence of a glucose transporter 1 (GLUT1) inhibitor (50 μM apigenin) or a SGLT2 inhibitor (0.5 μM dapagliflozin) for 2 hours at 37°C. Platforms were then washed and imaged

using a Nikon Eclipse T*i*-S (Tokyo, Japan) and inverted spinning disk microscope in phase contrast and fluorescent modes and fluorescent signal quantified using ImageJ software (National Institutes of Health, Bethesda, MD).

4.3.8 Ammoniagenesis

The ability to secrete ammonia in response to acidification was evaluated in PT-MPS units cultured with PTECs grown to >50% confluency. The PT-MPS units were initially perfused with phosphate-buffered saline (pH 7.4) at a flow rate of 1 μL/min for 4 hours; effluent was collected at 2-hour intervals. After 4 hours, the perfusate was switched to phosphate-buffered saline buffered to a relatively more acidic pH of 6.9, and 2-hourly collection of effluent was continued for another 4 hours. Samples at hour 4 were analyzed for ammonia concentration using a using a commercially available colorimetric ammonia assay kit according to the manufacturer-supplied protocol. Effluent ammonia concentrations at acidic and physiological pH conditions were compared.

4.3.9 25OHD$_3$ Metabolism

Conversion of 25OHD$_3$ to its physiologically active and inactive metabolites was assessed in the PT-MPS. Human PTECs cultured from 3 separate tissue donors were evaluated in triplicate for a total of 9 PT-MPS units. The cells were cultured for 2 to 3 weeks prior to the addition of 1 μM 25OHD$_3$ to the perfusion media. The media was also supplemented with 2% v/v fetal bovine serum (FBS) to minimize non-specific adsorption of vitamin D$_3$ metabolites to the tubing and components of the Nortis microfluidic platforms. The inflow rate of 25OHD$_3$-containing media was set at 0.5 μL/min and outflow was collected daily for 3 days and stored

at −80°C. Concentrations of 25OHD$_3$ and its primary oxidative metabolites were determined from 450 µL aliquots of efflux media samples using a modified LC-MS/MS method previously reported for assay of oxidative vitamin D metabolites in plasma.[113] To improve sensitivity limits, the established method was implemented on a Nexera X2 LC-30AD UHPLC (Shimadzu, Kyoto, Japan) coupled to an AB/SCIEX QTRAP 6500 mass spectrometer (Sciex, Framingham, MA). The following modifications were made to the published method: [1] methanol (MeOH) replaced acetonitrile as the organic mobile phase; [2] the mobile phase gradient was changed to 0-1 min at 35% MeOH, 6-8 min at 65% MeOH, 15-15.5 min at 75% MeOH, 17-19 min at 90% MeOH, 19.2-22.1 min at 35%; and [3] total flow was increased to 0.25 mL/min; [4] injection volume was reduced to 2 µL; [5] column temperature was increased to 45°C; [6] gas temperature was increased to 400°C; and [7] capillary voltage, fragmentor voltage, and collision energy were changed to 5500 V, 70 V and 20 V respectively. Data was acquired and peaks were integrated using Sciex Analyst version 1.6 software.

Formation clearance for three dihydroxy-vitamin D$_3$ metabolites (1α,25(OH)$_2$D$_3$, 4β,25(OH)$_2$D$_3$ and 24,25(OH)$_2$D$_3$) were plotted as formation clearance (CL_f) over time with GraphPad (La Jolla, CA) Prism v. 5.1 using the following equation:

$$CL_f = \frac{\frac{dA_m}{dt} + (CL_m \times C_m)}{C_p}$$

Concentration of the respective dihydroxy-vitamin D$_3$ metabolites was represented by the parameter C_m and the concentration of the parent 25OHD$_3$ was represented by C_p. Rate of metabolite formation (dA_m/dt) was determined by dividing the observed mass of the formed

metabolite by the duration of the 24-hour collection interval. We assumed no sequential metabolism for any of the dihydroxy-vitamin D_3 metabolites during the course of the experiment; clearance of the metabolite (CL_m) was assumed to be negligible and set equal to zero. The formation clearance was then plotted at the midpoint of the collection interval.

4.3.10 VDR-Dependent Regulation of CYP24A1 Activity

To evaluate the inductive effects of $1\alpha,25(OH)_2D_3$ (calcitriol) on the 24-hydroxylation of $25OHD_3$ (calcidiol), a group of PT-MPS units ($n = 5$) were exposed to 1 μM calcidiol in the presence or absence of 0.5 μM exogenous calcitriol. Effluent was collected for 3 days and stored at −80°C until LC-MS/MS analysis of $24,25(OH)_2D_3$ and calcidiol concentrations. Following treatment, RNA was extracted using Tri-reagent according to the manufacture-supplied protocol. In order to assess the more rapid effects of calcitriol coadministration on gene expression, additional MPSs were treated for 5 hours prior to collection in Tri-reagent. RNA was quantified on a NanoDrop ND-2000 spectrophotometer from Thermo-Fisher (Waltham, MA) and reverse transcribed to cDNA using reverse transcription kit. Isolated RNA was mixed with other components (including RNase inhibitor) of the high-capacity cDNA reverse transcription kit according to the manufacturer-supplied protocol. Reverse transcription was conducted in a PTC-200 thermal cycler (Bio-Rad, Hercules, CA) under the following conditions: 10 minutes at 25°C, 120 minutes at 37°C and 5 seconds at 85°C. Quantitative real-time polymerase chain reactions were then performed under the following conditions: warm up at 50°C for 10:00, followed by 40 cycles of 95°C for 5:10 and 60°C for 0:30. The effect of calcitriol on the expression of genes relevant to calcidiol metabolism (*CYP24A1*, *CYP27B1*, and *VDR*) was assessed using TaqMan Gene expression assays on a CFX Connect Real-Time PCR Detection System (Bio-Rad

Laboratories, Hercules, CA). Relative quantification of mRNA was determined using the ΔΔCt method with glyceraldehyde-3-phosphate dehydrogenase (GAPDH) serving as a housekeeping gene.

4.4 Results

4.4.1 Confirmation of PTEC Markers

Cell surfaces showed fairly even expression of CD13 (aminopeptidase-N) and E-cadherin, markers of epithelial origin, for at least 28 days (Figure 4.3). Proximal tubule origin of the final culture was verified by consistent ICC staining for aquaporin-1 (Figure 4.3) and lotus lectin, whereas the signal for aquaporin-2, prominin 2, and uromodulin, markers of distal tubule or collecting duct cells or both, was absent in cells cultured both 2-dimensional and MPS units (data not shown).

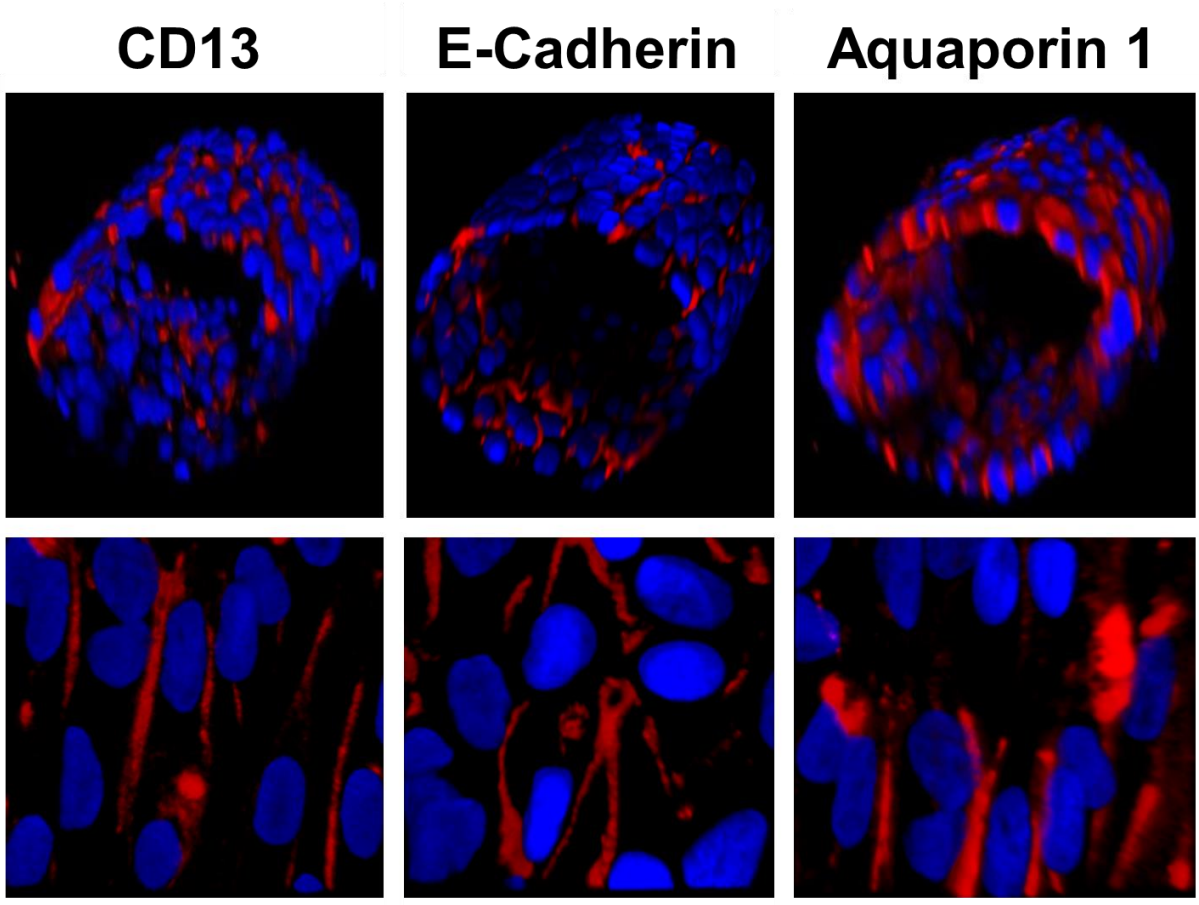

Figure 4.3. Markers of proximal tubular and epithelial phenotype. Depicted in red from left to right; surface expression of epithelial cell marker CD13 (aminopeptidase-N); cell self-assembly confirmed by E-cadherin expression; proximal tubule origin confirmed by expression of aquaporin 1 (original magnification ×400).

4.4.2 Polarization of PTECs in the PT-MPS

Polarization of PTECs was shown by localization of the tight junction protein ZO-1 to the luminal (apical) aspect of the PTEC tubule and localization of Na^+/K^+–adenosine triphosphatase (Na^+/K^+ ATPase) to the lateral interface between neighboring cells and the basal border between PTECs and collagen substrate (Figure 4.4).

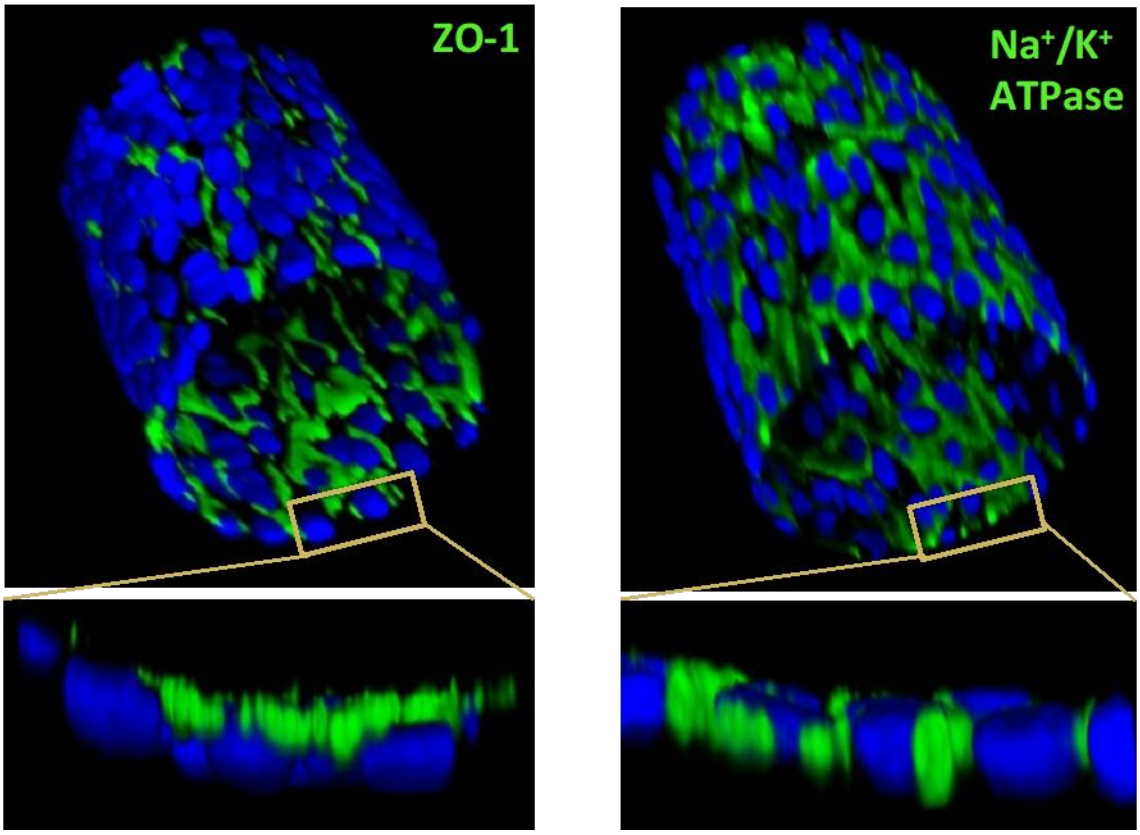

Figure 4.4. Polarization of human PTECs in PT-MPS. Cellular polarization of PTECs was confirmed by tight junction formation via apical localization of ZO-1 (green in left side image) and basolateral expression of Na^+/K^+ ATPase (green in right side image). Tubule diameter is ~120 μm for reference.

4.4.3 PTEC Ultratructure in the PT-MPS

Transmission electron microscopy images of PTEC ultrastructure showed representative density of mitochondria, golgi apparatus, and rough endoplasmic reticulum. Tight junctions and short microvilli at the apical surface were also observed, as well as basolateral interdigitations

between neighboring cells, the latter being characteristic of proximal tubules *in vivo* (Figure 4.5). Furthermore, fluid sheer stress-induced cilia formation was evidenced by positive staining of acetylated tubulin in rod-like structures that originate from close to the cell nucleus. The ciliary processes averaged 10 ± 3.5 μm in length (Figure 4.5B1 and B2).

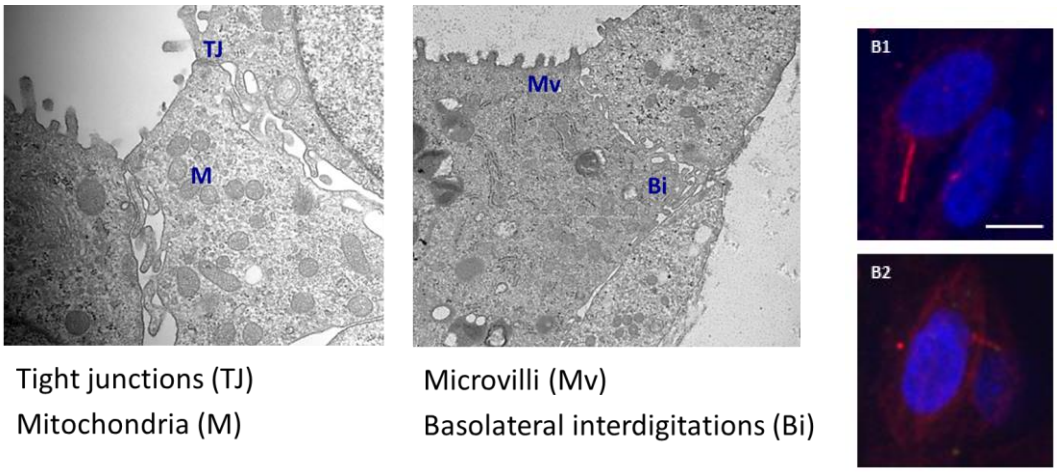

Figure 4.5. Ultrastructure of human PTECs in PT-MPS. Transmission electron microscopy of ultrastructure of proximal tubular epithelial cells (PTECs) cultured in a microphysiological system (MPS). The following cellular structures are identified: microvilli (MV), mitochondria (M), tight junction (TJ), and basolateral interdigitations (Bi). PTECs in MPS form cilia as seen from 2 representative images (B1 and 2) of single cells stained for acetylated tubulin in red. Bars = 5 μm).

4.4.4 γ-Glutamyl Transferase Activity

Reclamation of glutathione is an essential biochemical function of renal proximal tubule *in vivo*.[114] The reclamation process is mediated by γ-glutamyl transpeptidase (GGT), which normally catalyzes the transfer of glutamyl moiety from glutathione to an acceptor amino acid as part of the γ-glutamyl cycle, a pathway for the synthesis and degradation of glutathione. Selective ICC staining for GGT in the PT-MPS revealed enriched localization of the enzyme at the luminal aspect of the PTEC structure (Figure 4.6A). GGT mediates a comparable reaction for the oxidized form of glutathione, glutathione disulfide (GSSG),[115] which is a more chemically

stable substrate for assessing the activity of γ-glutamyl transpeptidase in the PT-MPS. PTECs within the MPS were perfused with media containing 4 μM GSSG in the presence or absence of an irreversible GGT inhibitor, 1 mM acivicin. The recovery of GSSG in the effluent was low (<1.5%), demonstrating extensive catalytic activity of GGT; in the presence of acivicin, an approximate 2-fold increase in GSSG recovery was observed over 2 to 4 hours (Figure 4.6B).

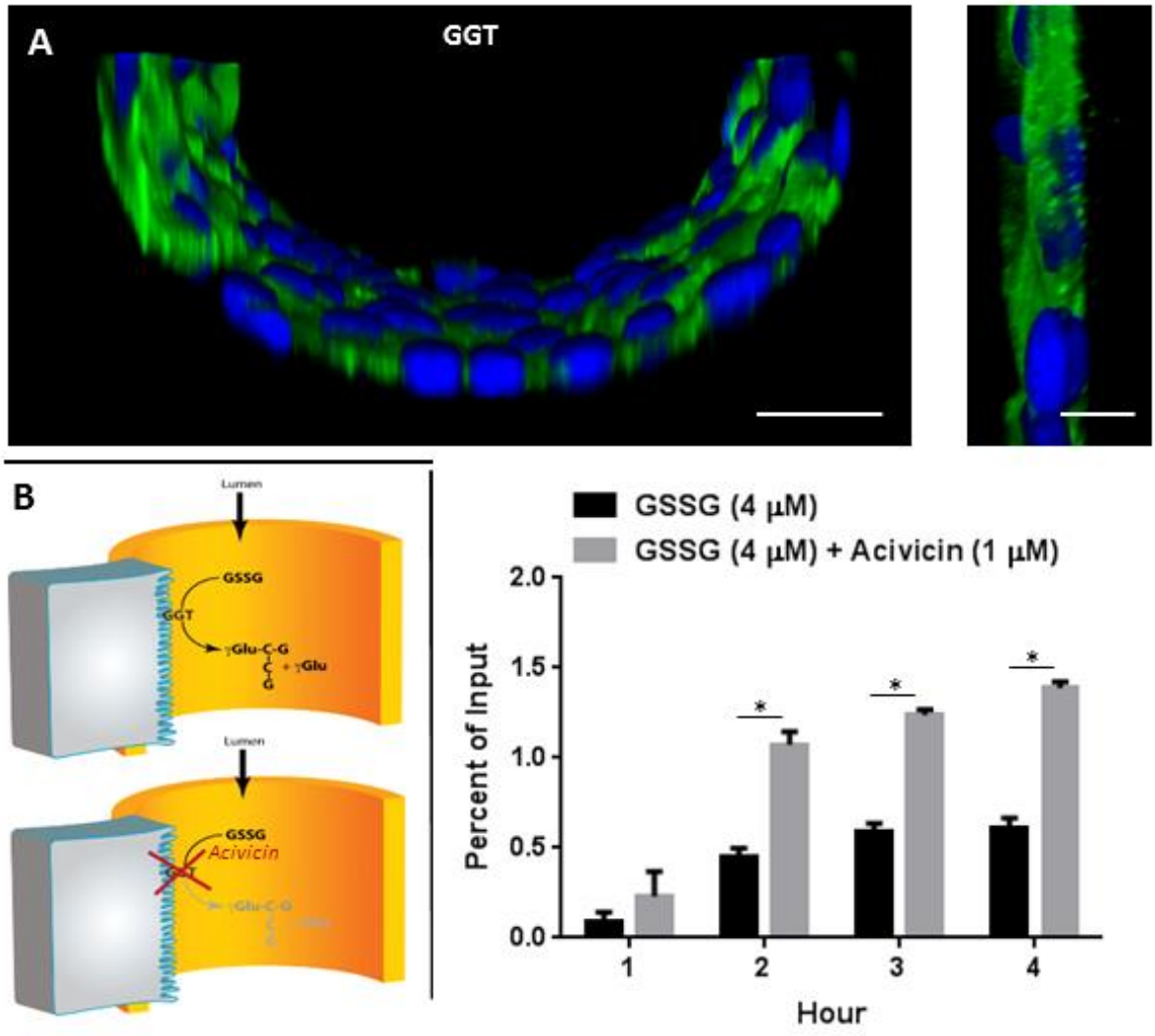

Figure 4.6. GGT activity in the PT-MPS. (**a**) ICC staining reveals proper apical localization of GGT (green) in juxtaposition to nuclei (blue) within the PTEC tubule. (**b**) GGT is functionally essential to cleaving the γ-glutamyl moiety from oxidized glutathione and can be inhibited by acivicin. (**c**) GGT activity as determined by oxidized glutathione abundance in the presence and absence of inhibitor, acivicin (n = 4 microphysiological system [MPS] devices) *P < 0.001, 2-tailed t-test. Bars = 20 μm for the tubule and 10 μm for the wall.

4.4.5 Glucose Reabsorption

The proximal tubule is responsible for nearly 90% of glucose reabsorption in the kidney, which is mediated primarily by glucose transporters, including sodium glucose co-transporter-2 (SGLT2).[15] Selective ICC staining for SGLT2 in the PTECs revealed its expression and localization at the apical surface (Figure 4.7A). To confirm functioning of SGLT2 in the PT-MPS, glucose reabsorption was demonstrated by perfusing the PT-MPS with a fluorescent glucose analog, 2-NBDG, in the presence or absence of either the GLUT1 inhibitor (apigenin) or a SGLT2-specific inhibitor (dapagliflozin).[116] The PTEC layer showed strong green fluorescent signal, demonstrating avid cellular uptake and accumulation of 2-NBDG.

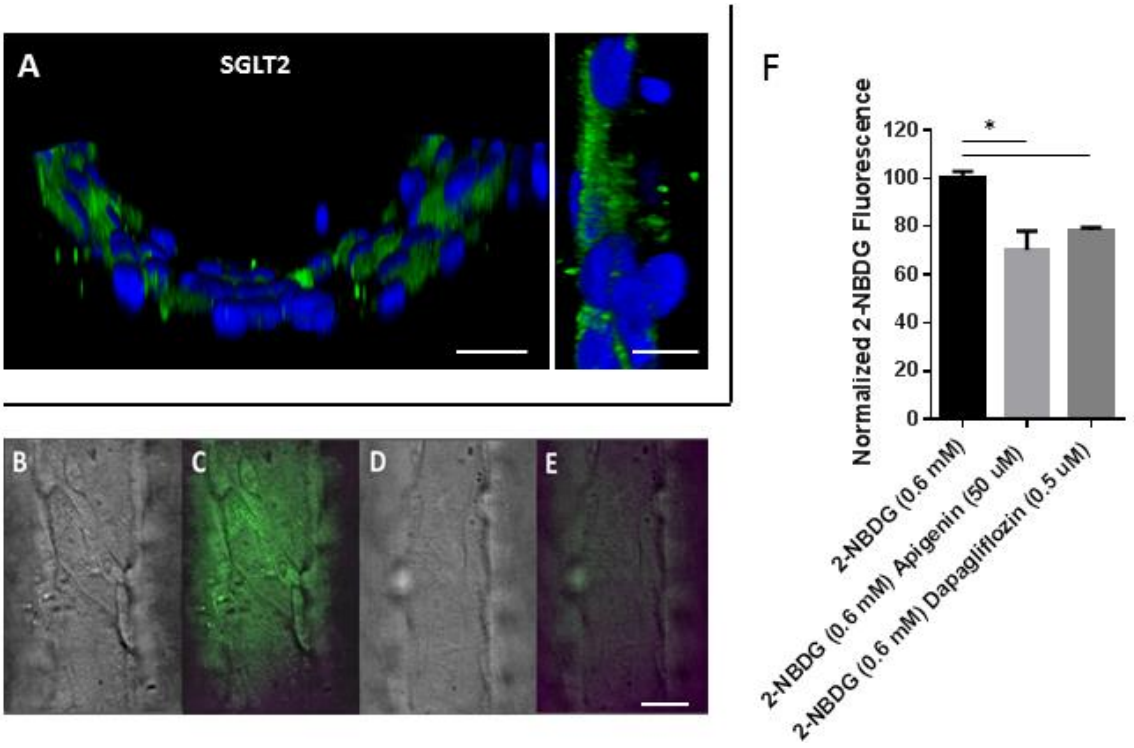

Figure 4.7. Glucose reabsorption in PT-MPS. (**a**) Immunocytochemistry reveals proper apical membrane enrichment of SGLT2 (green) in juxtaposition to nuclei (blue). (**b,d**) Differential interference contrast images showing the structure of PTECs in the MPS in the presence and absence of apigenin (GLUT1 inhibitor) and dapagliflozin (SGLT2 inhibitor). (**c,e**) Fluorescent images showing the distribution of the fluorescent glucose analog, 2-NBDG. (**c**) 2-NBDG was actively reabsorbed in the absence of inhibitor and (**e**) was not absorbed in the presence of inhibitor. (**f**) Quantification of a cell-associated fluorescent signal following subtraction of autofluorescence, demonstrating significant reduction of glucose uptake in the presence of inhibitors apigenin and dapagliflozin (n = 3 MPS devices/group) *P < 0.001, unpaired t-test. Scale Bars = (**a**) 20 μm for the tubule and 10 μm for the wall; (**e**) 50 μm.

Fluorescent signal intensity of 2-NBDG decreased significantly in the presence of both inhibitors, indicating blockade in uptake of the fluorescent glucose analog into epithelial cells (Figure 4.7B to F). It is worth noting that the magnitude of effect for both inhibitors (25%–30%) is similar to the clinical efficacy of SGLT2 inhibitors (30%–50%) despite *in vitro* predictions of 90% inhibition.[16]

4.4.6 Ammoniagenesis

Renal proximal tubules respond *in vivo* to a drop in either blood or luminal filtrate pH with an increased generation and secretion of ammonia (Figure 4.8A). To demonstrate this physiological response, PT-MPS units were exposed to a decrease in luminal perfusate pH from 7.4 to 6.9. PTECs in the MPS responded with an approximate 3-fold increase in effluent ammonia concentration (pH 7.4–0.55 mM NH_3, pH 6.9–1.56 mM NH_3) (Figure 4.8B).

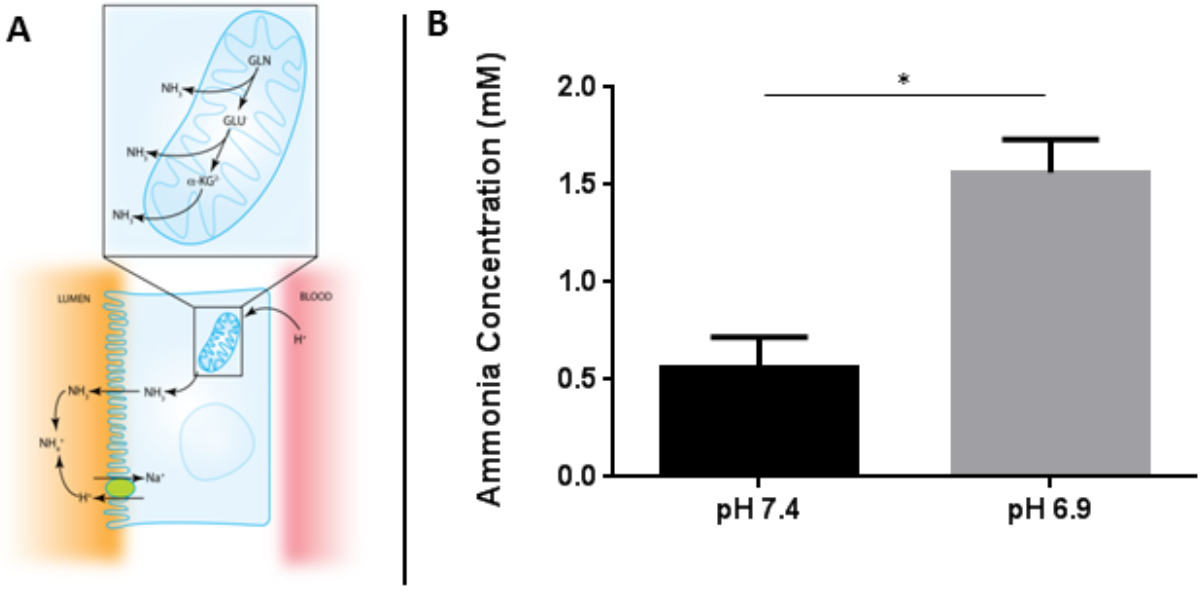

Figure 4.8. Ammoniagenesis in human kidney 3D MPS. (**a**) The physiological response to a drop in either blood or luminal pH resulting in the generation and secretion of ammonia in the tubular outflow. (**b**) With the PT-MPS, luminal media was initially at pH 7.4 and then switched to pH 6.9. Secreted ammonia in the outflow was quantified from 4 separate units after 4 hours and was significantly different when exposed to acidic conditions. **P* = 0.05, 2-tailed *t*-test. α-KG^2, alpha ketoglutarate; GLN, glutamine; GLU, glutamic acid.

4.4.7 25OHD$_3$ Metabolism

The proximal tubule epithelium is known to be a critical site for bioactivation of vitamin D. Systemically available 25-OH vitamin D_3 (calcidiol) is converted to bioactive 1α,25$(OH)_2D_3$ (calcitriol) through the action of cytochrome P450 27B1 (CYP27B1). Metabolism of calcidiol to relatively inactive metabolites also occurs in the kidney via cytochrome P450 24A1 (CYP24A1). ICC staining of PTECs cultured in the MPS revealed the presence of both CYP27B1 and CYP24A1 along the length of the epithelial cell tubule (Figure 4.9).

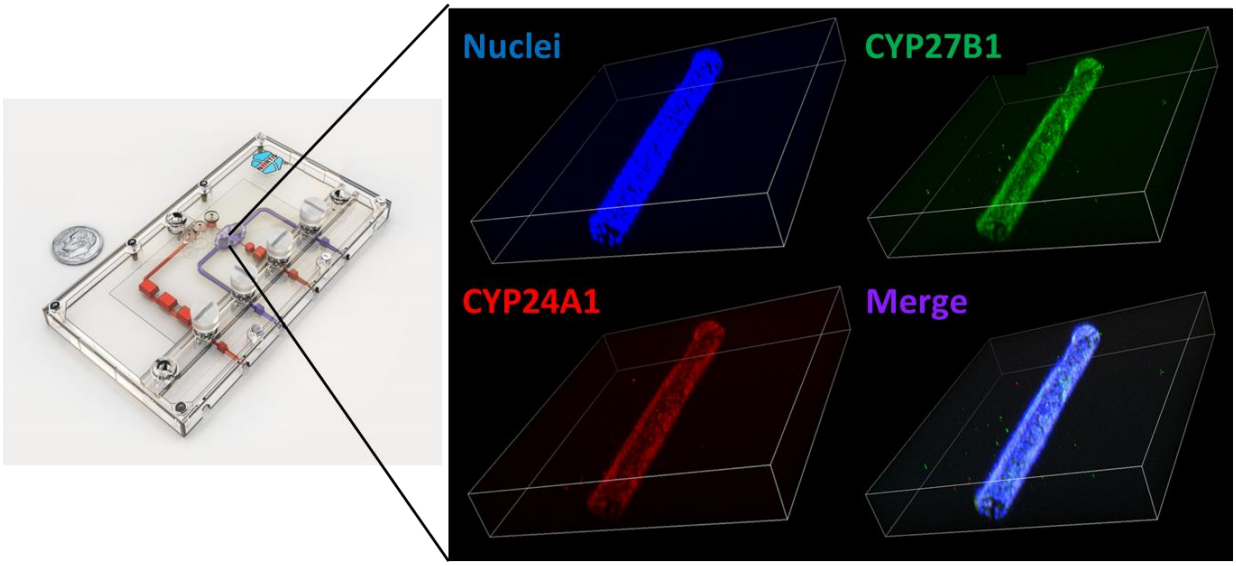

Figure 4.9. Expression of vitamin D metabolizing P450s in PT-MPS. ICC staining revealed expression of both CYP24A1 (red) and CYP27B1 (green) along the length of the PT-MPS cell tubule. Nuclei of the PTECs is depicted in blue.

Furthermore, PT-MPS units demonstrated the ability to metabolize calcidiol to quantifiable levels of bioactive calcitriol, inactive 24,25$(OH)_2D_3$ and 4β,25$(OH)_2D_3$ (Figure 4.10A). Overall, the formation clearance (i.e., formation rate normalized by substrate concentration) for 24,25$(OH)_2D_3$ was significantly greater than that of calcitriol and 4β,25$(OH)_2D_3$. This finding is consistent with metabolism of calcidiol *in vivo*, where circulating

concentrations of 24,25$(OH)_2D_3$ are known to be higher than those of both calcitriol and 4β,25$(OH)_2$ D_3.[113]

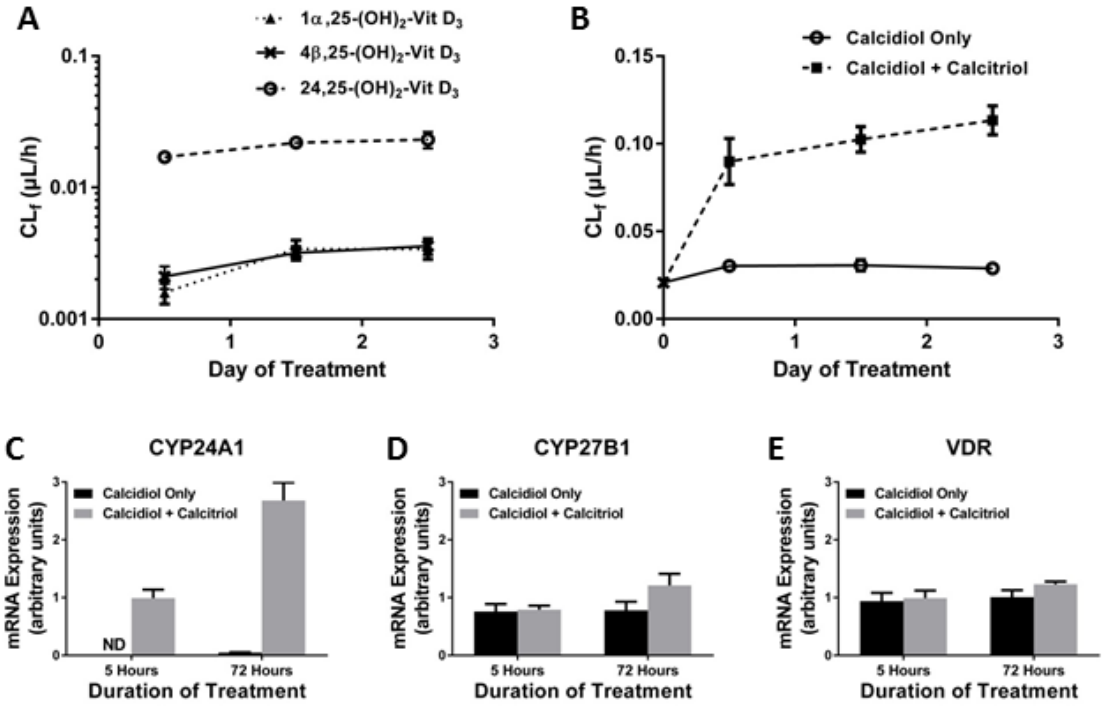

Figure 4.10. VDR-mediated regulation of vitamin D metabolism in human kidney PT-MPS. (**a**) Formation clearance of the 1α,25$(OH)_2D_3$ (calcitriol), 4β,25$(OH)_2D_3$, and 24,25$(OH)_2D_3$ over 3 days exposure of PT-MPS units to 1 μM 25-OH-Vit D_3 (calcidiol). Clearance values are plotted at midpoint of collection interval. Sequential metabolism was assumed to be negligible. (**b**) Formation clearance of the 24,25$(OH)_2D_3$ was greater in PT-MPS cultured in media with both 0.5 μM calcitriol and 1 μM calcidiol than those exposed to 1 μM calcidiol alone. Clearance values were plotted at the midpoint of the collection interval. Sequential metabolism was assumed to be negligible. Baseline data point (×) for formation clearance (CL_f) was determined from the experiment presented in (**a**). Effect of calcitriol on gene expression of (**c**) *CYP24A1*, (**d**) *CYP27B1*, and (**e**) *VDR* in MPS-seeded PTECs. Relative accumulation of *CYP24A1* mRNA transcripts was greater in MPS-seeded PTECs cultured in media with both calcitriol and calcidiol than those exposed to calcidiol alone. Induction of *CYP24A1* mRNA occurred rapidly (5 hours) and persisted for the duration of treatment (3 days). No detectable (ND) transcripts of CYP24A1 were observed in the 5-hour calcidiol-only group. There were no substantial changes in *CYP27B1* and *VDR* mRNA expression over the duration of treatment. All genes of interest were standardized to glyceraldehyde-3-phosphate dehydrogenase (GAPDH).

4.4.8 VDR-Dependent Regulation of CYP24A1 Activity

PT-MPS units were challenged with additional exogenous calcitriol (500 nM), a VDR ligand. Induction of the VDR–regulated 24-hydroxylation pathway was observed (Figure 4.10B).

This increase in 24,25$(OH)_2D_3$ formation was accompanied by a rapid (5 hours) and sustained (72 hours) accumulation of mRNA transcripts for *CYP24A1* (Figure 4.10C). No apparent changes in gene expression of *CYP27B1* (Figure 4.10D) or *VDR* (Figure 4.10E) were observed.

4.5 Discussion

We have demonstrated that in a flow-directed MPS, human PTECs attach to supportive collagen extracellular matrix and self-assemble to form a 3-dimensional tubular structure.[37, 117] Furthermore, cells maintain renal epithelial differentiation and characteristic polarized morphology in this microenvironment for an extended period of time. In contrast, PTECs grown in conventional 2-dimensional monolayer cultures often show limited longevity and loss of distinctive epithelial phenotype due to lack of fluidic mechanosensory input and other stimulus elements present in the native microenvironment *in vivo*.[118, 119]

We also demonstrated proximal tubular origin for the majority of epithelial cells in culture by ICC staining of differential markers of kidney epithelial cells (viz., aquaporin 1, aquaporin 2, and SGLT2). Structurally, PTECs in the MPS exhibited polarized structure based on localization of domain-marker proteins. Assessment of ultrastructure by transmission electron microscopy revealed the hallmarks of a competent epithelial barrier, as well as healthy mitochondria and characteristic basolateral membrane interdigitations. The apical brush border expressed functionally active SGLT2 transporter and GGT enzyme. Although brush border microvilli on the cultured PTECs were not as abundant as in freshly isolated cells,[120] this is consistent with literature reports of low microvilli density in traditional PTEC monolayer cultures.[121, 122] Metabolic competence of the cultured human PTECs was confirmed by their capability for ammoniagenesis and vitamin D biotransformation. In the case of vitamin D, this

metabolic competence was accompanied by retention of some of the regulatory machinery critical to maintaining vitamin D homeostasis *in vivo*.

A number of 3-dimensional tissue engineering models have been developed that attempt to mimic the proximal tubule structure and function.[114, 119, 123, 124] A number of these systems utilize a monolayer of cells adhered to a microporous membrane coated with a thin layer of an extracellular matrix protein component, often collagen IV or laminin. The importance of 3-dimensional tubular architecture is reinforced by the observation that transplantation of 2-dimensional sheets of porcine renal proximal tubule cells onto dorsal subcutaneous tissue of nude rats results in increasingly complicated tubular structures with altered expression of surface markers as the 2-dimensional sheets convert to their native structure *in vivo*.[125] It has become increasingly evident that the composition,[126] microtopography,[127, 128] and rigidity/elasticity [129, 130] of the extracellular matrix substrate on which a cell adheres can dictate the cells' morphology, phenotype, proliferation, and even fate.

Unlike systems using microporous membranes, the tubular structures formed in our PT-MPS are surrounded by extracellular matrix whose composition and rigidity/elasticity can be modified to best recapitulate *in vivo*-like cellular function. Additionally, our microfluidic system enables co-culture of a variety of cell types in the matrix compartment and the proximal tubule channel, permitting critical cell-cell and cell-matrix interactions, without interference from artificial scaffold materials.

The system described herein represents a milestone in cell culture modeling of human kidney in that it is possible to achieve a functional 3-dimensional construct of human proximal tubule *in vitro* in a microfluidic device that more faithfully reflects the native microenvironment of the renal tubulo-interstitium. There have been earlier attempts in recapitulating a functioning

3-dimensional proximal tubule. *DesRochers et al.* constructed a static 3-dimensional culture of proximal tubular cells by culturing immortalized human renal cortical epithelial cells (NKi-2) suspended in an extracellular matrix consisting of a 50:50 mixture of rat tail collagen I and Matrigel®.[118] *Maschmeyer et al.* cultured immortalized cell line renal proximal tubular epithelial cell/telomerase reverse transcriptase 1 on a polyester track etched membrane within a 4-organ-chip device under continuous flow.[131] Although longevity in culture and reproducible sourcing are practical advantages, the altered biology of immortalized cell lines is a serious drawback. The observation that the PTECs in our MPS self-assemble into 3-dimensional tubular structure may help to recapitulate proximal tubular functionality more effectively than previous 2-dimensional monolayer or dispersed culture systems have done.

More recently, *Jang et al.* reported development of a "kidney on a chip" with similar goals to our project.[119] The MPS reported by Jang et al. consisted of a PTEC epithelial monolayer exposed to an apical fluid shear stress that was capable of reabsorbing glucose in the range of approximately 2% of the nominal input.[119] Notably, our PT-MPS achieves approximately 10-fold higher glucose reabsorption than that noted by *Jang et al.* and is responsive to SGLT-2 specific inhibition. Thus, it more closely replicates the expected physiological function of efficient apical glucose uptake, a key function of proximal tubules *in vivo*. In addition, were also able to demonstrate physiologically regulated proximal tubular cytochrome P450 function in the biosynthesis of vitamin D sterols. Finally, our system demonstrates maintenance *in vitro* of an epithelial cell phenotype for up to 28 days, whereas the system employed by Jang et al. was tested for only up to 4 days.[119]

In pioneering work by *Humes et al.*,[114] the development of a renal tubule assist device (RAD) also recapitulated multiple aspects of proximal tubular physiological function *ex vivo*.

Similar to what we observe in our MPS, the RAD also demonstrated glucose reabsorption and glutathione metabolism.[114] The RAD, as the name implies, was developed for the purpose of providing proximal tubule replacement therapy in the setting of kidney failure, whereas our PT-MPS was designed for the specific purpose of improving the drug development as part of the National Institutes of Health Organs on Chips Consortium. Thus the RAD was designed to support renal function *in vivo* on a macroscale, whereas our PT-MPS is primarily designed for predictive toxicity testing on a microscale. Given the divergent goals for development of the RAD and our PT-MPS, it is not surprising that each system has both comparative strengths and weaknesses. In the RAD system, media is perfused across a flat cell sheet in a 1 mm wide channel that attempts to mimic luminal shear stress. In contrast, our MPS enables the creation of a 120 μm diameter tubular tissue that is in direct contact with the surrounding 3-dimensional extracellular matrix, which more closely replicates human anatomy. Additionally species specificity for individual transporters may be a concern, given the use of primary porcine cells in the RAD device, although the RAD tested in clinical trials did make use of human cells.[132] Because of the thickness of the hollow fiber dialysis membrane, the RAD may be less efficient for assessing basolateral secretory organic solute clearance, which is the major mechanism for proximal tubule drug and metabolite elimination.

Conversely, because the hollow fiber design of the RAD allows facile abluminal flow and creation of an interstitial oncotic gradient favoring apical reabsorption, the RAD is superior to the current PT-MPS design for detecting apical water and electrolyte reabsorption. Despite attempts to measure ion flux in our PT-MPS using lithium as a marker of sodium transport in the presence and absence of inhibitors targeting either Na^+H^+ exchanger or Na^+K^+ ATPase, we were unable to recapitulate this function (data not shown). We are currently developing a 2-channel

microfluidic PT-MPS, with the second channel allowing a peritubular microvascular endothelia to be grown within the matrix compartment.[133] This design should provide a biomimetic for a more complex *in vivo*-like microenvironment that may facilitate assessment of electrolyte and water reabsorption in the proximal tubule. In addition, several studies have shown that co-culturing endothelial cells with proximal tubule epithelial cells enhances *in vivo*-like epithelial function.[118, 129, 131]

In summary, for the first time, we have a high-fidelity system *in vitro* that allows reliable investigation of the fundamental biology of the renal tubule epithelium; the potential applications include tubular secretion of drugs, xenobiotics, and uremic toxins, as well as the ability to assess toxic injury response. To our knowledge, this is the first demonstration of a human proximal tubular cell *in vitro* system that can effectively model basolateral solute transport, apical solute uptake, and intracellular enzymatic function in a physiologically relevant manner. Moreover, our PT-MPS has the potential for integration of multiple cell types— epithelial cells, pericytes, and microvascular endothelial cells in a spatial alignment that would fully reconstitute a tubulointerstitial environment.[117] In time, we envision the PT-MPS will be extended to investigation into pathophysiological processes at the tubule-interstitium that underlie acute kidney injury and chronic kidney diseases (CKD), as well as transport and metabolic processes governing the renal handling of drugs and environmental toxicants in healthy and disease states.

5 Megalin-mediated Regulation of Vitamin D Homeostasis in PTECs

5.1 Abstract

The essential role of megalin in the physiological regulation of vitamin D metabolism has hereto been evaluated only in megalin-knockout mice and limited case reports of human hereditary defects. Through the use of primary human proximal tubule epithelial cells (PTECs) incorporated in a 3-dimensional proximal tubule microphysiological system (PT-MPS), we demonstrate that both $25OHD_3$ and $1\alpha,25(OH)_2D_3$ are actively transported into proximal tubule epithelium via megalin-mediated endocytosis while bound to vitamin D binding protein (DBP) . Co-administration of 1 μM $25OHD_3$ and a range of $1\alpha,25(OH)_2D_3$ concentrations with DBP resulted in a dose-dependent increase in the appearance of $24,25(OH)_2D_3$ in the efflux media. In the presence of DBP, the maximal induction of $24,25(OH)_2D_3$ formation clearance was over 40-fold greater than the baseline activity. Inhibition of megalin function decreased the induction of both cytochrome P450 24A1 protein levels and 24-hydroxylase enzymatic activity following perfusion with $1\alpha,25(OH)2D_3$ in the presence of DBP. These results suggest a novel role for vitamin D binding protein in the intracellular trafficking of $1\alpha,25(OH)_2D_3$ to the vitamin D receptor (VDR). The interplay between megalin and vitamin D bioactivation was further characterized as a reciprocal relationship through demonstration of significant dose–dependent suppression of megalin gene expression by $1\alpha,25(OH)_2D_3$. This suggests that megalin may be part of the same intracrine and endocrine feedback loops that tightly regulate other proteins important to vitamin D homeostasis.

5.2 Introduction to Chapter 5

Vitamin D is vital for the regulation of systemic mineral homeostasis.[42] To elicit many of its biological effects, circulating vitamin D must first be metabolized in the liver to $25OHD_3$ primarily by cytochrome P450 2R1 (CYP2R1) and then in the kidney proximal tubule epithelium to $1\alpha,25(OH)_2D_3$ by cytochrome P450 27B1 (CYP27B1).[42] Unlike hepatic 25-hydroxylation, renal 1α-hydroxylation is a tightly regulated process, controlled by a number of intracrine- and endocrine-mediated feedback loops.[134-136] When levels of calcium are low, parathyroid hormone (PTH), a potent inducer of renal CYP27B1, is released from the parathyroid gland to increase production of $1\alpha,25(OH)_2D_3$ in the kidneys.[42, 57] Conversely, when systemic concentrations of $1\alpha,25(OH)_2D_3$ are elevated, a compensatory vitamin D receptor (VDR)-dependent induction of renal cytochrome P450 24A1 (CYP24A1), the 24-hydroxylase responsible for the metabolic inactivation of $1\alpha,25(OH)_2D_3$ and 25OHD3, acts to maintain $1\alpha,25(OH)_2D_3$ at levels sufficient for bone mineral homeostasis.[55, 136]

In order for the proximal tubule epithelial cells (PTECs) to sense and respond to systemic demands for more or less $1\alpha,25(OH)_2D_3$, both $1\alpha,25(OH)_2D_3$ and its metabolic precursor, $25OHD_3$, must gain access to the PTECs. Both $1\alpha,25(OH)_2D_3$ and $25OHD_3$ circulate tightly bound to vitamin D binding protein (DBP) and, to a lesser extent, albumin.[137, 138] As a result, passive partitioning of the unbound "free" hormone and prohormone would yield low unbound intracellular concentrations and biological responses.[42] In 1999, *Nykjaer et al.* discovered that the major route by which $25OHD_3$ accesses the murine proximal tubule epithelium is via megalin-mediated endocytosis of the DBP-bound hormone from the glomerular ultra-filtrate.[139] In their seminal paper on the subject, the authors demonstrated binding and co-localization of DBP and megalin in cryopreserved mouse kidney sections.[139] They also

observed comparatively greater urinary excretion of DBP in megalin knockout mice and noted that renal reuptake of DBP by perfused rat proximal tubules was reduced upon administration of receptor associated protein (RAP), an inhibitor of megalin function.[139] Bone formation defects were also observed in megalin-knockout mice, highlighting the physiological significance of megalin-mediated uptake of DBP-bound vitamin D metabolites.[139, 140] Around the same time as the knockout mouse studies were being conducted, *Liu et al.* reported observations of $1\alpha,25(OH)_2D_3$-mediated regulation of megalin expression in immortalized rat proximal tubule epithelial cells.[63] Using a northern blot analysis, they observed that $1\alpha,25(OH)_2D_3$ treatment appeared to induce megalin gene transcription.[63]

Taken together, the separate findings of the *Nykjaer et al.* and *Liu et al.* studies have important implications for the role of megalin in the physiological maintenance of vitamin D homeostasis. If $1\alpha,25(OH)_2D_3$ promotes megalin expression, and if megalin-mediated uptake is essential to renal delivery of vitamin D, then diminished renal $1\alpha,25(OH)_2D_3$ synthesis, such as in chronic kidney disease (CKD), might reduce megalin expression. This in turn would reduce $25OHD_3$ uptake, theoretically further reducing $1\alpha,25(OH)_2D_3$ synthesis, and perpetuating a feedback loop of progressively deteriorating vitamin D status. While this "vicious cycle" hypothesis of positive feedback has been described in a number of reviews,[141-143] we are not aware of any *in vitro* or *in vivo* confirmatory studies evaluating the relationship between $1\alpha,25(OH)_2D_3$ and megalin expression in the healthy human kidney.

Although some case studies of individuals with rare diseases that affect megalin expression/localization have noted increased urinary excretion of DBP, there is only limited information of systemic vitamin D status in these patients. Furthermore, what limited information is available may not be translatable to individuals without these diseases. The jump

from animal studies to experimental human studies has thus far been hindered by the lack of a feasible and ethical means of delivering and sampling from an isolated human proximal tubule *in vivo*. The ability to conduct experiments in such a setting would permit researchers to investigate the metabolic fate and biochemical actions of vitamin D metabolites in the kidney. The recent development of a 3-dimensional proximal tubule microphysiological system (PT-MPS) that recapitulates the physiological functions of the renal proximal tubule now permits the continued exploration of the role of megalin in the regulation of systemic vitamin D homeostasis.[40] The development of this system is described in Chapter 4. Here in Chapter 5, we describe results of a series of experiments conducted using the *in vivo*-like environment of the PT-MPS and conventional 2-dimensional PTEC cultures. These experiments were designed to evaluate whether megalin plays a role in the proximal tubular uptake of vitamin D metabolites and whether bioactive vitamin D plays a reciprocal role in regulating the expression of megalin in humans.

5.3 Materials and Methods

5.3.1 Chemicals and Reagents

Bovine serum albumin, hydrocortisone, Tween-20 and Triton X-100 were purchased from Sigma-Aldrich (St. Louis, MO). 16% Formaldehyde (methanol free) was purchased from Polysciences (Warrington, PA). Vitamin D metabolites were obtained from Toronto Research Chemicals (Toronto, Ontario). D-Sucrose, methanol, isopropanol, hexanes, methylene chloride, hydrochloric acid, Dulbecco's phosphate-buffered saline with (DPBS) and without ($DPBS^{++}$) calcium and magnesium, 50:50 Dulbecco’s modified eagle medium with Ham’s F-12 (DMEM/F12), penicillin-streptomycin-amphotericin B, insulin-transferrin-selenium A solution

(ITS-A), TRIzol reagent, High Capacity cDNA Reverse Transcription Kit with RNase Inhibitor, TaqMan gene expression assays, fetal bovine serum (FBS), Trypsin EDTA, ProLong Gold Antifade reagent with/without 4',6-diamidino-2-phenylindole (DAPI), rabbit anti-human CYP24A1 antibody, Alexa Fluor 488 protein labeling kit and Lab-Tek II 4-well chambered cover glass systems were obtained from Thermo-Fisher Scientific (Waltham, MA). Mixed type human vitamin D binding protein (DBP) was purchased from Athens Research & Technology (Athens, GA). Alexa Fluor 594 conjugated donkey anti-mouse IgG, Alexa Fluor 488 conjugated donkey anti-rabbit IgG, Alexa Fluor 488 conjugated donkey anti-goat IgG, rabbit anti-megalin and mouse anti-sodium-potassium ATPase antibodies were purchased from Abcam (Cambridge, MA). Microfluidic platforms were obtained from Nortis (Woodinville, WA). Human receptor-associated protein (RAP) was purchased from Innovative Research (Novi, MI). Non-pepsinized rat tail collagen I was purchased from Ibidi (Martinsried, Germany). Collagen IV, Matrigel®, Transwell® inserts and tissue culture-treated 6-well plates were obtained from Corning (Corning, NY).

5.3.2 Statistical Analysis

All statistical analyses were conducted using GraphPad Prism version 5.04 (GraphPad Software, La Jolla, CA). Data in figures depict the arithmetic mean ± SEM unless otherwise stated. All statistical tests evaluating “fold-changes” in the data (i.e. ratios) utilized log-transformed data to ensure parity between fold-reductions and fold-increases. Whenever possible, data was paired by kidney tissue donor. This paired comparison of log-transformed ratios is referred to in Graphpad Prism and throughout this paper as a paired ratio t-test. A p-

value of < 0.05 was considered statistically significant and $p < 0.01$ was considered very statistically significant.

5.3.3 Cell Culture

Healthy resections of kidney cortical tissue were obtained during the surgical removal of renal cell carcinomas at the University of Washington Medical Center. The protocol was approved by the University of Washington Human Subjects Institutional Review Board (protocol # STUDY00001297). Human PTECs were isolated from kidney tissue and cultured as described in Chapter 4. PTECs (passage 1-5) were either seeded into 4-well chamber slides, 6-well plates, 24-well Transwell® inserts or single-channel Nortis microfluidic tubules to constitute a proximal tubule microphysiological system (PT-MPS). Cells cultured in all platforms were then maintained under previously established "standard" cell culture conditions of DMEM/F12 supplemented with ITS-A, penicillin, streptomycin, amphotericin B and 50 nM hydrocortisone. Cells cultured in the PT-MPS were perfused with media at a rate of 0.5 µL/min.

5.3.4 ICC Staining for Megalin in Cultured PTECs

Because validated commercially-available antibodies for megalin require heat-mediated antigen retrieval, and the MPS platform currently does not permit this technique, we were performed immunocytochemical (ICC) staining for megalin protein localization in 2-dimensional Transwell® cell culture inserts. Briefly, PTECs were seeded at a density 2 $x10^5$ cells onto collagen IV-coated 24-well transparent Transwell® inserts and allowed to attach for 5 hours. Media was then removed from the inserts and replaced with media containing 0.25 mg/mL Matrigel® and left overnight. The next day, the media was replaced with media that did not

contain Matrigel® and the cells were left to culture under standard conditions. After 7 days, the cells were fixed in a solution of 4% formaldehyde and 2% sucrose for 10 minutes. They were then incubated in 50 mM ammonium chloride for 30 minutes and rinsed 3 times with $DPBS^{++}$. Next, cells were incubated in a solution of 0.05% Tween-20 in 10 mM sodium citrate buffer (pH = 6) for 20 minutes at 100°C. Cells were allowed to cool to room temperature before being blocked with PTB (a solution of 0.1% Triton X-100 and 5% bovine serum albumin in $DPBS^{++}$) for 30 minutes. A 1:25 dilution of rabbit anti-megalin and a 1:100 dilution of mouse anti-sodium-potassium ATPase primary antibodies in PTB was then added to the cell culture inserts and allowed to incubate at room temperature for 30 minutes. The inserts were washed three times with $DPBS^{++}$, and the cells were then incubated with a 1:1000 dilution of both Alexa Fluor 594 conjugated donkey anti-mouse IgG and Alexa Fluor 488 conjugated donkey anti-rabbit IgG for 30 minutes at room temperature. The cells were again rinsed 3 times with $DPBS^{++}$ and exposed to a 30 minute incubation with a 1:3 dilution of DAPI in $DPBS^{++}$. The cells were again rinsed 3 times with $DPBS^{++}$ before the porous membrane of the cell culture insert was extracted using a scalpel and tweezers. The membrane was then mounted in deionized water on glass microscope slides and imaged using a Zeiss LSM 780 confocal microscope from Carl Zeiss (Oberkochen, Germany). Confocal images were then processed in Velocity software version 6.3 from PerkinElmer (Waltham, MA).

5.3.5 Validation of DBP for the Delivery of $25OHD_3$ in the PT-MPS

After 5 days under standard culture conditions, 1 µM 25OHD3 was added to the PT-MPS media perfusate with either the previously established delivery vehicle (2% v/v FBS) or the experimental delivery vehicle (3 µM purified human DBP). Media exiting the PT-MPS luminal

path was collected over 24 hour intervals, for 3 days. All samples were stored at -80°C until they could be prepared for LC/MS-MS analysis using a previously established method.[40, 113] Quadruplicate PT-MPS (technical replicates) were used for each of the kidney tissue donors evaluated (biological replicates, n=3). Some 24,25$(OH)_2D_3$ contaminant was present in both the FBS and the plasma-derived human DBP. As such, net appearance rate, rather absolute appearance rate of 24,25$(OH)_2D_3$ in the efflux media was used for the assessment of vitamin metabolite disposition in the PT-MPS (Equation 1).

$$Net\ Efflux\ Appearance\ Rate_{24,25(OH)_2D_3} = \frac{[24,25(OH)_2D_3]_{outflow} - [24,25(OH)_2D_3]_{input}}{Duration\ of\ Collection\ Interval\ /\ Volume\ Collected} \quad (1)$$

The mean and standard deviation of net efflux appearance rate were calculated for each treatment (DBP or FBS) at each time point and two-way ANOVA was performed. A post-hoc Bonferroni procedure was used to make pairwise comparisons.

5.3.6 Comparison of the Relative Effects of DBP and FBS on the 1α,25$(OH)_2D_3$-Mediated Induction of CYP24A1

Having confirmed the suitability of purified human DBP as a delivery vehicle for vitamin D metabolites, we conducted an exploratory experiment with a single donor comparing the relative effects of the two delivery vehicle (FBS and DBP) on 1α,25$(OH)_2D_3$-mediated induction of 24-hydroxylation activity. Human PTECs from a single donor were cultured in the PT-MPS for 5 days post seeding, as previously described. All PT-MPS received 1 µM 25OHD_3 for 48 hours. Using equation 2, baseline 24,25$(OH)_2D_3$ formation clearance (CL_f) was determined for

each PT-MPS from metabolite concentrations in the media exiting the PT-MPS during hours 24 to 48 of the 2 day collection interval, following the addition of $25OHD_3$ to the perfusion media.

$$CL_f = \frac{Net\ Effluent\ Appearance\ Rate_{24,25(OH)_2D_3}}{[25OHD_3]_{outflow}} \quad (2)$$

In order to assess dose-dependency in the VDR-mediated induction of CYP24A1 expression and activity, the 16 tubules were randomly assigned to groups of 4 to receive either 500, 100, 10 nM of the VDR ligand, $1\alpha,25(OH)_2D_3$, or 0.1% ethanol vehicle control for the subsequent 48 hours. The CYP24A1 substrate, 1 μM $25OHD_3$, was also continued in all PT-MPS throughout the treatment phase. The $24,25(OH)_2D_3$ formation clearance during the "induction" phase was determined from media exiting each PT-MPS during hours 24 to 48 of the 2 day collection interval following the initiation of $1\alpha,25(OH)_2D_3$ induction. The experiment was conducted with either 2% v/v FBS or 3 μM DBP serving as the carrier vehicle for vitamin D metabolites. An overview of the experimental workflow is outlined in Figure 5.1. Fold-increase in CL_f from the baseline ($CL_{f(baseline\ phase,\ \ treatment)}$) to the induced state ($CL_{f(induction\ phase,\ \ treatment)}$) was calculated for each PT-MPS and standardized to the fold-change in CL_f from the baseline ($CL_{f(baseline\ phase,\ \ vehicle)}$) to the "induction" phase ($CL_{f(treatment\ phase,\ \ vehicle)}$) of the vehicle control (equation 3).

$$\%\ Increase = \left\{\left(\frac{CL_{f(induction\ phase,\ \ treatment)}}{CL_{f(baseline\ phase,\ \ treatment)}} \Big/ \frac{CL_{f(induction\ phase,\ \ vehicle)}}{CL_{f(baseline\ phase,\ \ vehicle)}}\right) - 1\right\} \times 100\% \quad (3)$$

The parameters of maximal induction (E_{max}) and the concentration of 1α,25(OH)$_2$D$_3$ at which half maximal induction is observed (EC_{50}) were then estimated using the simple E_{max} model, outlined in equation 4.

$$\%\ Increase = \frac{E_{max} \times [1\alpha 25(\mathrm{OH})_2 D_3]}{EC_{50} + [1\alpha 25(\mathrm{OH})_2 D_3]} \quad (4)$$

The estimated E_{max} and EC_{50} for the dose-dependent induction of 24-hydroxylation activity was then visually compared between PT-MPS supplemented with 2% v/v FBS versus 3 µM DBP.

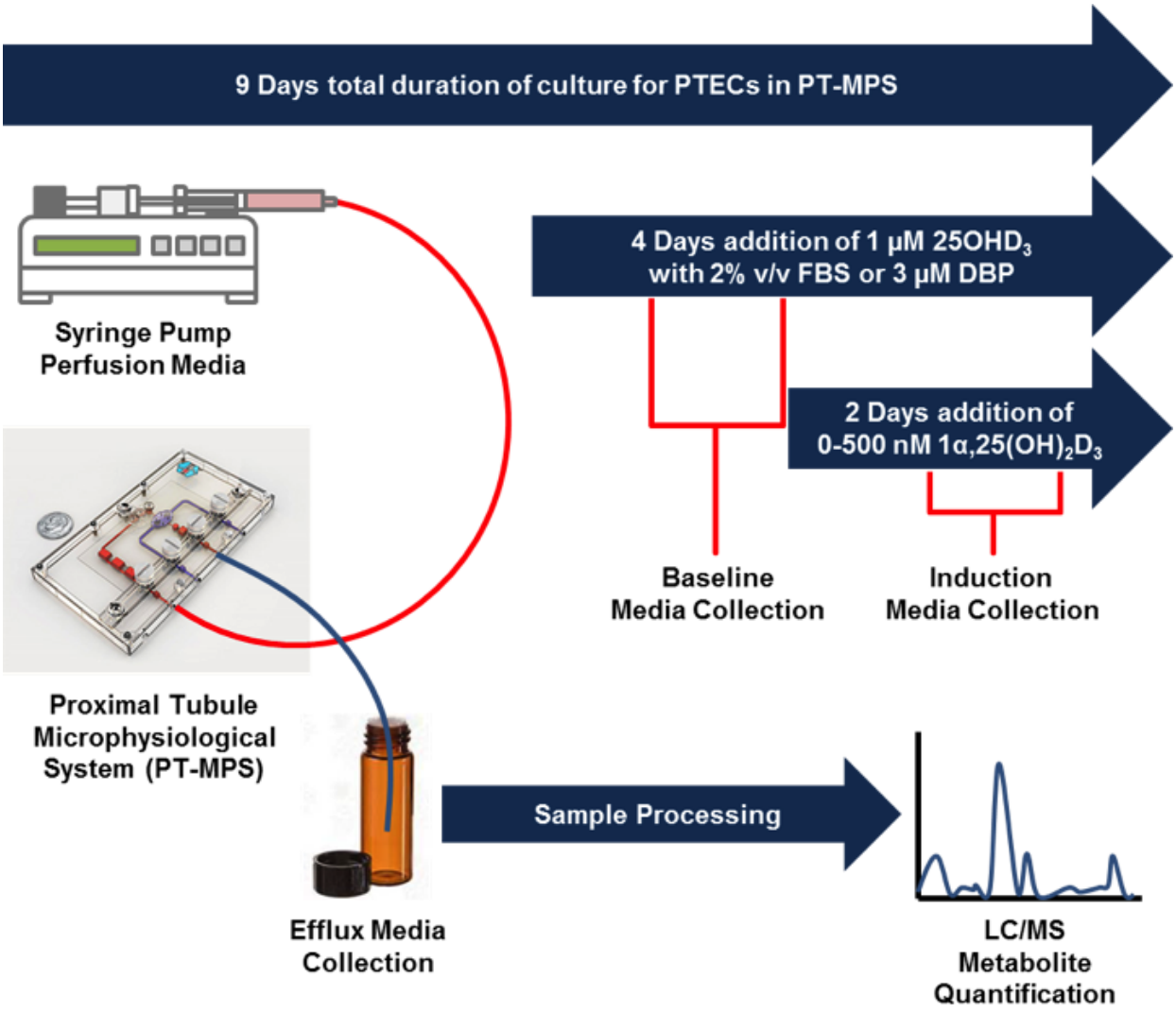

Figure 5.1. General scheme for experiments evaluating dose-dependent regulation of CYP24A1 by 1α,25(OH)$_2$D$_3$ in the PT-MPS. PT-MPS units are perfused with media containing 1 µM 25OHD$_3$ for 48 hours with either 2% v/v FBS or 3 µM DBP serving as a carrier vehicle for vitamin D metabolites. Baseline 24,25(OH)$_2$D$_3$ formation clearance is determined for each PT-MPS from metabolite concentrations in the media exiting the PT-MPS during the 24 to 48 hour period of the "baseline" phase. The various PT-MPS then receive a range of 1α,25(OH)$_2$D$_3$ concentrations or a vehicle control (0.1% ethanol) for the subsequent 48 hours. The CYP24A1 substrate (1 µM 25OHD$_3$) and the respective carrier protein source (2% v/v FBS or 3 µM DBP) for each PT-MPS is continued throughout the "induction" phase. The 24,25(OH)$_2$D$_3$ formation clearance during the "induction" phase is determined from the efflux media of each PT-MPS during hours 24 to 48 of the 2 day collection interval following the initiation of 1α,25(OH)$_2$D$_3$ co-treatment. Fold-increase in 24,25(OH)$_2$D$_3$ formation clearance from the baseline to the induced state is calculated for each PT-MPS receiving 1α,25(OH)$_2$D$_3$ and standardized as a percentage increase in 24,25(OH)$_2$D$_3$ formation clearance over the vehicle control.

5.3.7 Evaluation of the Effect of RAP on the Uptake of DBP in PTECs

Alexa Fluor 488-conjugated vitamin D binding protein (A488-DBP) was synthesized using a commercially available kit, as previously described.[144, 145] PTECs were cultured for 5 days in collagen IV-coated glass-bottom 4-well chamber slides. The cells were then treated with 20 µg/mL A488-DBP under the following conditions: 4°C (inhibits all endocytosis), 37°C (optimal for endocytosis) and 37°C with an established inhibitor of megalin, 1 µM receptor-associated protein (RAP).[145-147] At 30 minutes, PTECs were rinsed with $DPBS^{++}$, washed with acetic acid (adjusted with hydrochloric acid to pH 2.8) to remove cell surface-associated DBP, fixed for 20 minutes with ice-cold methanol, and then stored in anti-fade reagent. Quantification of cell-associated green fluorescence was determined in ImageJ using established methodologies.[148, 149] Differences in mean cell-associated fluorescence were evaluated by standardizing fluorescence measurements to each donor-specific 4°C control and performing a ratio t-test, paired by donor (n=5 biological replicates), comparing the cells subjected to 37° C with and without RAP co-incubation. Following fluorescence quantification, anti-fade reagent with 4',6-diamidino-2-phenylindole (DAPI) was then applied to cells in order to visualize nuclei in the representative images taken from confluent portions of the cell monolayers.

5.3.8 Evaluation of the Effect of RAP on the Uptake and 24-hydroxylation of $25OHD_3$

PT-MPS were cultured under standard conditions (16-20 PT-MPS per donor) for 5 days. Then PT-MPS were perfused (0.5 µL/min) for 48 hours with 3 µM DBP-supplemented media containing 500 nM $1\alpha,25(OH)_2D_3$. This 48 hour pre-incubation of $1\alpha,25(OH)_2D_3$ was employed to induce CYP24A1 activity and enhance sensitivity for quantifying the 24-hydroxylation of the relatively lower $25OHD_3$ concentrations. In order to remove residual $1\alpha,25(OH)_2D_3$ and promote

the equilibration of incoming vitamin D metabolites, an 8 hour accelerated perfusion (2.5 µL/min) of DBP-supplemented media without 1α,25$(OH)_2D_3$, but containing different 25OHD_3 concentrations (ranging from 0.25 to 3 µM), was administered to the PT-MPS. Perfusion with 25OHD_3, in the DBP-supplemented media was then reduced to 0.5 µL/min and 1 µM RAP was administered to half of the PT-MPS at each 25OHD_3 concentration. Media was collected for 1 day and concentrations of 25OHD_3 and 24,25$(OH)_2D_3$ were determined using a previously established LC-MS/MS method.[40, 113] The disappearance rate of 25OHD_3 from the perfusion media was calculated according to equation 5.

$$25OHD_3\ Disappearance\ Rate = \frac{[25OHD_3]_{input} - [25OHD_3]_{outflow}}{Duration\ of\ Collection\ Interval\ /\ Volume\ Collected} \quad (5)$$

The net appearance rate for 24,25$(OH)_2D_3$ was also calculated across the range of 25OHD_3 input concentrations (equation 1). Given the roughly proportional increase in both 24,25$(OH)_2D_3$ net appearance and 25OHD_3 disappearance rate across the range of 25OHD_3 input concentrations, a simple linear regression model was fit to the data. Under these linear conditions, the slope of the 24,25$(OH)_2D_3$ net appearance and 25OHD_3 disappearance rate across the concentration reflects the intrinsic clearance of 24,25$(OH)_2D_3$ appearance ($CL_{int,24,25(OH)2D3}$) and 25OHD_3 disappearance ($CL_{int,25OHD3}$) respectively. The effect of RAP on each intrinsic clearance was evaluated using ratio t-tests paired by kidney tissue donor (n=5 biological replicates). De-identified subject information for each kidney tissue donor is provided in Table 5.1.

Table. 5.1. Kidney tissue donor characteristics in 25OHD$_3$ uptake/loss experiment

Donor No.	Age	Sex	Ethnicity	Pre-existing Conditions	Reason for Nephrectomy	Final Pathology
1	58	Male	White	HTN, sleep apnea	Renal mass (bilateral)	Papillary RCC, multiple papillary adenomas
2	56	Male	White	None reported	Renal mass (left)	Clear cell RCC
3	58	Male	White	HTN, hernia	Renal mass (right)	Unclassified RCC with clear cell features
4	58	Male	White	None reported	Renal mass (right)	Clear cell RCC
5	40	Male	African American	Methamphetamine use, Deep Vein thrombosis	Renal mass (left)	Clear Cell RCC

Table 5.2. Kidney tissue donor characteristics in 1α,25(OH)$_2$D$_3$–mediated induction experiment

Donor No.	Age	Sex	Ethnicity	Pre-existing Conditions	Reason for Nephrectomy	Final Pathology
1	65	Male	White	None reported	Renal mass	Not Available
2	49	Male	White	Clear cell RCC	Renal mass	Not Available
3	68	Male	White	HTN, GERD, Aortic Aneurysm, Diabetes Mellitus 2	Renal Mass (left)	Clear Cell RCC
4	62	Female	White	HTN, GERD, previous cervical, thyroid and breast carcinoma	Renal mass	Not Available
5	58	Male	White	HTN, sleep apnea	Renal mass (bilateral)	Papillary RCC

5.3.9 Evaluation of the Effect of RAP on 1α,25(OH)$_2$D$_3$-Mediated Induction of CYP24A1 Activity

The experimental design outlined in Figure 5.1 was modified so that all PT-MPS received 3 µM DBP as the carrier vehicle. During the induction phase, half of the PT-MPS, per 1α,25(OH)$_2$D$_3$ concentration, additionally received 1 µM of the megalin inhibitor, RAP. Fold induction of 24,25(OH)$_2$D$_3$ formation clearance was calculated as before and compared in the presence and absence of RAP. The experiment was then repeated for a total of 5 donors, two of which were also evaluated in the presence of 2000 nM 1α,25(OH)$_2$D$_3$ to confirm that near-maximal induction was likely being achieved where 500 nM 1α,25(OH)$_2$D$_3$ was the highest evaluated concentration. The shifts in EC_{50} and E_{max} were then evaluated using a paired ratio t-test comparing the estimated parameters from each donor in the presence and absence of RAP. De-identified subject information for each kidney tissue donor is provided in Table 5.2.

5.3.10 Evaluation of the Effect of RAP on 1α,25(OH)$_2$D$_3$-Mediated Induction of CYP24A1 Protein Accumulation

PT-MPS were maintained for 5 days under standard culture conditions. The culture media was then supplemented with 3 µM human DBP and the cells were treated with either 500 nM 1α,25(OH)$_2$D$_3$ in the presence or absence of 1 µM RAP or 0.1 % ethanol vehicle control. After 2 days of culture in these treatment conditions, the cells were then fixed by flowing a solution of 4% formaldehyde and 2% D-sucrose in DPBS^{++} at 10 µL/min through the PT-MPS for 20 minutes. ICC staining was then conducted using a previously established method, described in Chapter 4. For the ICC staining, a

1:200 dilution of goat anti-CYP24A1 (primary antibody) and a 1:1000 dilution of Alexa Fluor 488 conjugated donkey anti-goat IgG (secondary antibody) were used. Images of the PT-MPS tubules were captured on a Nikon Eclipse Ti fluorescent microscope (Melville, NY).

5.3.11 Characterization of the Effects of 1α,25(OH)$_2$D$_3$ on Megalin Gene Expression in PTECs

In order to increase total mRNA yield and improve sensitivity for megalin gene expression, human PTECs were cultured in collagen IV-coated 6-well plates, rather than the PT-MPS. The cells were cultured under "standard conditions" for 5 days before being exposed to a range of concentrations (0-500 nM) of 1α,25(OH)$_2$D$_3$. After 24 hours of exposure, the cells were homogenized in 1 mL of TriZol reagent. The samples were collected and stored at -80°C until the time of processing and analysis. The mRNA was then isolated according to the TriZol manufacturer-supplied protocol, quantified on a NanoDrop ND-2000 spectrophotometer from Thermo-Fisher (Waltham, MA). Isolated RNA was mixed with other components (including RNase inhibitor) of the high-capacity cDNA reverse transcription kit according to the manufacturer-supplied protocol. Reverse transcription was conducted in a PTC-200 thermal cycler (Bio-Rad, Hercules, CA) under the following conditions: 10 minutes at 25°C, 120 minutes at 37°C and 5 seconds at 85°C. Quantitative real-time polymerase chain reactions were then performed under the following conditions: warm up at 50°C for 10:00, followed by 40 cycles of 95°C for 5:10 and 60°C for 0:30. TaqMan gene expression assays were used to evaluate the dose-dependent effects of 1α,25(OH)$_2$D$_3$ on megalin, CYP24A1 (inductive control) and

CYP27B1 (suppressive control) on relative gene expression. The ΔΔCt method, using glyceraldehyde 3-phosphate dehydrogenase (GAPDH) as a housekeeping gene, was employed to quantify relative amounts of megalin, CYP24A1 and CYP27B1 mRNA transcripts in all samples. A one-way ANOVA, treating different $1\alpha,25(OH)_2D_3$ doses in a given donor as repeated measures, was performed on the log-transformed data. Post-hoc paired ratio t-tests (n=6 biological replicates) between each $1\alpha,25(OH)_2D_3$ dose and the vehicle control (0.1% ethanol) were then conducted for each of the genes evaluated (megalin, CYP24A1 and CYP27B1). Levels of CYP24A1 RNA were below the limit of quantification in the vehicle control group so the group was omitted from the statistical analysis. Post-hoc t-tests for CYP24A1 compared gene expression in cells treated with 1 nM $1\alpha,25(OH)_2D_3$ (rather than vehicle control) to those treated with higher doses.

5.4 Results

5.4.1 Megalin Localization in Cultured Human PTECs

Demonstration of proper expression and localization of megalin in primary PTECs was required to confirm the capability of our *in vitro* system to model *in vivo* megalin-mediated processes. As seen in Figure 5.2, megalin (depicted in green) is preferentially expressed along the apical and adjacent subapical regions of cultured PTECs. Sodium-potassium ATPase (depicted in red) serves as an established counterstain for cell basolateral membranes.[150] These findings of *in vivo*-like localization of megalin in cultured PTECs provides additional confidence in the utility of our *in vitro* system for assessing megalin-mediated uptake of DBP-bound $25OHD_3$ and $1\alpha,25(OH)_2D_3$ from the glomerular ultra-filtrate.

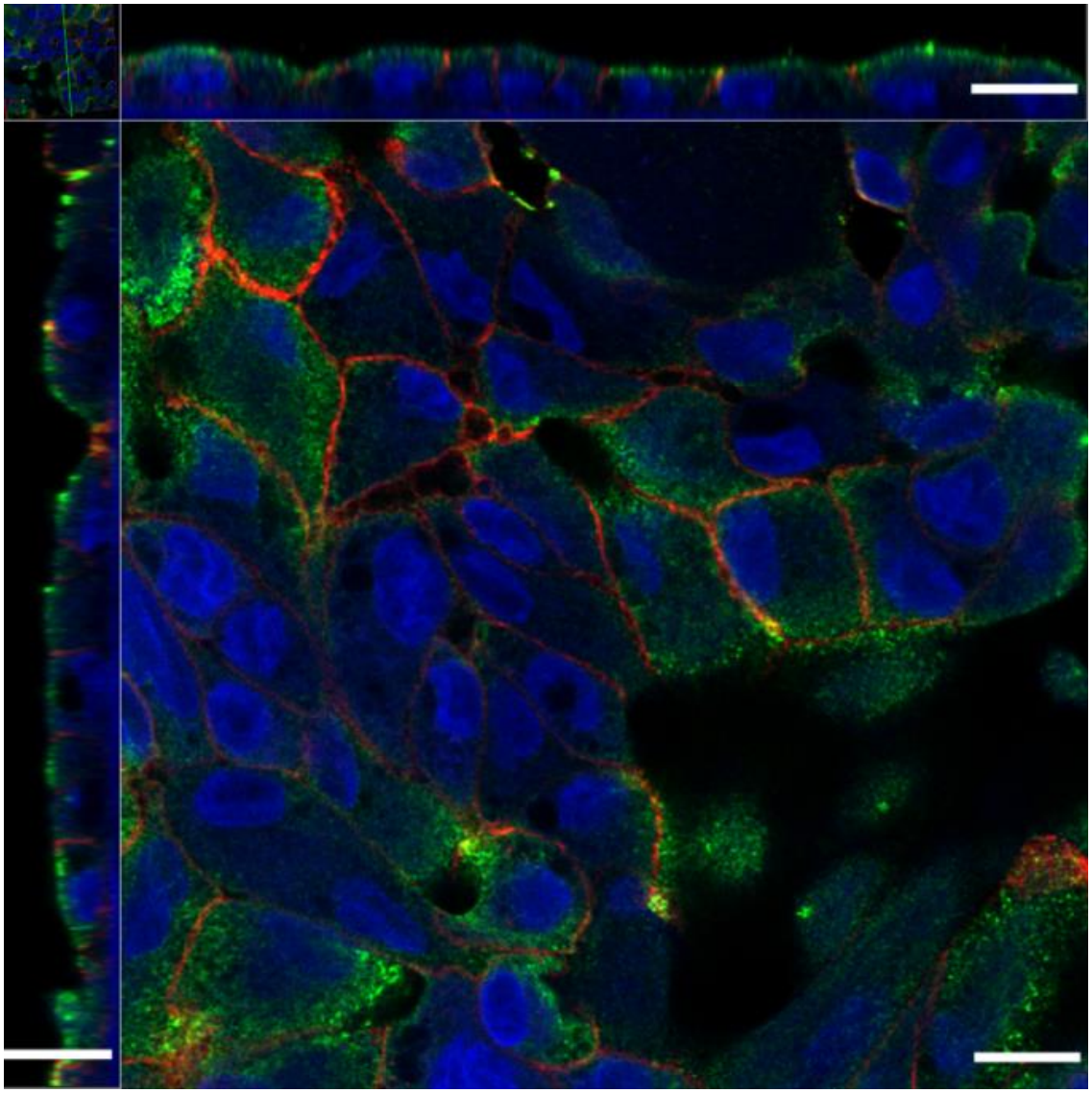

Figure 5.2. Megalin protein localization in PTECs. Megalin (green signal) is preferentially expressed along the apical and adjacent subapical regions of cultured human proximal tubule epithelial cells (PTECs), as is seen *in vivo*. Sodium-potassium ATPase (red signal) was used as a counterstain for the cells basolateral membranes. Scale bar represents 10 µm.

5.4.2 DBP is a Carrier Protein for Vitamin D Metabolites

Cells cultured in the PT-MPS with either 2% v/v FBS or 3 µM DBP as delivery vehicle for vitamin D metabolites exhibited net 24,25$(OH)_2D_3$ formation during the 24-48 hr and 48-72 hr collection intervals. Unlike with FBS, cells cultured with DBP exhibited a net loss of 24,25$(OH)_2D_3$ to the PT-MPS system during the 0-24 hr collection interval.

The difference in net 24,25$(OH)_2D_3$ formation rate between the FBS- and DBP-treated cells was significant for the 0-24 hr collection interval (Figure 5.3). These results demonstrate that purified human DBP (which provides a more controlled culture milieu than 2% v/v FBS) is an effective vehicle for the delivery of vitamin D metabolites to the PT-MPS.

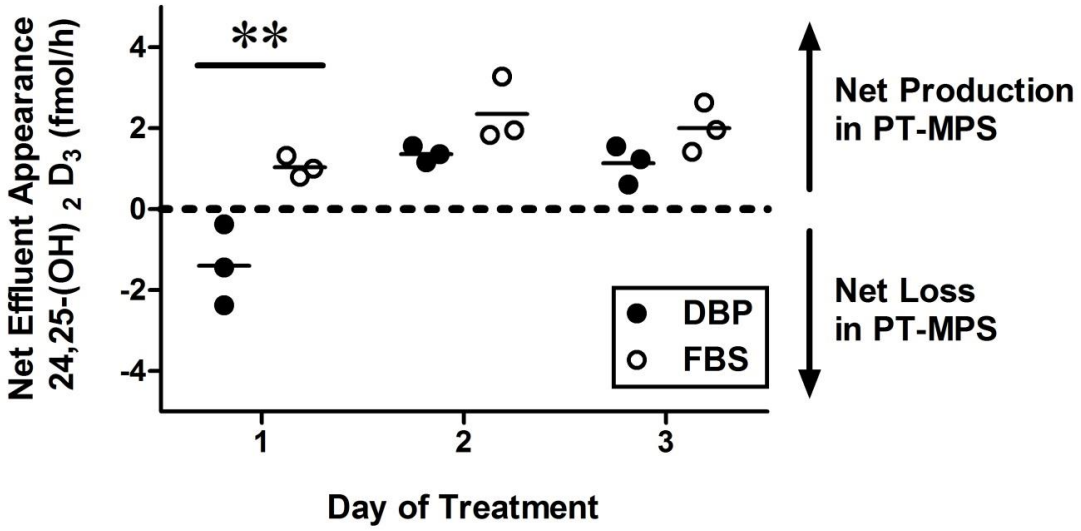

Figure 5.3. Comparison of FBS- and DBP-facilitated delivery on the metabolic formation and distribution of 24,25$(OH)_2D_3$ in the PT-MPS. Cells cultured in the PT-MPS with either 2% v/v FBS or 3 µM DBP as delivery vehicle for vitamin D metabolites exhibited net 24,25$(OH)_2D_3$ formation during the 24-48 hr and 48-72 hr collection intervals. Unlike with FBS, cells cultured with DBP exhibited a net loss of 24,25$(OH)_2D_3$ to the PT-MPS system during the 0-24 hr collection interval. The difference in net 24,25$(OH)_2D_3$ formation rate between the FBS- and DBP-treated cells was significant for the 0-24 hr collection interval. **Very statistically significant, $p < 0.01$.

5.4.3 Differential Effects of DBP and FBS on the Regulation of CYP24A1 Activity by 1α,25$(OH)_2D_3$

Having confirmed the suitability of purified human DBP as a delivery vehicle for vitamin D metabolites, we conducted an exploratory experiment in a single donor comparing the relative effects of the two delivery vehicles (FBS and DBP) on

$1\alpha,25(OH)_2D_3$-mediated induction of $24,25(OH)_2D_3$ formation clearance. Co-administration of 1 µM $25OHD_3$ and a range of $1\alpha,25(OH)_2D_3$ concentrations (0-500 nM) to the PT-MPS resulted in a dose-dependent increase in the appearance of $24,25(OH)_2D_3$ in the efflux media of both DBP- and FBS- supplemented perfusion media (Figure 5.4). The maximal induction (E_{max}) of $24,25(OH)_2D_3$ formation clearance in DBP-supplemented media was over 40-fold greater than the baseline activity and approximately 10-fold greater than the increase seen with FBS co-incubation. Given its physiological relevance, the remaining experiments were conducted using 3 µM DBP, rather than 2% v/v FBS, as the delivery vehicle for vitamin D metabolites to the PT-MPS.

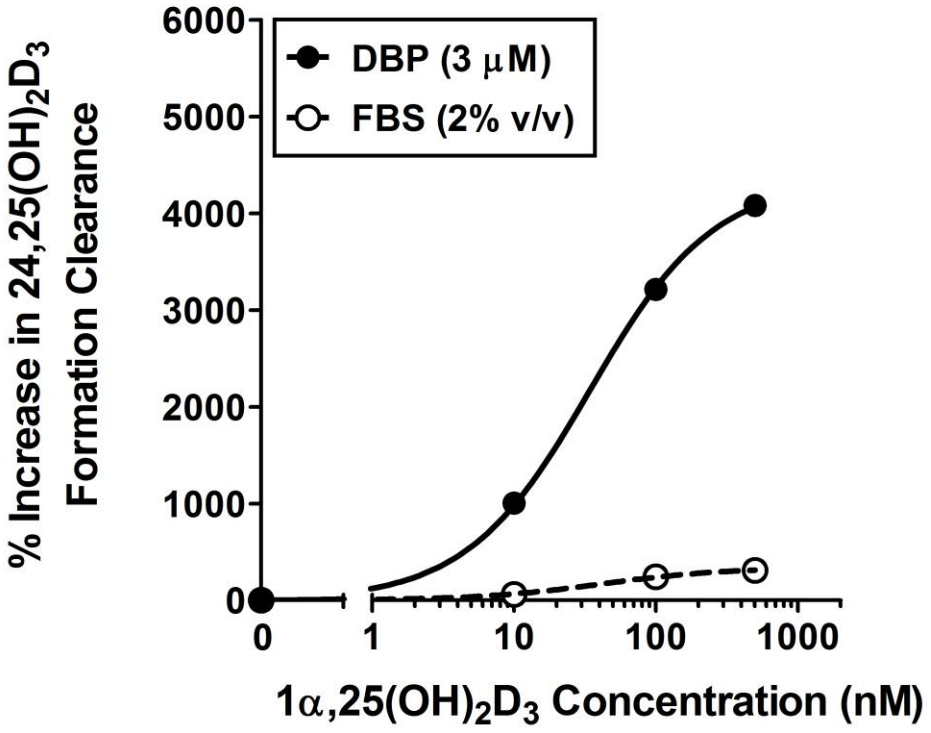

Figure 5.4. Relative effects of DBP and FBS on $1\alpha,25(OH)_2D_3$-mediated regulation of CYP24A1 activity in the PT-MPS. Co-incubation of $25OHD_3$ and across a range (0-500 nM) of $1\alpha,25(OH)_2D_3$ concentrations resulted in a dose-dependent increase in the appearance of $24,25(OH)_2D_3$ in the efflux media of both DBP- and FBS-supplemented perfusion media. The maximal induction (E_{max}) of $24,25(OH)_2D_3$ formation clearance in DBP-supplemented media was greater than that seen with FBS co-incubation.

5.4.4 Megalin Mediates the Uptake of DBP into PTECs

In order to determine if megalin-mediated processes contribute to the uptake of vitamin D metabolites into the renal tubular epithelium, we first evaluated the effects of an established megalin inhibitor, RAP, on the uptake of fluorescent Alexa 488-conjugated DBP (A488-DBP) by PTECs cultured in conventional 2D monolayers.

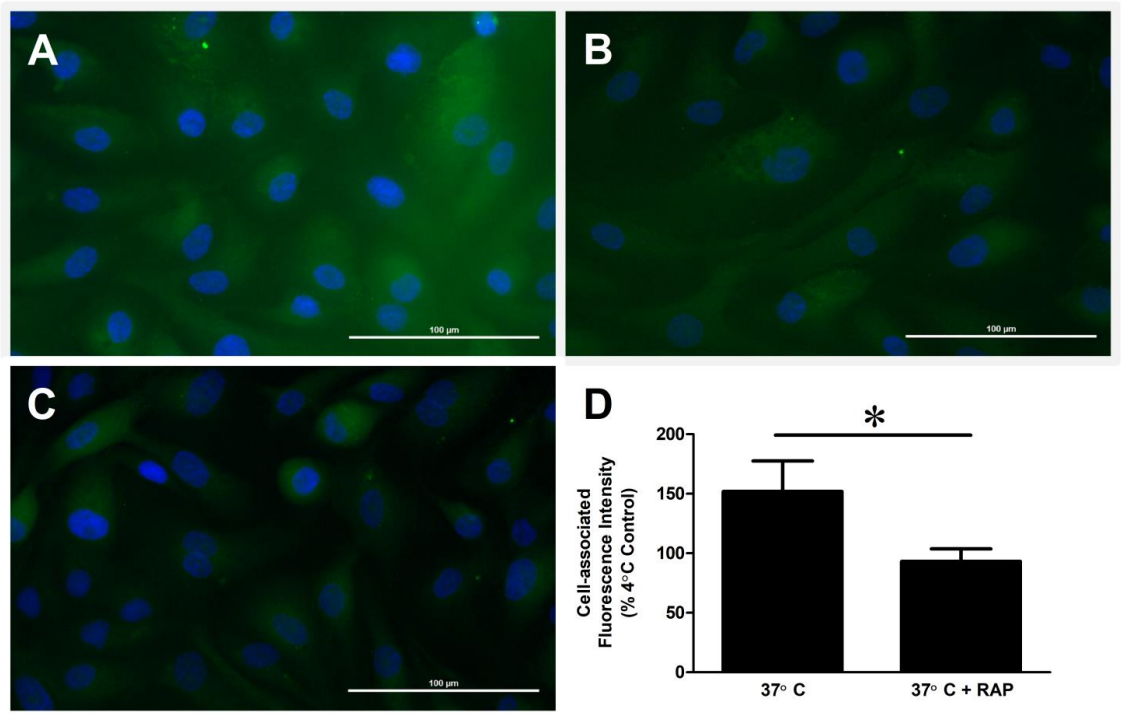

Figure 5.5. Megalin-mediated uptake of fluorescently-tagged DBP into PTECs. Cell-associated fluorescence in PTECs cultured at **(A)** 37°C, **(B)** 4°C, and **(C)** 37°C with 1 µM RAP. Fluorescence intensity was greater in PTECs incubated with A488-DBP at 37°C (optimal for endocytosis) relative to those incubated at 4°C, indicating endocytosis of DBP occurs in cultured human PTECs. **(D)** Semi-quantitation of cell-associated fluorescence revealed a significant reduction in fluorescence upon RAP co-administration at 37°. Apparent A488-DBP uptake was reduced down to levels comparable to those observed at 4°C, where endocytosis should be mostly suppressed.[145, 151] Columns reflect the arithmetic mean ± SEM. Scale bars represents 100 µm.

As shown in Figure 5.5, cell-associated fluorescence intensity was greater in cells incubated with A488-DBP at 37°C (optimal for endocytosis), relative to those incubated at 4°C, indicating endocytosis of DBP occurs in cultured human PTECs. Moreover, RAP

significantly reduced A488-DBP uptake down to levels comparable to those observed at 4°C, where receptor-mediated and non-specific forms of endocytosis are assumed to be inhibited.[145, 151] This suggests that uptake of DBP into cultured PTECs is predominantly via megalin-mediated endocytosis and that 1 μM RAP is sufficient to inhibit this process *in vitro*.

5.4.5 RAP Inhibits the Cellular Uptake of DBP-Bound 25OHD$_3$

After validating the ability of 1 μM RAP to inhibit megalin-mediated uptake of DBP into PTECs, we cultured cells to confluence in the PT-MPS and evaluated the effect of RAP on the uptake and catabolism of 25OHD$_3$ from the luminal perfusion medium. Both the rate of 24,24(OH)$_2$D$_3$ formation (Figure 5.6) and the loss of 25OHD$_3$ (Figure 5.7) from the perfusion media was observed to be roughly proportional to the empirically-measured range of 25OHD$_3$ input concentrations tested. While RAP co-administration resulted in a statistically-significantly 2.4-fold reduction in the intrinsic metabolic clearance of 25OHD$_3$ from the PT-MPS perfusion media, it had no apparent effect on the net appearance of 24,25(OH)$_2$D$_3$ in the perfusion media (Table 5.3).

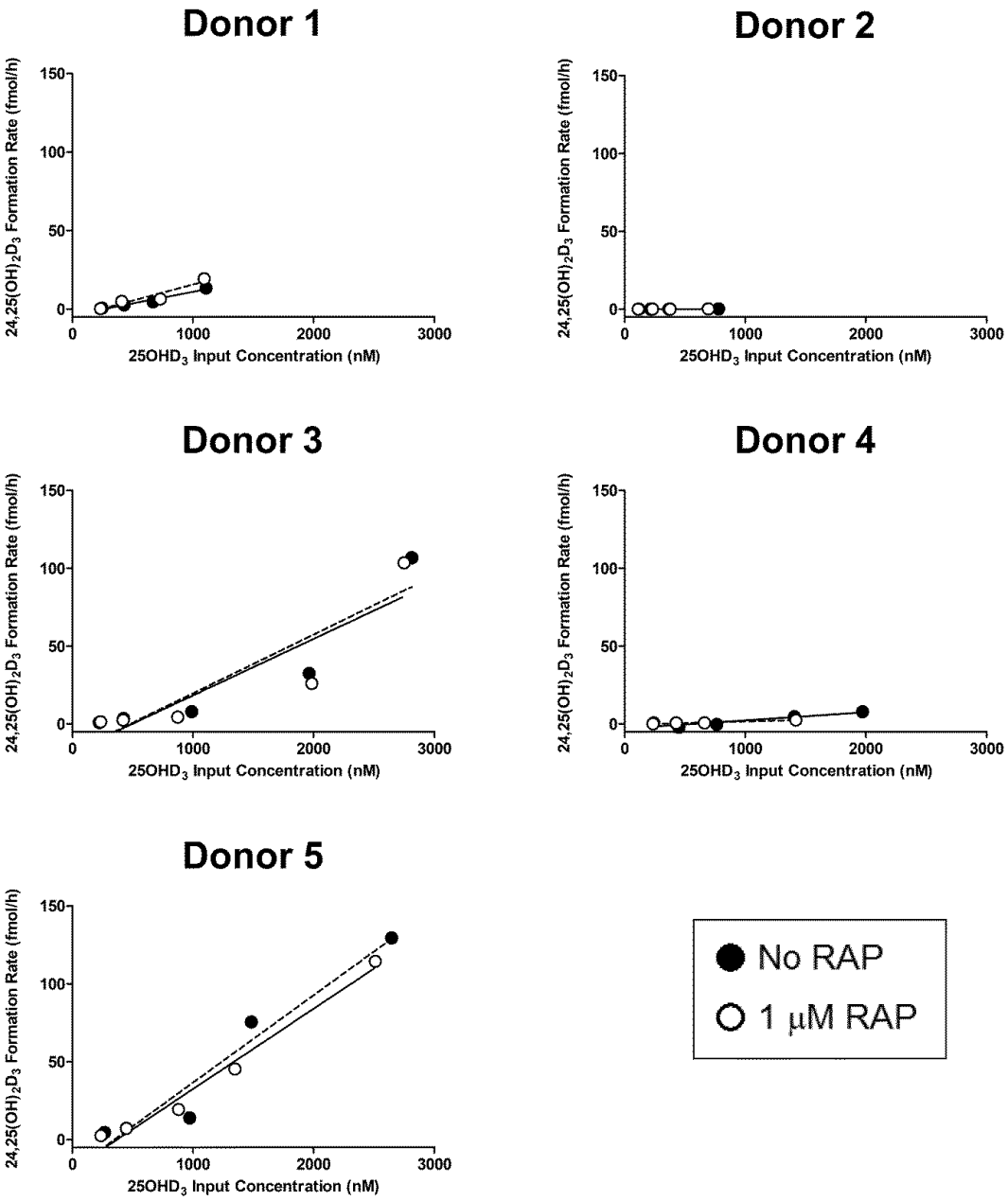

Figure 5.6. Megalin inhibition does not affect the formation of $24,25(OH)_2D_3$ from $25OHD_3$ in the PT-MPS. The rate of formation of $24,25(OH)_2D_3$ from $25OHD_3$ was observed to be roughly proportional to the $25OHD_3$ input concentrations across the measured range of input concentrations tested. There was no significant effect of RAP on the estimated intrinsic formation clearance of $24,25(OH)_2D_3$ from $25OHD_3$.

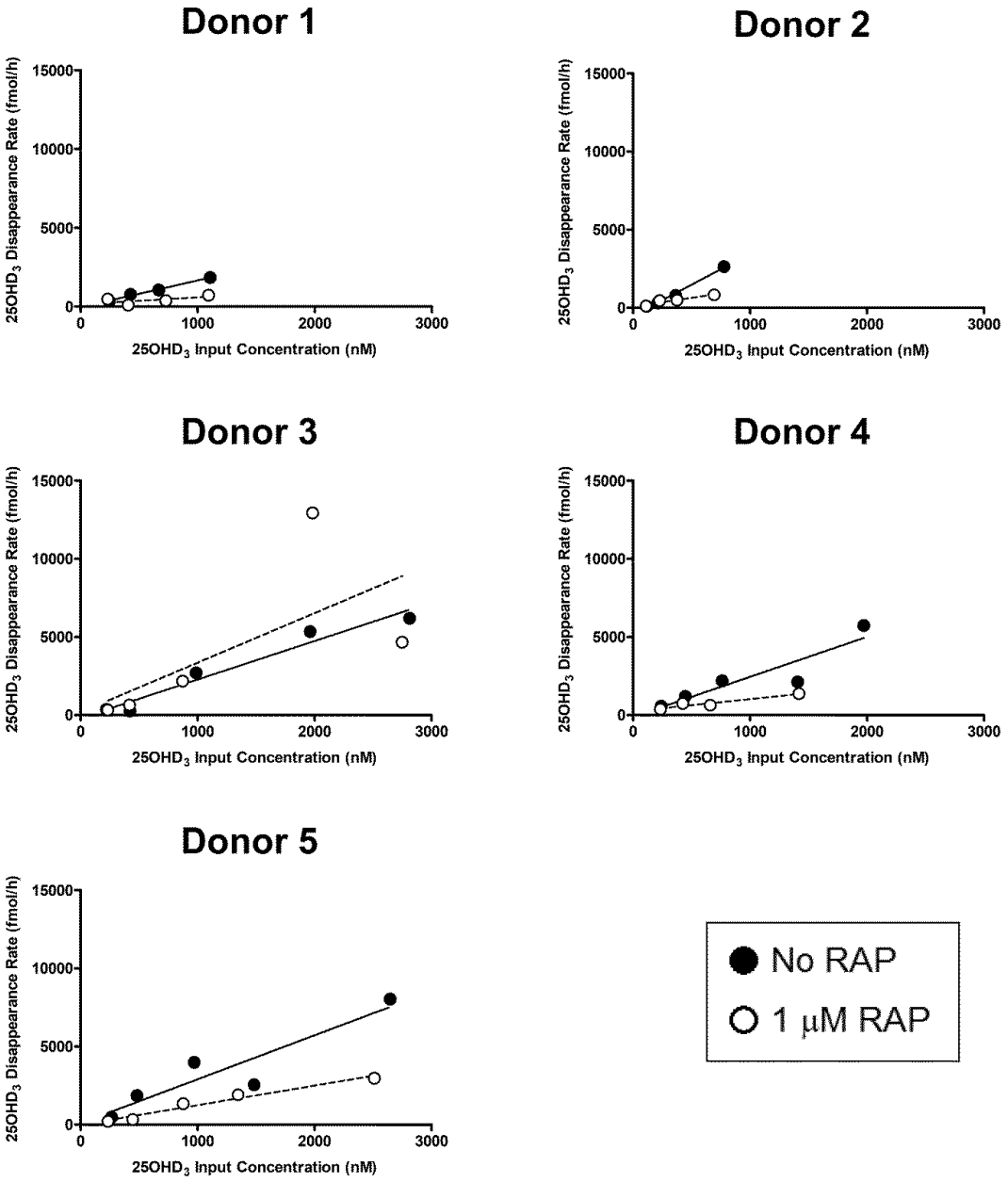

Figure 5.7. Megalin-mediated cellular uptake and loss of DBP-bound 25OHD$_3$ in the PT-MPS. The rate of loss of 25OHD$_3$ from the perfusion media was observed to be roughly proportional to the 25OHD$_3$ input concentrations across the measured range of input concentrations tested. RAP significantly reduced the estimated intrinsic clearance, reflected in slope of the linear regression line, of 25OHD$_3$ from the luminal perfusion media.

Table 5.3. Donor-specific effects of RAP on the intrinsic clearances of $24,25(OH)_2D_3$ formation and $25OHD_3$ loss.

	$CL_{int,24,25(OH)2D3}$ (µL/h)			$CL_{int,25OHD3}$ (µL/h)		
Donor No.	**No RAP**	**RAP**	**Fold-Change CL_{int}**	**No RAP**	**RAP**	**Fold-Change CL_{int}**
1	0.015	0.021	1.4 ↑	1.7	0.42	4.0 ↓
2	0.00029	0.00037	1.3 ↑	4.0	1.1	3.6 ↓
3	0.038	0.036	1.1 ↓	2.5	3.2	1.3 ↑
4	0.0052	0.0021	2.5 ↓	2.6	0.78	3.3 ↓
5	0.056	0.052	1.1 ↓	2.8	1.3	2.2 ↓
Mean†	0.023	0.022	1.1 ↓	2.7	1.4	*2.4 ↓
SD†	0.024	0.022	1.6	0.83	1.1	2.0

Treatment with the megalin inhibitor (RAP) significantly reduced the intrinsic clearance for $25OHD_3$ loss ($CL_{int,25OHD3}$**)** to PTECs cultured in the PT-MPS but had no significant effect on the intrinsic clearance of $24,25(OH)_2D_3$ formation ($CL_{int,24,25(OH)2D3}$**)**. †Geometric mean and geometric standard deviation calculated for "fold-change" (ratio) parameters. *Statistically significant, $p < 0.05$.

5.4.6 RAP Impairs 1α,25(OH)$_2$D$_3$–Mediated Induction of CYP24A1

Biologically active 1α,25(OH)$_2$D$_3$, like the pro-hormone (25OHD$_3$), circulates tightly bound to DBP.[137, 138] As such, protein-bound 1α,25(OH)$_2$D$_3$ represented a hereto unevaluated candidate for megalin-mediated delivery to the renal proximal tubule. In order to test whether megalin-mediated uptake of DBP-bound 1α,25(OH)$_2$D$_3$ is capable of modulating the intracellular availability of 1α,25(OH)$_2$D$_3$ for VDR-dependent pharmacologic activity (e.g. CYP24A1-mediated 24-hydroxylation of 25OHD$_3$) in the proximal tubule epithelium, additional experiments were performed. In brief, human PTECs cultured in the PT-MPS were perfused with 1 µM of 25OHD$_3$ and a baseline value of 24,25(OH)$_2$D$_3$ formation clearance was determined. Varying concentrations of 1α,25(OH)$_2$D$_3$ were then added to the perfusion medium in the presence or absence of a megalin inhibitor (RAP) and the percent increase in the rate of 24,25(OH)$_2$D$_3$ production was calculated as detailed in the methods. The mean concentration required for half-maximal effect (EC_{50}) of 1α,25(OH)$_2$D$_3$-mediated induction of 25OHD$_3$ 24-hydroxylation activity displayed a non-significant 1.5-fold rightward shift upon RAP co-treatment (Figure 5.8). However, inhibition of megalin by RAP resulted in a statistically significant 1.8-fold downward shift in the maximal inductive response (E_{max}). Donor-specific parameter estimates are outlined in Table 5.4.

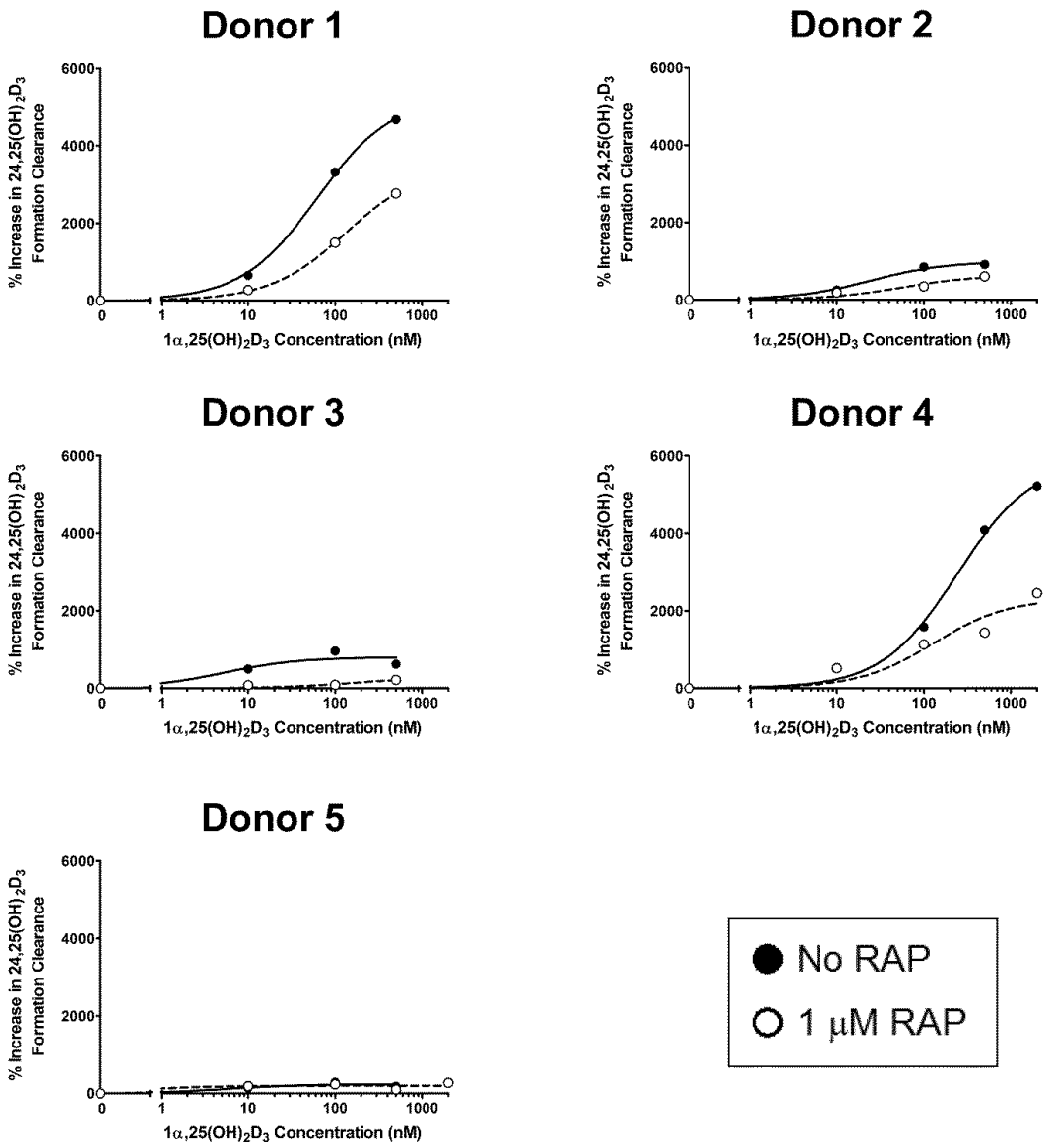

Figure 5.8. Megalin-mediated uptake of DBP-bound 1α,25(OH)$_2$D$_3$ is critical for maximal VDR-dependent induction of CYP24A1 activity in the PT-MPS. The formation of 24,25(OH)$_2$D$_3$ from 25OHD$_3$ increased with increasing concentrations of 1α,25(OH)$_2$D$_3$. Co-incubation with RAP resulted in a statistically significant downward shift in the maximal inductive response (E_{max}) but had no significant effect on the concentration required for half-maximal effect (EC_{50}).

Table 5.4. Donor-specific effects of RAP on 1α,25(OH)$_2$D$_3$–mediated induction of 24,25(OH)$_2$D$_3$ formation clearance.

	EC_{50} (nM)			E_{max} (% Increase from Baseline)		
Donor No.	**No RAP**	**RAP**	**Fold-Change EC_{50}**	**No RAP**	**RAP**	**Fold-Change E_{max}**
1	62	130	2.1 ↑	5300	3500	1.5 ↓
2	25	56	2.2 ↑	990	640	1.5 ↓
3	5.3	170	32 ↑	800	280	2.9 ↓
4	240	130	1.8 ↓	5900	2300	2.6 ↓
5	5.6	0.61	9.2 ↓	235	200	1.2 ↓
Mean†	68	97	1.5 ↑	2600	1400	*1.8 ↓
SD†	99	68	8.1	2700	1500	1.5

Treatment with the megalin inhibitor (RAP) significantly reduced the maximal inducibility (E_{max}) for the 1α,25(OH)$_2$D$_3$–mediated induction of 24,25(OH)$_2$D$_3$ formation clearance clearance in the PT-MPS but had no significant effect on the concentration of 1α,25(OH)$_2$D$_3$ required for half-maximal induction (EC_{50}) of 24,25(OH)$_2$D$_3$ formation clearance. †Geometric mean and geometric standard deviation calculated for "fold-change" (ratio) parameters. *Statistically significant $p < 0.05$.

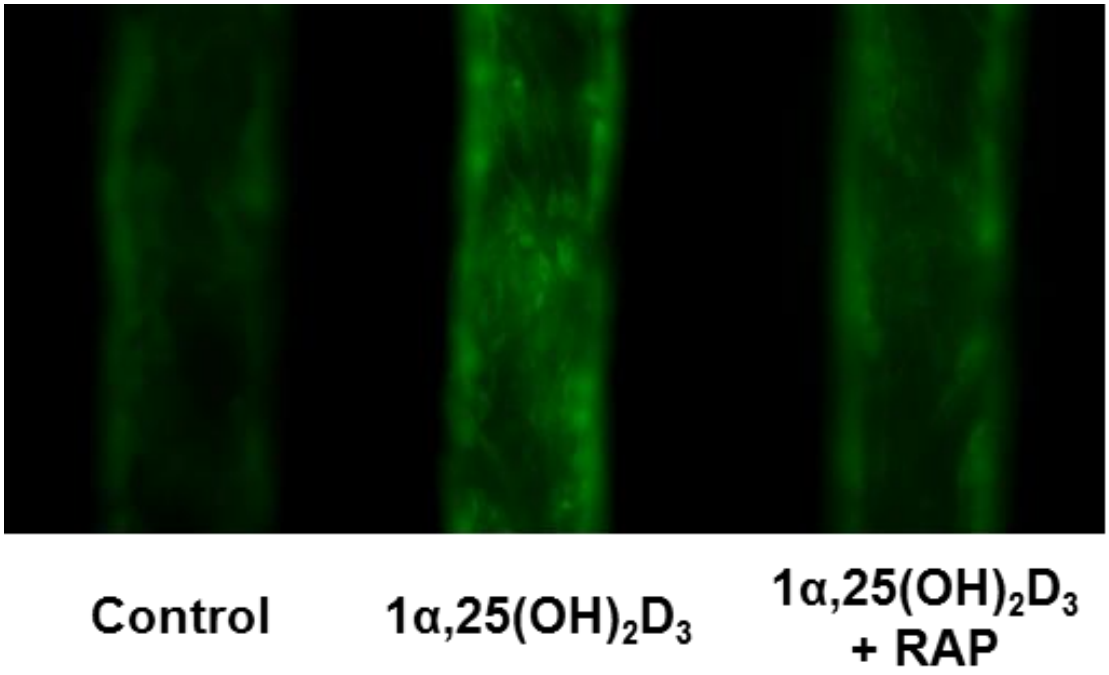

Figure 5.9. Megalin inhibition impairs 1α,25(OH)$_2$D$_3$-mediated induction of CYP24A1 protein accumulation in the PT-MPS. Treatment of PTECs in the PT-MPS with 500 nM 1α,25(OH)$_2$D$_3$ (center) resulted in increases in fluorescent signal for CYP24A1 protein compared to the vehicle control (left). This inductive effect appeared to be partially reversed with RAP co-administration (right). For reference, the approximate diameter of PT-MPS tubules shown above is 120 μm.

A separate experiment was then conducted to assess whether the observed RAP-dependent reductions in 1α,25(OH)$_2$D$_3$-mediated induction of 24,25(OH)$_2$D$_3$ formation was the result of diminished up-regulation of CYP24A1 protein levels. Treatment of PTECs in the PT-MPS with 500 nM 1α,25(OH)$_2$D$_3$ resulted in apparently increased fluorescent signal for CYP24A1 protein compared to the vehicle control. This inductive effect was observed to be partially reversible with RAP co-administration (Figure 5.9).

5.4.7 1α,25(OH)$_2$D$_3$ Suppresses Megalin Gene Expression

Having established a role for the megalin in the modulation of intracellular levels of 1α,25(OH)$_2$D$_3$, we proceeded to explore the possible existence of a physiological feedback loop for the compensatory regulation megalin gene expression by 1α,25(OH)$_2$D$_3$. As shown in Figure 5.10A, expression of *megalin* and *CYP27B1* mRNA was suppressed in a roughly dose-dependent manner by 1α,25(OH)$_2$D$_3$.

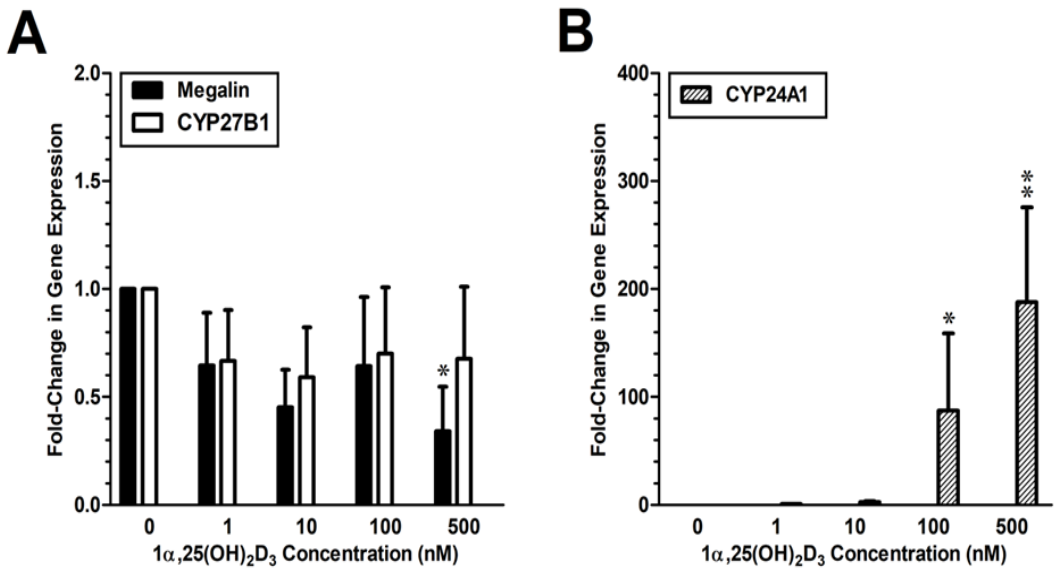

Figure 5.10. Comparative effects of 1α,25(OH)$_2$D$_3$ on *megalin*, *CYP24A1* and *CYP27B1* gene expression in PTECs. (A) Expression of both *megalin* and *CYP27B1* mRNA expression was suppressed in a roughly dose-dependent manner by 1α,25(OH)$_2$D$_3$. The apparent suppression was statistically significant only for *megalin* and only at the 500 nM dose. **(B)** Upregulation of the VDR-responsive "inductive" control gene (*CYP24A1*) was observed at both the 100 nM and 500 nM doses of 1α,25(OH)$_2$D$_3$. Levels of *CYP24A1* RNA were below the limit of quantification in the vehicle control group so the group was omitted from the statistical analysis. All gene expression data was standardized to GAPDH. *Statistically significant, $p < 0.05$. **Very statistically significant, $p < 0.01$.

However, a 1-way ANOVA revealed this suppression was statistically significant only for megalin. Post-hoc paired ratio t-tests revealed a statistically significant difference between megalin gene expression between the vehicle control and 1α,25(OH)$_2$D$_3$ only at

the highest (500 nM) dose. Up-regulation of the VDR-responsive "inductive" control gene (*CYP24A1*) was also significant, as determined by 1-way ANOVA. Post-hoc paired ratio t-tests displayed significantly different mRNA expression between the 1 nM $1\alpha,25(OH)_2D_3$ dose and both the 100 nM and 500 nM doses of $1\alpha,25(OH)_2D_3$ (Figure 5.10B).

5.5 Discussion

Since the time of the original knockout mouse studies, follow-up experiments evaluating the role of megalin in humans have been lacking. The recent development of the 3-dimensional PT-MPS has allowed us to reconstitute many of the *in vivo* physiologic processes of the proximal tubule epithelium in an *ex vivo* setting.[40] Recent observations of the effects of fluid sheer stress on promoting endocytosis and cellular polarization suggest an advantage to studying endocytotic processes in perfusion-based platforms such as the PT-MPS.[110, 152] The design of the PT-MPS permits the exposure of ligands of interest selectively to the apical cell surfaces and thus facilitates the functional characterization of megalin, a protein that is primarily localized to the apical membrane of PTECs.[153] Our observations of reduced uptake of $25OHD_3$ upon megalin inhibition confirm in a more human system, previous findings from the murine megalin knockout model.[140, 154] Furthermore, we observed the novel finding that megalin inhibition also reduced the VDR-dependent $1\alpha,25(OH)_2D_3$-mediated induction of CYP24A1 24-hydroxylation activity and protein expression. This finding is not surprising given that $1\alpha,25(OH)_2D_3$ is also tightly bound to DBP,[138] and that megalin-mediated uptake of protein-bound $1\alpha,25(OH)_2D_3$ may permit PTECs to better sense and respond to changes

in circulating concentrations of this bioactive hormone. Interestingly, the effects of megalin inhibition on 1α,25$(OH)_2D_3$ hormonal activity manifested predominantly as a reduction in the E_{max} for CYP24A1 induction. While RAP is a well-established competitive inhibitor of megalin,[145-147] there are a number of distinct RAP binding sites present on the large megalin protein and some evidence suggesting a non-competitive component to the RAP-mediated inhibition of certain substrates.[146, 155] Our results suggest that the RAP-mediated inhibition of the megalin-dependent uptake of DBP may proceed partially via a non-competitive mechanism. Alternatively, the RAP-mediated reduction in the E_{max} may be the result of megalin inhibition interfering with the intracellular trafficking pathways by which endocytosed megalin transfers DBP-bound 1α,25$(OH)_2D_3$ to intracellular vitamin D binding proteins (IDBPs) required to achieve maximal induction of CYP24A1. Members of the heat shock protein family, including IDBP-1 and IDBP-3, have been shown to be capable of interacting directly with megalin's cytosolic domain and are capable of binding both 25OHD_3 and 1α,25$(OH)_2D_3$.[156] In particular, IDBP-1 has been shown to bind 1α,25$(OH)_2D_3$ (K_d ~ 100 nM) with a high capacity and to translocate to the nucleus where it can facilitate the delivery of bound 1α,25$(OH)_2D_3$ to VDR.[157-159] Selective overexpression of IDBP-1 in non-human primate kidney cells has also been demonstrated to enhance the effectiveness 1α,25$(OH)_2D_3$-mediated induction of CYP24A1 gene expression.[157, 158]

Surprisingly, while the ability of 1α,25$(OH)_2D_3$ to induce the 24-hydroxylation of 25OHD_3 in the PT-MPS was reduced with RAP co-administration, the inhibitor did not independently alter the rate of 24,25$(OH)_2D_3$ formation from 25OHD_3 in PTECs. This occurred despite the apparent reduction in megalin-mediated endocytosis of DBP-bound

$25OHD_3$, as evidenced by the RAP-dependent reduction $25OHD_3$ disappearance rate from the PT-MPS perfusion media. This suggests one or more of the participants (e.g. IDBPs) governing the intracellular couriering of $25OHD_3$ to mitochondrial P450s may be saturated under our experimental conditions and that production of the majority of $24,25(OH)_2D_3$ formed in the cells may be from passively-partitioned unbound $25OHD_3$.

Supporting this explanation is the fact that a number of IDBPs have been identified to possess a selectively high affinity for $25OHD_3$ (K_d ~ 0.5 to 2.2 nM) and, as such, may be saturated at the relatively high concentrations of $25OHD_3$ administered in our experiments.[159] Furthermore, some of these proteins have even been demonstrated to translocate bound $25OHD_3$ to the mitochondria and participate in protein-protein interactions with vitamin D-metabolizing mitochondrial P450s.[157] It is important to note a critical assumption underlying this potential explanation is that DBP-bound $25OHD_3$ that is unable to be transferred to the saturated IDBPs would have to be unable to substantially access CYP24A1. Such an instance where this might occur would be if endocytosed DBPs transcytosed, rather than destined for lysosomal protein catabolism that could liberate $25OHD_3$ into the cytosol (See Figure 5.11). While there is evidence to suggest DBP is catabolized in the kidney, the extent of catabolism is unknown.[53, 160] Furthermore, other megalin substrates, such as albumin and retinol binding protein have been shown to be subject to extensive transcytosis.[22, 161]

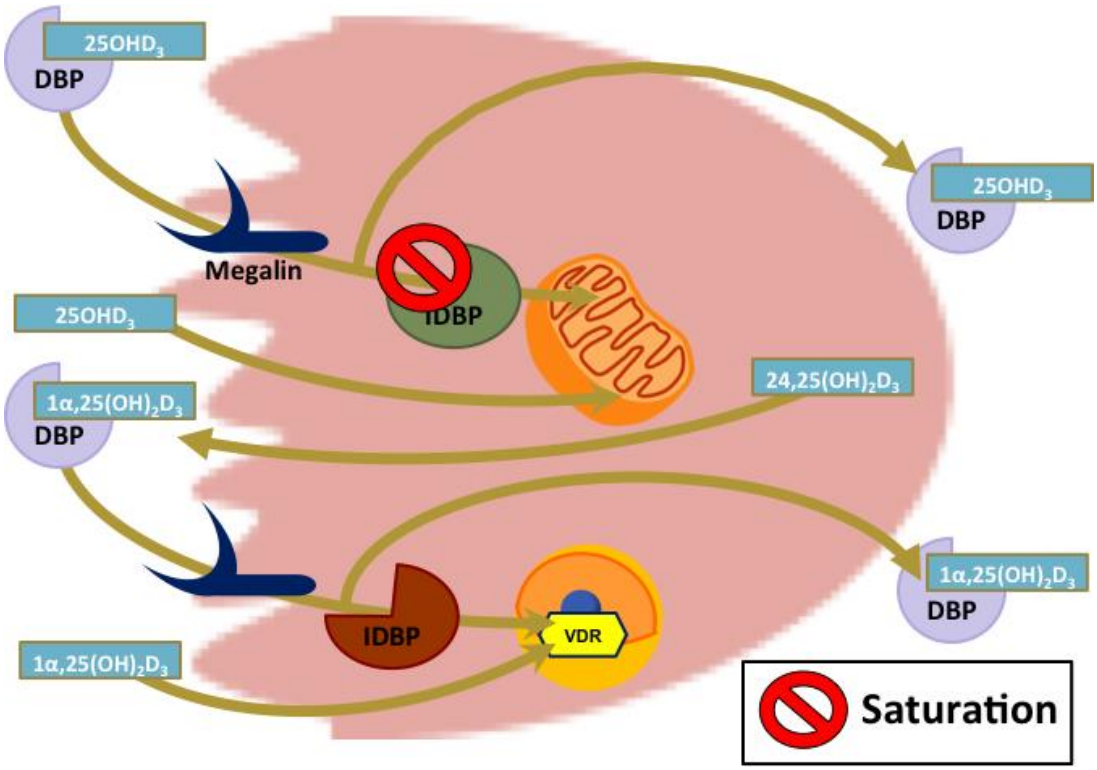

Figure 5.11. Hypothesis of saturation of 25OHD$_3$-binding but not 1α,25(OH)$_2$D$_3$-binding IDBP(s) under experimental conditions. The intracellular IDBPs that bind 25OHD$_3$ may be saturated at the super-physiological concentrations of 25OHD3 that are required in the experiments. As such, the majority of 24,25(OH)$_2$D$_3$ formed in the cells may be from passively-partitioned unbound 25OHD$_3$. However, DBP-bound 25OHD$_3$ that is unable to be transferred to the saturated IDBP(s) would have to be unable to substantially access CYP24A1. Such an instance where this might occur would be if endocytosed DBPs transcytosed, rather than destined for lysosomal protein catabolism that could liberate 25OHD$_3$ into the cytosol.

Taken together, these findings suggested a complex interplay between DBP levels, megalin-mediated uptake, vitamin D bioactivation and the 1α,25(OH)$_2$D$_3$–mediated induction of its own metabolic inactivation. As such, it is conceivable that 1α,25(OH)$_2$D$_3$ participates in the feedback regulation of megalin, thereby regulating its own metabolic formation. Hereto, the body of literature evaluating the role of 1α,25(OH)$_2$D$_3$ in megalin regulation has consisted of a sole study in immortalized rat proximal tubule epithelial cells.[63] That study concluded that 1α,25(OH)$_2$D$_3$ induces the

expression of megalin in the proximal tubule.[63] Despite the paucity of data, the findings of this singular study have repeatedly served as the basis for a "vicious cycle" hypothesis.[141-143] Essentially, this hypothesis states that decreases in renal vitamin D bioactivation, such as in CKD, can lead to reductions in renal megalin expression. This in turn would theoretically reduce vitamin D uptake and bioactivation, resulting in a cycle of progressively worsening vitamin D deficiency. Our findings run at odds with this idea and instead favor a hypothesis of compensatory reaction, whereby PTECs compensate for diminishing renal vitamin D bioactivation by increasing megalin and its reabsorptive uptake of DBP-bound $25OHD_3$ into the proximal tubule epithelium (Figure 5.12). Compensatory "negative" feedback loops have consistently characterized the physiological regulation of systemic vitamin D homeostasis (e.g. induction of CYP24A1 and CYP27B1 by $1\alpha,25(OH)_2D_3$ and PTH respectively).[42, 55, 162] Our findings are more in line with this overarching theme of compensatory regulation and may even shed some light on published results that previously seemed anomalous, including the dose-dependent down-regulation of megalin gene expression in LLC-PK1 cells exposed to lithocholic acid, an established VDR agonist.[163]

In summary, our findings describe megalin as a protein intimately woven into the complex web of physiological mechanisms regulating mineral homeostasis by promoting the uptake of $25OHD_3$ and $1\alpha,25(OH)_2D_3$ into human PTECs. Moreover, enhanced intracellular availability of $1\alpha,25(OH)_2D_3$ results in a down-regulation of PTEC megalin expression, providing negative feedback control of $1\alpha,25(OH)_2D_3$-mediated genomic effects. Further elucidation of aspects of this regulatory process may provide a better understanding of renal physiology and possibly reveal novel therapeutic targets for CKD.

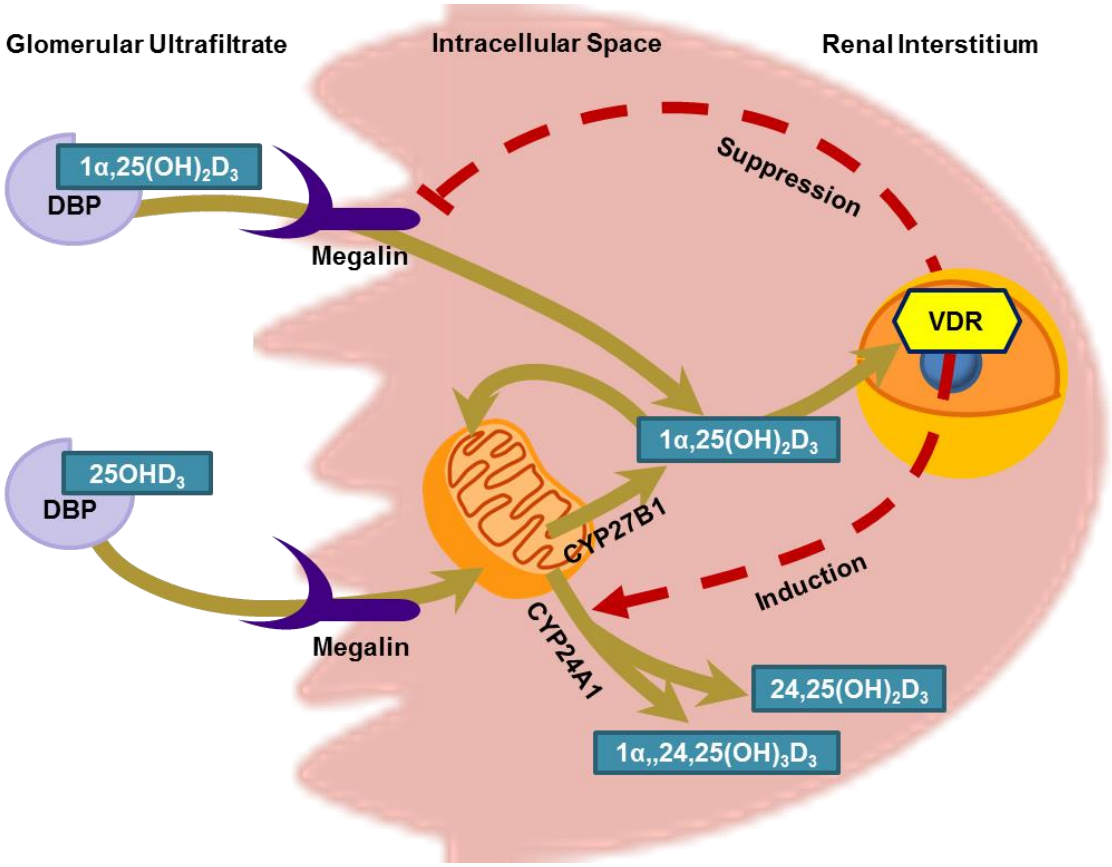

Figure 5.12. Role of megalin in the maintenance of renal vitamin D metabolite homeostasis. In PTECs, apically-localized megalin reclaims DBP-bound vitamin D metabolites from the glomerular ultra-filtrate. Resorbed $25OHD_3$ is then shuttled to the mitochondria for either CYP24A1-mediated inactivation or CYP27B1-mediated bioactivation. Intracellular $1\alpha,25(OH)_2D_3$, whether generated within the PTECs mitochondria or resorbed directly from the tubular lumen, can then undergo metabolic inactivation, enter systemic circulation to mediate endocrine effects or exert VDR-dependent intracrine effects within the PTECs. Intracrine effects include the compensatory upregulation of *CYP24A1* and the suppression *megalin* gene transcription.

6 Conclusions

When I the first joined the lab of Dr. Kenneth Thummel in the summer of 2012, I was assigned to characterize the drug-drug interaction between the 1st generation hepatitis C protease inhibitor, telaprevir, and the immunosuppressive drug, tacrolimus. Telaprevir, like most clinically administered protease inhibitors, is a potent inhibitor of Cytochrome P450 3A (CYP3A) so the presence of an interaction with tacrolimus, a drug exclusively metabolized by CYP3A, was not surprising.[68, 164] However, the sheer magnitude of the interaction, a nearly 70-fold increase in tacrolimus exposure,[67] raised many questions relating to the underlying mechanisms. The proposed explanation at the time, outlined by Vertex Pharmaceuticals in the telaprevir NDA, was that telaprevir was a time-dependent irreversible inhibitor of CYP3A.[68] Under the co-mentorship of Dr. Danny Shen, I set out in good faith to repeat the time-dependent inhibition studies originally conducted by Vertex. Our efforts are detailed in Chapter 2 and were also published in the *Journal of Pharmacy and Pharmaceutical Sciences*.[165] While time-dependent inhibition of CYP3A was observed in human liver microsomes, it was surprisingly completely reversible for the archetypical CYP3A probe substrate, midazolam, and partially reversible in the case of tacrolimus. Similar observations of reversible time-dependent CYP3A inhibition were also made by others relating to another 1st generation hepatitis C protease inhibitor, boceprevir.[82] Notably, these observations with boceprevir were accompanied by an absence of observable non-heme associated binding in radiolabeled studies.[82] With this in mind, we became interested in exploring whether the formation of inhibitory metabolites could explain the profound increases in tacrolimus exposure or even the relatively more moderate increases in midazolam exposure seen *in vivo*.[67, 68, 73]

Vertex had already characterized the major circulating metabolite of telaprevir, VRT-127394, and determined it to be a competitive inhibitor of CYP3A.[68] Relying on the *in vitro* competitive inhibition parameters supplied by Vertex for both telaprevir and VRT-127394, I employed classic static pharmacokinetic modeling approaches to account for inhibitor concentrations in the hepatic portal vein and intestinal villi.

Nevertheless, even when accounting for the presence of the major inhibitory metabolite, competitive inhibition of CYP3A alone could not explain the magnitude of the drug-drug interaction. A further theoretical exercise where I assumed entirely abolished first-pass metabolism was still unable to achieve the observed reductions in clearance for either midazolam or tacrolimus, even when systemic steady-state concentrations of the inhibitor were assumed to be at the upper bound of their 95% confidence interval. The persistent under-prediction of the static modeling under these extreme conditions of first-pass abolition suggested that further modeling of competitive inhibition of CYP3A with more advanced dynamic modeling methods (e.g. SimCyp Simulator), held little promise for fully predicting the magnitude of these drug-drug interactions. We began to suspect that a number of complex phenomena such as telaprevir-mediated inhibition of tacrolimus own inhibitory metabolites, interference with multiple "first-pass" extractions resulting from enterohepatic recycling, and inhibition of synergistic enzyme-transporter interplay between P-gp and CYP3A in intestinal lumen or hepatic bile canaliculi could be the cause of the observed drug-drug interaction. The human liver microsomal incubations and Caco-2 permeability assays that Vertex had relied upon were inadequate to test these difficult mechanistic hypotheses. This prompted us to look into alternative *in vitro* models that were capable of addressing these questions.

Around this time, researchers at the University of Washington Department of Pharmaceutics and the Kidney Research Institute were collaborating in a multi-center initiative to bioengineer flow-directed 3-dimensional microphysiological models of human organs. Our group was particularly focused on developing a model of the renal proximal tubule, but there was considerable interest in the simultaneous development of models for other organs that govern drug disposition such as the liver and small intestine. Promising initial results with the kidney proximal tubule module prompted our group to begin the development of a small intestinal module. Candidate cells lines and primary human fetal small intestinal epithelial cells (fSIECs) were first evaluated in traditional 2-dimensional Transwell® culture for their suitability in regards to barrier integrity and CYP3A expression. The results of these studies are described in Chapter 3 and were published in the journal *Drug Metabolism and Disposition*.[33] Unfortunately, the crucial properties of measurable CYP3A activity, tight junction integrity and responsiveness to prototypical inducers of CYP3A were not completely present in any of the cell lines/sources when cultured in Transwell® inserts.

Given the success of incorporating primary proximal tubule epithelial cells in the renal proximal tubule module, we decided to evaluate whether conditions of fluid sheer stress in 3-dimensional culture could restore *in vivo*-like phenotype in primary human fSIECs. While we obtained intriguing findings related to structural biology, our ability to assess the restoration of CYP3A activity was hindered by non-specific binding of our substrates of interest, midazolam and tacrolimus, to the polydimethylsiloxane (PDMS) components of the platform. Similar problems were also encountered when we administered midazolam to the liver module that was also under development. As a

material, PDMS has a number of favorable properties that make it well suited for use in microphysiological platforms. Its malleability makes it ideal for microfabrication, its transparency is conducive to microscopy and its gas permeability permits adequate cell oxygenation.[166] As such, a suitable alternative PDMS was, and still remains, elusive. As an alternative means to reduce the adsorption of lipophilic substrates and their metabolites, we began looking into the use of plasma carrier proteins to compete with PDMS surfaces for the compounds of interest. An opportunity arose to test such a method in the kidney proximal tubule model, which then could be adapted for use in the intestinal and liver modules.

The kidney proximal tubule is responsible for secreting relatively polar organic anions and cations.[3] As such, the adsorption of many of the compounds tested in the kidney module to its PDMS components was relatively negligible. However, as part of the evaluation of the proximal tubule microphysiological system (PT-MPS), there was a need to demonstrate functionality in regards to vitamin D bioactivation. The renal proximal tubule is the principal site for the bioactivation of vitamin D, a hormone critical for the maintenance of calcium and phosphate homeostasis.[42] Vitamin D and its metabolites are highly lipophilic secosteroids and problems of non-specific binding in the PT-MPS were immediately encountered.[167, 168] In order to recover vitamin D metabolites from PT-MPS, we began supplementing the perfusion media with fetal bovine serum (FBS). The addition of FBS proved to be an adequate but imperfect solution to demonstrate that the PT-MPS could generate the both the bioactive and major inactive metabolites, $1\alpha,25(OH)_2D_3$ and $24,25(OH)_2D_3$ respectively, from the prohormone, $25OHD_3$.[40] Using FBS as source of carrier proteins, we were also able to

establish that 1α,25$(OH)_2D_3$ was capable of inducing the metabolic inactivation of 25OHD_3 to 24,25$(OH)_2D_3$, a well-established form of negative feedback regulation *in vivo*.[40] These and additional findings related to the *ex vivo* recapitulation of other aspects of human renal proximal tubular physiology are described in Chapter 4 and also in a publication in *Kidney International* which I co-first authored with Alenka Chapron and Elijah Weber under the direction of Dr. Edward Kelly and Dr. Jonathan Himmelfarb.[40]

Because vitamin D metabolites circulate tightly bound their carrier protein, vitamin D binding protein (DBP),[137, 138] we began to validate the use of purified DBP as a carrier protein in the perfusion media. During this validation process we made an unexpected discovery; the maximum achievable induction of 24,25$(OH)_2D_3$ formation by 1α,25$(OH)_2D_3$ was approximately 10-fold greater for DBP than FBS. This suggested that DBP played a critical role in the delivery of 1α,25$(OH)_2D_3$ to the vitamin D receptor (VDR). We immediately suspected megalin, an endocytotic receptor expressed in the renal proximal tubular brush border, played a role in this phenomenon. This was because megalin had previously been shown to reclaim DBP-bound 25OHD_3 from the glomerular ultrafiltrate in mice.[139] Our preliminary data represented the first time megalin-mediated endocytosis of a DBP-bound vitamin D metabolite was demonstrated in a human cell-derived model of the renal proximal tubule. Furthermore, megalin-mediated uptake of the bioactive hormone, 1α,25$(OH)_2D_3$, had not been previously demonstrated in any species and was not hypothesized in any reviews on the subject of renal vitamin D disposition. Follow-up experiments of more controlled nature, incorporating the use of a specific megalin inhibitor, were conducted in the PT-MPS. They demonstrated that

interference with megalin-mediated endocytosis of DBP-bound 1α,25$(OH)_2D_3$ could modulate the hormone's VDR-dependent activity. Additional experiments also confirmed that the previous findings of megalin-mediated uptake of 25OHD_3 in the murine knockout models also applied to humans.

While these megalin-mediated uptake studies were being conducted, we were also in the midst of running screens with an array of nuclear receptor ligands in order to characterize the effects of the various regulatory pathways on the gene expression of drug transporters in 2-dimensional cultures of renal proximal tubule epithelial cells. Because of the intriguing findings with megalin, we decided to include it as a target in the screening. Interestingly, 1α,25$(OH)_2D_3$ was shown to have an effect on megalin expression. Further investigation into the literature provided little information on 1α,25$(OH)_2D_3$-mediated regulation of megalin gene expression. The only study that we could find used immortalized rat proximal tubule epithelial cells and surprisingly reported an opposite effect, with 1α,25$(OH)_2D_3$ inducing megalin gene expression.[63] Discrepancies between different models such as rodent versus human or immortalized versus primary cells are not uncommon.[25, 33] However, I was surprised to find that the earlier rat cell data had been repeatedly used as the sole basis for a provocative hypothesis for chronic kidney disease-induced vitamin D deficiency that invoked the participation of megalin in 1α,25$(OH)_2D_3$-dependent positive feedback loop.[141-143] Given the tenuous applicability to humans and the extensive citation history of the data from the rat cell model, we believe our findings (detailed in Chapter 5) regarding megalin's regulation by and transport of 1α,25$(OH)_2D_3$ are poised to considerably alter

the way in which megalin's role in renal disposition of vitamin D metabolites is understood.

Within the time frame of my dissertation research, circumstances did not favor a return to the original research questions that set me on my circuitous path. Telaprevir was eventually pulled from the market by its manufacturer and replaced by a plethora of newer direct acting antivirals with increased efficacy, safer adverse effect profiles and reduced potential to elicit drug-drug interactions.[169] We may never know what mechanisms precipitated the profound drug-drug interactions between telaprevir and tacrolimus. Without an understanding of these underlying mechanisms, it is possible that they may resurface in drugs that are yet to be developed. To prevent this from happening, it is essential to refine *in vitro* models of the human intestine and liver to accurately and holistically reflect the complexities of *in viv*o physiology. I have had the pleasure of assisting Dr. Shih-Yu Chang and her advisor, Dr. Dave Eaton, in the refinement of their CYP3A-competant model of the human liver.[39] Recent successes in integrating the liver microphysiological model with our kidney proximal tubule model highlight its potential to operate as part of a multi-organ system.[170] Further integration with a fully functional intestinal model may shed light on poorly explained but clinically significant drug-drug interactions. Unfortunately for our efforts on the intestinal microphysiological model, the commercial supplier of the primary human fSIECs used in our preliminary experiments no longer provides the cells. However, the development of an *in vitro* model for the simultaneous assessment of absorption and CYP3A-mediated metabolism is of such a wide-reaching importance that research will undoubtedly continue where there is funding and access to primary small intestinal tissue.

References

1. Hisaka A, Ohno Y, Yamamoto T, Suzuki H. Theoretical considerations on quantitative prediction of drug-drug interactions. Drug metabolism and pharmacokinetics. 2010;25(1):48-61.
2. Rowland M, Benet LZ, Graham GG. Clearance concepts in pharmacokinetics. Journal of pharmacokinetics and biopharmaceutics. 1973;1(2):123-36.
3. Rowland M, Tozer T. Clinical Pharmacokinetics and Pharmacodynamics Concepts and Applications. 4th ed: Lippincott Williams and Wilkins; 2011.
4. Guyton A, Hall J. Textbook of Medical Physiology. 11th ed: Elsevier Saunders; 2006.
5. Giacomini KM, Huang SM, Tweedie DJ, Benet LZ, Brouwer KL, Chu X, et al. Membrane transporters in drug development. Nature reviews Drug discovery. 2010;9(3):215-36.
6. Christians U. Transport proteins and intestinal metabolism: P-glycoprotein and cytochrome P4503A. Therapeutic drug monitoring. 2004;26(2):104-6.
7. Kato M. Intestinal first-pass metabolism of CYP3A4 substrates. Drug metabolism and pharmacokinetics. 2008;23(2):87-94.
8. Paine MF, Hart HL, Ludington SS, Haining RL, Rettie AE, Zeldin DC. The human intestinal cytochrome P450 "pie". Drug metabolism and disposition: the biological fate of chemicals. 2006;34(5):880-6.
9. Felmlee DJ, Grun D, Baumert TF. Zooming in on Liver Zonation. Hepatology (Baltimore, Md). 2017.
10. Liu L, Pang KS. An integrated approach to model hepatic drug clearance. European journal of pharmaceutical sciences : official journal of the European Federation for Pharmaceutical Sciences. 2006;29(3-4):215-30.
11. Westlind A, Lofberg L, Tindberg N, Andersson TB, Ingelman-Sundberg M. Interindividual differences in hepatic expression of CYP3A4: relationship to genetic polymorphism in the 5'-upstream regulatory region. Biochemical and biophysical research communications. 1999;259(1):201-5.
12. Guengerich FP. Cytochrome P-450 3A4: regulation and role in drug metabolism. Annual review of pharmacology and toxicology. 1999;39:1-17.
13. Klein K, Zanger UM. Pharmacogenomics of Cytochrome P450 3A4: Recent Progress Toward the "Missing Heritability" Problem. Frontiers in genetics. 2013;4:12.
14. Taal M, Brenner B, Rector F. Brenner and Rector's the kidney. 9th ed: Elsevier Saunders; 1937-.
15. Vallon V, Platt KA, Cunard R, Schroth J, Whaley J, Thomson SC, et al. SGLT2 mediates glucose reabsorption in the early proximal tubule. Journal of the American Society of Nephrology : JASN. 2011;22(1):104-12.
16. Liu JJ, Lee T, DeFronzo RA. Why Do SGLT2 inhibitors inhibit only 30-50% of renal glucose reabsorption in humans? Diabetes. 2012;61(9):2199-204.
17. Schlondorff D, Wyatt CM, Campbell KN. Revisiting the determinants of the glomerular filtration barrier: what goes round must come round. Kidney international. 2017;92(3):533-6.

18. Eshbach ML, Weisz OA. Receptor-Mediated Endocytosis in the Proximal Tubule. Annual review of physiology. 2017;79:425-48.
19. Marzolo MP, Farfan P. New insights into the roles of megalin/LRP2 and the regulation of its functional expression. Biological research. 2011;44(1):89-105.
20. Czekay RP, Orlando RA, Woodward L, Lundstrom M, Farquhar MG. Endocytic trafficking of megalin/RAP complexes: dissociation of the complexes in late endosomes. Molecular biology of the cell. 1997;8(3):517-32.
21. Jovic M, Sharma M, Rahajeng J, Caplan S. The early endosome: a busy sorting station for proteins at the crossroads. Histology and histopathology. 2010;25(1):99-112.
22. Tenten V, Menzel S, Kunter U, Sicking EM, van Roeyen CR, Sanden SK, et al. Albumin is recycled from the primary urine by tubular transcytosis. Journal of the American Society of Nephrology : JASN. 2013;24(12):1966-80.
23. Mettetal JT. Model-Informed Reverse and Forward Translation of Safety Risks in Drug Development. Clinical pharmacology and therapeutics. 2017.
24. Administration USFaD. In Vitro Metabolism and Transporter-Mediated Drug-Drug Interaction Studies Guidance for Industry 2017 [cited 2018 January 9]. Available from: https://http://www.fda.gov/downloads/Drugs/GuidanceComplianceRegulatoryInformation/Guidances/UCM581965.pdf.
25. Jiang XL, Gonzalez FJ, Yu AM. Drug-metabolizing enzyme, transporter, and nuclear receptor genetically modified mouse models. Drug metabolism reviews. 2011;43(1):27-40.
26. Chang SY, Weber EJ, Ness KV, Eaton DL, Kelly EJ. Liver and Kidney on Chips: Microphysiological Models to Understand Transporter Function. Clinical pharmacology and therapeutics. 2016;100(5):464-78.
27. Pathak SM, Ruff A, Kostewicz ES, Patel N, Turner DB, Jamei M. Model-Based Analysis of Biopharmaceutic Experiments To Improve Mechanistic Oral Absorption Modeling: An Integrated in Vitro in Vivo Extrapolation Perspective Using Ketoconazole as a Model Drug. Molecular pharmaceutics. 2017;14(12):4305-20.
28. Johnson TN, Rostami-Hodjegan A. Resurgence in the use of physiologically based pharmacokinetic models in pediatric clinical pharmacology: parallel shift in incorporating the knowledge of biological elements and increased applicability to drug development and clinical practice. Paediatric anaesthesia. 2011;21(3):291-301.
29. Zhuang X, Lu C. PBPK modeling and simulation in drug research and development. Acta pharmaceutica Sinica B. 2016;6(5):430-40.
30. Gill KL, Gertz M, Houston JB, Galetin A. Application of a physiologically based pharmacokinetic model to assess propofol hepatic and renal glucuronidation in isolation: utility of in vitro and in vivo data. Drug metabolism and disposition: the biological fate of chemicals. 2013;41(4):744-53.
31. Jones HM, Gardner IB, Watson KJ. Modelling and PBPK simulation in drug discovery. The AAPS journal. 2009;11(1):155-66.
32. Sjoberg A, Lutz M, Tannergren C, Wingolf C, Borde A, Ungell AL. Comprehensive study on regional human intestinal permeability and prediction of fraction absorbed of drugs using the Ussing chamber technique. European journal of

pharmaceutical sciences : official journal of the European Federation for Pharmaceutical Sciences. 2013;48(1-2):166-80.
33. Yamaura Y, Chapron BD, Wang Z, Himmelfarb J, Thummel KE. Functional Comparison of Human Colonic Carcinoma Cell Lines and Primary Small Intestinal Epithelial Cells for Investigations of Intestinal Drug Permeability and First-Pass Metabolism. Drug metabolism and disposition: the biological fate of chemicals. 2016;44(3):329-35.
34. Cummins CL, Jacobsen W, Benet LZ. Unmasking the dynamic interplay between intestinal P-glycoprotein and CYP3A4. The Journal of pharmacology and experimental therapeutics. 2002;300(3):1036-45.
35. Schmiedlin-Ren P, Thummel KE, Fisher JM, Paine MF, Watkins PB. Induction of CYP3A4 by 1 alpha,25-dihydroxyvitamin D3 is human cell line-specific and is unlikely to involve pregnane X receptor. Drug metabolism and disposition: the biological fate of chemicals. 2001;29(11):1446-53.
36. Prantil-Baun R, Novak R, Das D, Somayaji MR, Przekwas A, Ingber DE. Physiologically Based Pharmacokinetic and Pharmacodynamic Analysis Enabled by Microfluidically Linked Organs-on-Chips. Annual review of pharmacology and toxicology. 2018;58:37-64.
37. Kelly EJ, Wang Z, Voellinger JL, Yeung CK, Shen DD, Thummel KE, et al. Innovations in preclinical biology: ex vivo engineering of a human kidney tissue microperfusion system. Stem cell research & therapy. 2013;4 Suppl 1:S17.
38. Bauer S, Wennberg Huldt C, Kanebratt KP, Durieux I, Gunne D, Andersson S. Functional coupling of human pancreatic islets and liver spheroids on-a-chip: Towards a novel human ex vivo type 2 diabetes model. 2017;7(1):14620.
39. Chang SY, Voellinger JL, Van Ness KP, Chapron B, Shaffer RM, Neumann T, et al. Characterization of rat or human hepatocytes cultured in microphysiological systems (MPS) to identify hepatotoxicity. Toxicology in vitro : an international journal published in association with BIBRA. 2017;40:170-83.
40. Weber EJ, Chapron A, Chapron BD, Voellinger JL, Lidberg KA, Yeung CK, et al. Development of a microphysiological model of human kidney proximal tubule function. Kidney international. 2016;90(3):627-37.
41. Kurokawa YK, Yin RT, Shang MR, Shirure VS, Moya ML, George SC. Human Induced Pluripotent Stem Cell-Derived Endothelial Cells for Three-Dimensional Microphysiological Systems. Tissue engineering Part C, Methods. 2017;23(8):474-84.
42. Dusso AS, Brown AJ, Slatopolsky E. Vitamin D. American journal of physiology Renal physiology. 2005;289(1):F8-28.
43. Jaaskelainen T, Knekt P, Suvisaari J, Mannisto S, Partonen T, Saaksjarvi K, et al. Higher serum 25-hydroxyvitamin D concentrations are related to a reduced risk of depression. The British journal of nutrition. 2015;113(9):1418-26.
44. Lugg ST, Howells PA, Thickett DR. Optimal Vitamin D Supplementation Levels for Cardiovascular Disease Protection. Disease markers. 2015;2015:864370.
45. Blomhoff R, Helgerud P, Dueland S, Berg T, Pedersen JI, Norum KR, et al. Lymphatic absorption and transport of retinol and vitamin D-3 from rat intestine. Evidence for different pathways. Biochimica et biophysica acta. 1984;772(2):109-16.

46. Jones G. Pharmacokinetics of vitamin D toxicity. The American journal of clinical nutrition. 2008;88(2):582s-6s.
47. Axelson M. 25-Hydroxyvitamin D3 3-sulphate is a major circulating form of vitamin D in man. FEBS letters. 1985;191(2):171-5.
48. Wang Z, Wong T, Hashizume T, Dickmann LZ, Scian M, Koszewski NJ, et al. Human UGT1A4 and UGT1A3 conjugate 25-hydroxyvitamin D3: metabolite structure, kinetics, inducibility, and interindividual variability. Endocrinology. 2014;155(6):2052-63.
49. Frese MA, Schulz S, Dierks T. Arylsulfatase G, a novel lysosomal sulfatase. The Journal of biological chemistry. 2008;283(17):11388-95.
50. Miki Y, Nakata T, Suzuki T, Darnel AD, Moriya T, Kaneko C, et al. Systemic distribution of steroid sulfatase and estrogen sulfotransferase in human adult and fetal tissues. The Journal of clinical endocrinology and metabolism. 2002;87(12):5760-8.
51. Wang TT, Tavera-Mendoza LE, Laperriere D, Libby E, MacLeod NB, Nagai Y, et al. Large-scale in silico and microarray-based identification of direct 1,25-dihydroxyvitamin D3 target genes. Molecular endocrinology (Baltimore, Md). 2005;19(11):2685-95.
52. Gao C, Bergagnini-Kolev MC, Liao MZ, Wang Z, Wong T, Calamia JC, et al. Simultaneous quantification of 25-hydroxyvitamin D3-3-sulfate and 25-hydroxyvitamin D3-3-glucuronide in human serum and plasma using liquid chromatography-tandem mass spectrometry coupled with DAPTAD-derivatization. Journal of chromatography B, Analytical technologies in the biomedical and life sciences. 2017;1060:158-65.
53. Dueland S, Blomhoff R, Pedersen JI. Uptake and degradation of vitamin D binding protein and vitamin D binding protein-actin complex in vivo in the rat. The Biochemical journal. 1990;267(3):721-5.
54. Mirkovic K, Doorenbos CR, Dam WA, Lambers Heerspink HJ, Slagman MC, Nauta FL, et al. Urinary vitamin D binding protein: a potential novel marker of renal interstitial inflammation and fibrosis. PloS one. 2013;8(2):e55887.
55. Jones G, Prosser DE, Kaufmann M. 25-Hydroxyvitamin D-24-hydroxylase (CYP24A1): its important role in the degradation of vitamin D. Archives of biochemistry and biophysics. 2012;523(1):9-18.
56. Prie D, Friedlander G. Reciprocal control of 1,25-dihydroxyvitamin D and FGF23 formation involving the FGF23/Klotho system. Clinical journal of the American Society of Nephrology : CJASN. 2010;5(9):1717-22.
57. Cheloha RW, Gellman SH, Vilardaga JP, Gardella TJ. PTH receptor-1 signalling-mechanistic insights and therapeutic prospects. Nature reviews Endocrinology. 2015.
58. Fan Y, Bi R, Densmore MJ, Sato T, Kobayashi T, Yuan Q, et al. Parathyroid hormone 1 receptor is essential to induce FGF23 production and maintain systemic mineral ion homeostasis. FASEB journal : official publication of the Federation of American Societies for Experimental Biology. 2015.
59. Alfadda TI, Saleh AM, Houillier P, Geibel JP. Calcium-sensing receptor 20 years later. American journal of physiology Cell physiology. 2014;307(3):C221-31.

60. Erkan E. Proteinuria and progression of glomerular diseases. Pediatric nephrology (Berlin, Germany). 2013;28(7):1049-58.
61. Gekle M, Knaus P, Nielsen R, Mildenberger S, Freudinger R, Wohlfarth V, et al. Transforming growth factor-beta1 reduces megalin- and cubilin-mediated endocytosis of albumin in proximal-tubule-derived opossum kidney cells. The Journal of physiology. 2003;552(Pt 2):471-81.
62. Vinge L, Lees GE, Nielsen R, Kashtan CE, Bahr A, Christensen EI. The effect of progressive glomerular disease on megalin-mediated endocytosis in the kidney. Nephrology, dialysis, transplantation : official publication of the European Dialysis and Transplant Association - European Renal Association. 2010;25(8):2458-67.
63. Liu W, Yu WR, Carling T, Juhlin C, Rastad J, Ridefelt P, et al. Regulation of gp330/megalin expression by vitamins A and D. European journal of clinical investigation. 1998;28(2):100-7.
64. Ghany MG, Nelson DR, Strader DB, Thomas DL, Seeff LB. An update on treatment of genotype 1 chronic hepatitis C virus infection: 2011 practice guideline by the American Association for the Study of Liver Diseases. Hepatology (Baltimore, Md). 2011;54(4):1433-44.
65. Manos MM, Shvachko VA, Murphy RC, Arduino JM, Shire NJ. Distribution of hepatitis C virus genotypes in a diverse US integrated health care population. Journal of medical virology. 2012;84(11):1744-50.
66. Talavera Pons S, Lamblin G, Boyer A, Sautou V, Abergel A. Drug interactions and protease inhibitors used in the treatment of hepatitis C: how to manage? European journal of clinical pharmacology. 2014;70(7):775-89.
67. Garg V, van Heeswijk R, Lee JE, Alves K, Nadkarni P, Luo X. Effect of telaprevir on the pharmacokinetics of cyclosporine and tacrolimus. Hepatology (Baltimore, Md). 2011;54(1):20-7.
68. Research. USFaDACfEa. Telaprevir Clinical Pharmacology and Biopharmaceutics Review(s) http://www.accessdata.fda.gov/drugsatfda_docs/nda/2011/201917Orig1s000ClinPharmR.pdf.
69. Oda K, Yamano K. Effect of telaprevir on the metabolism and hepatic uptake of tacrolimus (FK506). Biopharmaceutics & drug disposition. 2014;35(9):501-12.
70. Zheng S, Easterling TR, Umans JG, Miodovnik M, Calamia JC, Thummel KE, et al. Pharmacokinetics of tacrolimus during pregnancy. Therapeutic drug monitoring. 2012;34(6):660-70.
71. Galetin A, Gertz M, Houston JB. Potential role of intestinal first-pass metabolism in the prediction of drug-drug interactions. Expert opinion on drug metabolism & toxicology. 2008;4(7):909-22.
72. Obach RS, Walsky RL, Venkatakrishnan K, Gaman EA, Houston JB, Tremaine LM. The utility of in vitro cytochrome P450 inhibition data in the prediction of drug-drug interactions. The Journal of pharmacology and experimental therapeutics. 2006;316(1):336-48.
73. Garg V, Chandorkar G, Farmer HF, Smith F, Alves K, van Heeswijk RP. Effect of telaprevir on the pharmacokinetics of midazolam and digoxin. Journal of clinical pharmacology. 2012;52(10):1566-73.

74. Gertz M, Houston JB, Galetin A. Physiologically based pharmacokinetic modeling of intestinal first-pass metabolism of CYP3A substrates with high intestinal extraction. Drug metabolism and disposition: the biological fate of chemicals. 2011;39(9):1633-42.
75. Gorski JC, Jones DR, Haehner-Daniels BD, Hamman MA, O'Mara EM, Jr., Hall SD. The contribution of intestinal and hepatic CYP3A to the interaction between midazolam and clarithromycin. Clinical pharmacology and therapeutics. 1998;64(2):133-43.
76. Lu C, Hatsis P, Berg C, Lee FW, Balani SK. Prediction of pharmacokinetic drug-drug interactions using human hepatocyte suspension in plasma and cytochrome P450 phenotypic data. II. In vitro-in vivo correlation with ketoconazole. Drug metabolism and disposition: the biological fate of chemicals. 2008;36(7):1255-60.
77. Heizmann P, Ziegler WH. Excretion and metabolism of 14C-midazolam in humans following oral dosing. Arzneimittel-Forschung. 1981;31(12a):2220-3.
78. Yang J, Jamei M, Yeo KR, Tucker GT, Rostami-Hodjegan A. Prediction of intestinal first-pass drug metabolism. Current drug metabolism. 2007;8(7):676-84.
79. Dai Y, Hebert MF, Isoherranen N, Davis CL, Marsh C, Shen DD, et al. Effect of CYP3A5 polymorphism on tacrolimus metabolic clearance in vitro. Drug metabolism and disposition: the biological fate of chemicals. 2006;34(5):836-47.
80. Kamdem LK, Streit F, Zanger UM, Brockmoller J, Oellerich M, Armstrong VW, et al. Contribution of CYP3A5 to the in vitro hepatic clearance of tacrolimus. Clinical chemistry. 2005;51(8):1374-81.
81. Reckhow D. Chapter XXIII: Parametric Statistics UMASS College of Engineering2004 [September 24, 2015]. Available from: http://www.ecs.umass.edu/cee/reckhow/courses/572/572bk23/572BK23.html.
82. Chu X, Cai X, Cui D, Tang C, Ghosal A, Chan G, et al. In vitro assessment of drug-drug interaction potential of boceprevir associated with drug metabolizing enzymes and transporters. Drug metabolism and disposition: the biological fate of chemicals. 2013;41(3):668-81.
83. Lee JY, Lee SY, Oh SJ, Lee KH, Jung YS, Kim SK. Assessment of drug-drug interactions caused by metabolism-dependent cytochrome P450 inhibition. Chemico-biological interactions. 2012;198(1-3):49-56.
84. Wu CY, Benet LZ. Disposition of tacrolimus in isolated perfused rat liver: influence of troleandomycin, cyclosporine, and gg918. Drug metabolism and disposition: the biological fate of chemicals. 2003;31(11):1292-5.
85. Amundsen R, Asberg A, Ohm IK, Christensen H. Cyclosporine A- and tacrolimus-mediated inhibition of CYP3A4 and CYP3A5 in vitro. Drug metabolism and disposition: the biological fate of chemicals. 2012;40(4):655-61.
86. Artursson P, Karlsson J. Correlation between oral drug absorption in humans and apparent drug permeability coefficients in human intestinal epithelial (Caco-2) cells. Biochemical and biophysical research communications. 1991;175(3):880-5.
87. Yee S. In vitro permeability across Caco-2 cells (colonic) can predict in vivo (small intestinal) absorption in man--fact or myth. Pharmaceutical research. 1997;14(6):763-6.
88. Schmiedlin-Ren P, Thummel KE, Fisher JM, Paine MF, Lown KS, Watkins PB. Expression of enzymatically active CYP3A4 by Caco-2 cells grown on extracellular

matrix-coated permeable supports in the presence of 1alpha,25-dihydroxyvitamin D3. Molecular pharmacology. 1997;51(5):741-54.
89. Peters SA, Schroeder PE, Giri N, Dolgos H. Evaluation of the use of static and dynamic models to predict drug-drug interaction and its associated variability: impact on drug discovery and early development. Drug metabolism and disposition: the biological fate of chemicals. 2012;40(8):1495-507.
90. Brimer C, Dalton JT, Zhu Z, Schuetz J, Yasuda K, Vanin E, et al. Creation of polarized cells coexpressing CYP3A4, NADPH cytochrome P450 reductase and MDR1/P-glycoprotein. Pharmaceutical research. 2000;17(7):803-10.
91. Crespi CL, Fox L, Stocker P, Hu M, Steimel DT. Analysis of drug transport and metabolism in cell monolayer systems that have been modified by cytochrome P4503A4 cDNA-expression. European journal of pharmaceutical sciences : official journal of the European Federation for Pharmaceutical Sciences. 2000;12(1):63-8.
92. Fisher JM, Wrighton SA, Watkins PB, Schmiedlin-Ren P, Calamia JC, Shen DD, et al. First-pass midazolam metabolism catalyzed by 1alpha,25-dihydroxy vitamin D3-modified Caco-2 cell monolayers. The Journal of pharmacology and experimental therapeutics. 1999;289(2):1134-42.
93. Mouly SJ, Paine MF, Watkins PB. Contributions of CYP3A4, P-glycoprotein, and serum protein binding to the intestinal first-pass extraction of saquinavir. The Journal of pharmacology and experimental therapeutics. 2004;308(3):941-8.
94. Zheng XE, Wang Z, Liao MZ, Lin YS, Shuhart MC, Schuetz EG, et al. Human PXR-mediated induction of intestinal CYP3A4 attenuates 1alpha,25-dihydroxyvitamin D(3) function in human colon adenocarcinoma LS180 cells. Biochemical pharmacology. 2012;84(3):391-401.
95. Dharmsathaphorn K, McRoberts JA, Mandel KG, Tisdale LD, Masui H. A human colonic tumor cell line that maintains vectorial electrolyte transport. The American journal of physiology. 1984;246(2 Pt 1):G204-8.
96. Bourgine J, Billaut-Laden I, Happillon M, Lo-Guidice JM, Maunoury V, Imbenotte M, et al. Gene expression profiling of systems involved in the metabolism and the disposition of xenobiotics: comparison between human intestinal biopsy samples and colon cell lines. Drug metabolism and disposition: the biological fate of chemicals. 2012;40(4):694-705.
97. Juuti-Uusitalo KM, Kaukinen K, Maki M, Tuimala J, Kainulainen H. Gene expression in TGFbeta-induced epithelial cell differentiation in a three-dimensional intestinal epithelial cell differentiation model. BMC genomics. 2006;7:279.
98. Haslam IS, Jones K, Coleman T, Simmons NL. Rifampin and digoxin induction of MDR1 expression and function in human intestinal (T84) epithelial cells. British journal of pharmacology. 2008;154(1):246-55.
99. Kauffman AL, Gyurdieva AV, Mabus JR, Ferguson C, Yan Z, Hornby PJ. Alternative functional in vitro models of human intestinal epithelia. Frontiers in pharmacology. 2013;4:79.
100. Nakamura T, Sato T. Advancing Intestinal Organoid Technology Toward Regenerative Medicine. Cellular and molecular gastroenterology and hepatology. 2018;5(1):51-60.

101. Saxena K, Blutt SE, Ettayebi K, Zeng XL, Broughman JR, Crawford SE, et al. Human Intestinal Enteroids: a New Model To Study Human Rotavirus Infection, Host Restriction, and Pathophysiology. Journal of virology. 2015;90(1):43-56.
102. Johnson TN, Tanner MS, Taylor CJ, Tucker GT. Enterocytic CYP3A4 in a paediatric population: developmental changes and the effect of coeliac disease and cystic fibrosis. British journal of clinical pharmacology. 2001;51(5):451-60.
103. Takenaka T, Harada N, Kuze J, Chiba M, Iwao T, Matsunaga T. Human small intestinal epithelial cells differentiated from adult intestinal stem cells as a novel system for predicting oral drug absorption in humans. Drug metabolism and disposition: the biological fate of chemicals. 2014;42(11):1947-54.
104. Powell DW. Barrier function of epithelia. The American journal of physiology. 1981;241(4):G275-88.
105. Kirch W, Gorg KG. Clinical pharmacokinetics of atenolol--a review. European journal of drug metabolism and pharmacokinetics. 1982;7(2):81-91.
106. Jeon H, Jang IJ, Lee S, Ohashi K, Kotegawa T, Ieiri I, et al. Apple juice greatly reduces systemic exposure to atenolol. British journal of clinical pharmacology. 2013;75(1):172-9.
107. Vernetti L, Gough A, Baetz N, Blutt S, Broughman JR, Brown JA, et al. Functional Coupling of Human Microphysiology Systems: Intestine, Liver, Kidney Proximal Tubule, Blood-Brain Barrier and Skeletal Muscle. Scientific reports. 2017;7:42296.
108. Acara M, Carr EA, Jr., Terry EN. Probenecid inhibition of the renal excretion of dyphylline in chicken, rat and man. The Journal of pharmacy and pharmacology. 1987;39(7):526-30.
109. Horster M, Valtin H. ostnatal development of renal function: micropuncture and clearance studies in the dog. The Journal of clinical investigation. 1971;50(4):779-95.
110. Raghavan V, Rbaibi Y, Pastor-Soler NM, Carattino MD, Weisz OA. Shear stress-dependent regulation of apical endocytosis in renal proximal tubule cells mediated by primary cilia. Proceedings of the National Academy of Sciences of the United States of America. 2014;111(23):8506-11.
111. Sciancalepore AG, Sallustio F, Girardo S, Gioia Passione L, Camposeo A, Mele E, et al. A bioartificial renal tubule device embedding human renal stem/progenitor cells. PloS one. 2014;9(1):e87496.
112. Alpers CE, Hudkins KL, Pritzl P, Johnson RJ. Mechanisms of clearance of immune complexes from peritubular capillaries in the rat. The American journal of pathology. 1991;139(4):855-67.
113. Wang Z, Senn T, Kalhorn T, Zheng XE, Zheng S, Davis CL, et al. Simultaneous measurement of plasma vitamin D(3) metabolites, including 4beta,25-dihydroxyvitamin D(3), using liquid chromatography-tandem mass spectrometry. Analytical biochemistry. 2011;418(1):126-33.
114. Humes HD, MacKay SM, Funke AJ, Buffington DA. Tissue engineering of a bioartificial renal tubule assist device: in vitro transport and metabolic characteristics. Kidney international. 1999;55(6):2502-14.

115. Wickham S, West MB, Cook PF, Hanigan MH. Gamma-glutamyl compounds: substrate specificity of gamma-glutamyl transpeptidase enzymes. Analytical biochemistry. 2011;414(2):208-14.
116. Park JB. Flavonoids are potential inhibitors of glucose uptake in U937 cells. Biochemical and biophysical research communications. 1999;260(2):568-74.
117. Tourovskaia A, Fauver M, Kramer G, Simonson S, Neumann T. Tissue-engineered microenvironment systems for modeling human vasculature. Experimental biology and medicine (Maywood, NJ). 2014;239(9):1264-71.
118. DesRochers TM, Suter L, Roth A, Kaplan DL. Bioengineered 3D human kidney tissue, a platform for the determination of nephrotoxicity. PloS one. 2013;8(3):e59219.
119. Jang KJ, Mehr AP, Hamilton GA, McPartlin LA, Chung S, Suh KY, et al. Human kidney proximal tubule-on-a-chip for drug transport and nephrotoxicity assessment. Integrative biology : quantitative biosciences from nano to macro. 2013;5(9):1119-29.
120. Smith PL, Buffington DA, Humes HD. Kidney epithelial cells. Methods in enzymology. 2006;419:194-207.
121. Blackburn JG, Hazen-Martin DJ, Detrisac CJ, Sens DA. Electrophysiology and ultrastructure of cultured human proximal tubule cells. Kidney international. 1988;33(2):508-16.
122. Lash LH, Putt DA, Cai H. Membrane transport function in primary cultures of human proximal tubular cells. Toxicology. 2006;228(2-3):200-18.
123. Jansen J, De Napoli IE, Fedecostante M, Schophuizen CM, Chevtchik NV, Wilmer MJ, et al. Human proximal tubule epithelial cells cultured on hollow fibers: living membranes that actively transport organic cations. Scientific reports. 2015;5:16702.
124. Schophuizen CM, De Napoli IE, Jansen J, Teixeira S, Wilmer MJ, Hoenderop JG, et al. Development of a living membrane comprising a functional human renal proximal tubule cell monolayer on polyethersulfone polymeric membrane. Acta biomaterialia. 2015;14:22-32.
125. Sekiya S, Shimizu T, Yamato M, Okano T. Hormone supplying renal cell sheet in vivo produced by tissue engineering technology. BioResearch open access. 2013;2(1):12-9.
126. Maeshima A, Sakurai H, Nigam SK. Adult kidney tubular cell population showing phenotypic plasticity, tubulogenic capacity, and integration capability into developing kidney. Journal of the American Society of Nephrology : JASN. 2006;17(1):188-98.
127. Martinez E, Engel E, Planell JA, Samitier J. Effects of artificial micro- and nano-structured surfaces on cell behaviour. Annals of anatomy = Anatomischer Anzeiger : official organ of the Anatomische Gesellschaft. 2009;191(1):126-35.
128. Thery M. Micropatterning as a tool to decipher cell morphogenesis and functions. Journal of cell science. 2010;123(Pt 24):4201-13.
129. Discher DE, Janmey P, Wang YL. Tissue cells feel and respond to the stiffness of their substrate. Science (New York, NY). 2005;310(5751):1139-43.
130. Engler AJ, Sen S, Sweeney HL, Discher DE. Matrix elasticity directs stem cell lineage specification. Cell. 2006;126(4):677-89.

131. Maschmeyer I, Lorenz AK, Schimek K, Hasenberg T, Ramme AP, Hubner J, et al. A four-organ-chip for interconnected long-term co-culture of human intestine, liver, skin and kidney equivalents. Lab on a chip. 2015;15(12):2688-99.
132. Humes HD, Weitzel WF, Bartlett RH, Swaniker FC, Paganini EP, Luderer JR, et al. Initial clinical results of the bioartificial kidney containing human cells in ICU patients with acute renal failure. Kidney international. 2004;66(4):1578-88.
133. Ligresti G, Nagao RJ, Xue J, Choi YJ, Xu J, Ren S, et al. A Novel Three-Dimensional Human Peritubular Microvascular System. Journal of the American Society of Nephrology : JASN. 2016;27(8):2370-81.
134. Maiti A, Beckman MJ. Extracellular calcium is a direct effecter of VDR levels in proximal tubule epithelial cells that counter-balances effects of PTH on renal Vitamin D metabolism. The Journal of steroid biochemistry and molecular biology. 2007;103(3-5):504-8.
135. Perwad F, Zhang MY, Tenenhouse HS, Portale AA. Fibroblast growth factor 23 impairs phosphorus and vitamin D metabolism in vivo and suppresses 25-hydroxyvitamin D-1alpha-hydroxylase expression in vitro. American journal of physiology Renal physiology. 2007;293(5):F1577-83.
136. Wang Y, Zhu J, DeLuca HF. The vitamin D receptor in the proximal renal tubule is a key regulator of serum 1alpha,25-dihydroxyvitamin D(3). American journal of physiology Endocrinology and metabolism. 2015;308(3):E201-5.
137. Bikle DD, Gee E, Halloran B, Kowalski MA, Ryzen E, Haddad JG. Assessment of the free fraction of 25-hydroxyvitamin D in serum and its regulation by albumin and the vitamin D-binding protein. The Journal of clinical endocrinology and metabolism. 1986;63(4):954-9.
138. Bikle DD, Siiteri PK, Ryzen E, Haddad JG. Serum protein binding of 1,25-dihydroxyvitamin D: a reevaluation by direct measurement of free metabolite levels. The Journal of clinical endocrinology and metabolism. 1985;61(5):969-75.
139. Nykjaer A, Dragun D, Walther D, Vorum H, Jacobsen C, Herz J, et al. An endocytic pathway essential for renal uptake and activation of the steroid 25-(OH) vitamin D3. Cell. 1999;96(4):507-15.
140. Leheste JR, Melsen F, Wellner M, Jansen P, Schlichting U, Renner-Muller I, et al. Hypocalcemia and osteopathy in mice with kidney-specific megalin gene defect. FASEB journal : official publication of the Federation of American Societies for Experimental Biology. 2003;17(2):247-9.
141. Dusso A, Gonzalez EA, Martin KJ. Vitamin D in chronic kidney disease. Best practice & research Clinical endocrinology & metabolism. 2011;25(4):647-55.
142. Dusso AS. Kidney disease and vitamin D levels: 25-hydroxyvitamin D, 1,25-dihydroxyvitamin D, and VDR activation. Kidney international supplements. 2011;1(4):136-41.
143. Kim CS, Kim SW. Vitamin D and chronic kidney disease. The Korean journal of internal medicine. 2014;29(4):416-27.
144. Abboud M, Puglisi DA, Davies BN, Rybchyn M, Whitehead NP, Brock KE, et al. Evidence for a specific uptake and retention mechanism for 25-hydroxyvitamin D (25OHD) in skeletal muscle cells. Endocrinology. 2013;154(9):3022-30.

145. Rowling MJ, Kemmis CM, Taffany DA, Welsh J. Megalin-mediated endocytosis of vitamin D binding protein correlates with 25-hydroxycholecalciferol actions in human mammary cells. The Journal of nutrition. 2006;136(11):2754-9.
146. Horn IR, van den Berg BM, van der Meijden PZ, Pannekoek H, van Zonneveld AJ. Molecular analysis of ligand binding to the second cluster of complement-type repeats of the low density lipoprotein receptor-related protein. Evidence for an allosteric component in receptor-associated protein-mediated inhibition of ligand binding. The Journal of biological chemistry. 1997;272(21):13608-13.
147. Jensen GA, Andersen OM, Bonvin AM, Bjerrum-Bohr I, Etzerodt M, Thogersen HC, et al. Binding site structure of one LRP-RAP complex: implications for a common ligand-receptor binding motif. Journal of molecular biology. 2006;362(4):700-16.
148. Burgess A, Vigneron S, Brioudes E, Labbe JC, Lorca T, Castro A. Loss of human Greatwall results in G2 arrest and multiple mitotic defects due to deregulation of the cyclin B-Cdc2/PP2A balance. Proceedings of the National Academy of Sciences of the United States of America. 2010;107(28):12564-9.
149. McCloy RA, Rogers S, Caldon CE, Lorca T, Castro A, Burgess A. Partial inhibition of Cdk1 in G 2 phase overrides the SAC and decouples mitotic events. Cell cycle (Georgetown, Tex). 2014;13(9):1400-12.
150. Molitoris BA, Dahl R, Geerdes A. Cytoskeleton disruption and apical redistribution of proximal tubule Na(+)-K(+)-ATPase during ischemia. The American journal of physiology. 1992;263(3 Pt 2):F488-95.
151. Wolkers WF, Looper SA, Fontanilla RA, Tsvetkova NM, Tablin F, Crowe JH. Temperature dependence of fluid phase endocytosis coincides with membrane properties of pig platelets. Biochimica et biophysica acta. 2003;1612(2):154-63.
152. Raghavan V, Weisz OA. Flow stimulated endocytosis in the proximal tubule. Current opinion in nephrology and hypertension. 2015;24(4):359-65.
153. Kerjaschki D, Noronha-Blob L, Sacktor B, Farquhar MG. Microdomains of distinctive glycoprotein composition in the kidney proximal tubule brush border. The Journal of cell biology. 1984;98(4):1505-13.
154. Nykjaer A, Fyfe JC, Kozyraki R, Leheste JR, Jacobsen C, Nielsen MS, et al. Cubilin dysfunction causes abnormal metabolism of the steroid hormone 25(OH) vitamin D(3). Proceedings of the National Academy of Sciences of the United States of America. 2001;98(24):13895-900.
155. Neels JG, van Den Berg BM, Lookene A, Olivecrona G, Pannekoek H, van Zonneveld AJ. The second and fourth cluster of class A cysteine-rich repeats of the low density lipoprotein receptor-related protein share ligand-binding properties. The Journal of biological chemistry. 1999;274(44):31305-11.
156. Adams JS, Chen H, Chun RF, Nguyen L, Wu S, Ren SY, et al. Novel regulators of vitamin D action and metabolism: Lessons learned at the Los Angeles zoo. Journal of cellular biochemistry. 2003;88(2):308-14.
157. Adams JS, Chen H, Chun R, Ren S, Wu S, Gacad M, et al. Substrate and enzyme trafficking as a means of regulating 1,25-dihydroxyvitamin D synthesis and action: the human innate immune response. Journal of bone and mineral research : the official journal of the American Society for Bone and Mineral Research. 2007;22 Suppl 2:V20-4.

158. Gacad MA, Adams JS. Identification of a competitive binding component in vitamin D-resistant New World primate cells with a low affinity but high capacity for 1,25-dihydroxyvitamin D3. Journal of bone and mineral research : the official journal of the American Society for Bone and Mineral Research. 1993;8(1):27-35.
159. Gacad MA, Adams JS. Proteins in the heat shock-70 family specifically bind 25-hydroxyvitamin D3 and 17beta-estradiol. The Journal of clinical endocrinology and metabolism. 1998;83(4):1264-7.
160. Yamane T, Takeuchi K, Yamamoto Y, Li YH, Fujiwara M, Nishi K, et al. Legumain from bovine kidney: its purification, molecular cloning, immunohistochemical localization and degradation of annexin II and vitamin D-binding protein. Biochimica et biophysica acta. 2002;1596(1):108-20.
161. Marino M, Andrews D, Brown D, McCluskey RT. Transcytosis of retinol-binding protein across renal proximal tubule cells after megalin (gp 330)-mediated endocytosis. Journal of the American Society of Nephrology : JASN. 2001;12(4):637-48.
162. Brenza HL, Kimmel-Jehan C, Jehan F, Shinki T, Wakino S, Anazawa H, et al. Parathyroid hormone activation of the 25-hydroxyvitamin D3-1alpha-hydroxylase gene promoter. Proceedings of the National Academy of Sciences of the United States of America. 1998;95(4):1387-91.
163. Erranz B, Miquel JF, Argraves WS, Barth JL, Pimentel F, Marzolo MP. Megalin and cubilin expression in gallbladder epithelium and regulation by bile acids. Journal of lipid research. 2004;45(12):2185-98.
164. Ernest CS, 2nd, Hall SD, Jones DR. Mechanism-based inactivation of CYP3A by HIV protease inhibitors. The Journal of pharmacology and experimental therapeutics. 2005;312(2):583-91.
165. Chapron B, Risler L, Phillips B, Collins C, Thummel K, Shen D. Reversible, time-dependent inhibition of CYP3A-mediated metabolism of midazolam and tacrolimus by telaprevir in human liver microsomes. Journal of pharmacy & pharmaceutical sciences : a publication of the Canadian Society for Pharmaceutical Sciences, Societe canadienne des sciences pharmaceutiques. 2015;18(1):101-11.
166. Hamon M, Hanada S, Fujii T, Sakai Y. Direct oxygen supply with polydimethylsiloxane (PDMS) membranes induces a spontaneous organization of thick heterogeneous liver tissues from rat fetal liver cells in vitro. Cell transplantation. 2012;21(2-3):401-10.
167. Gershkovich P, Hoffman A. Uptake of lipophilic drugs by plasma derived isolated chylomicrons: linear correlation with intestinal lymphatic bioavailability. European journal of pharmaceutical sciences : official journal of the European Federation for Pharmaceutical Sciences. 2005;26(5):394-404.
168. Toepke MW, Beebe DJ. PDMS absorption of small molecules and consequences in microfluidic applications. Lab on a chip. 2006;6(12):1484-6.
169. Brouard C, Boussac-Zarebska M, Silvain C, Durand J, de Ledinghen V, Pillonel J, et al. Rapid and large-scale implementation of HCV treatment advances in France, 2007-2015. BMC infectious diseases. 2017;17(1):784.
170. Chang SY, Weber EJ, Sidorenko VS, Chapron A, Yeung CK, Gao C, et al. Human liver-kidney model elucidates the mechanisms of aristolochic acid nephrotoxicity. JCI insight. 2017;2(22).

VITA

Brian Dennis Chapron was born on March 27, 1987 in Middletown, CT. He graduated from Xavier High School in 2005. He obtained both his B.S. in Pharmaceutical Sciences and his Doctor of Pharmacy degree from Duquesne University in Pittsburgh, PA in 2011. During his time as a student at Duquesne, he conducted pharmaceutics research under the mentorship of Dr. Moji Adeyeye. In the fall of 2011, he joined the Department of Pharmaceutics at the University of Washington as a PhD graduate student. During his graduate training, he was awarded the NIH TL1 Yearlong Training Grant, the William E. Bradley Fellowship, the University of Washington Top Scholar Award, and the 2017 Innovations in Research Award. Under the mentorship of Dr. Kenneth E. Thummel, he received a Doctor of Philosophy degree in 2018. His current professional plans are to pursue a post-doctoral fellowship in Clinical Pharmacology and The Children's Mercy Hospital in Kansas City, Missouri.